Title
Growth and Characterization of alpha-PbO for Room Temperature Radiation Detection

Author
Ford, Erin Leigh

Publication Date
2014

Growth and Characterization of α-PbO for Room Temperature Radiation Detection

By

Erin Leigh Ford

A dissertation submitted in partial satisfaction of the

requirements for the degree of

Doctor of Philosophy

in

Engineering - Materials Science and Engineering

in the

Graduate Division

of the

University of California, Berkeley

Committee in charge:

Professor Eugene E. Haller, Chair
Professor Daryl C. Chrzan
Professor Tsu-Jae King Liu

Spring 2014

Abstract

Growth and Characterization of α-PbO for Room Temperature Radiation Detection

by

Erin Leigh Ford

Doctor of Philosophy in Engineering-Materials Science and Engineering

University of California, Berkeley

Professor Eugene E. Haller, Chair

A global trading structure and high throughput of shipping containers into ports around the world increases the chance of nuclear terrorism via cargo containers. Harmless radioactive sources confuse and impede detection of the materials that pose a real threat, making spectroscopy difficult and requiring detectors with high resolution. The current methods that are used to check containers in ports have security flaws, and only 5% of all shipping containers are checked. The development of semiconductor γ-ray detectors is one of the protocols being advanced to alleviate this risk because they can function at room temperature and they are cost effective, easily produced, and have high resolution. This dissertation has addressed the current lack of "perfect" room temperature detector materials by investigating α-PbO, a novel material in this field. This includes the development of a growth process for α-PbO thin films, as well as its structural and performance characterization as a detector material.

Because we intend α-PbO to be a photoconductive detector, it should have certain properties. A photoconductive detector consists of a highly resistive material with a voltage bias across it. It absorbs incident γ-rays, creating electron-hole pairs that provide a signal. To function well, it must have a high atomic number and a high density in order to absorb high-energy photons via the photoelectric effect. It should also have a large resistivity and a wide band gap to avoid large leakage currents at room temperature. Finally, it must have good charge carrier transport properties and detector resolution in order to be able to determine the characteristic energy peaks of the radiation-emitting source. We chose α-PbO because it has a very high Z and a very high density and a band gap in the correct range. It also has a rich history of use as a photoconductor that reaches back to the 1950s.

Numerous methods have been used to grow thin films of α-PbO. However, rarely are those films single phase or highly oriented. Pulsed laser deposition provides a method to grow epitaxial thin films of α-PbO. The structure of the grown films was characterized using X-ray diffraction 2θ-ω scans, rocking curves, and reciprocal space mapping. Feedback from a parameterized study of the structural characterization enabled optimization of the growth process to improve the quality of the thin films. The parameters that were studied included: epitaxial strain, substrate temperature, oxygen background pressure, and fluence of the laser. The result of this process led to favorable growth parameters that included: KTO substrates, a substrate temperature of 495°C, an oxygen pressure of 10 mTorr, and a fluence of ~ 6 J/cm^2. The resulting

films showed peak broadening in the XRD scans that was only marginally greater than the peak broadening seen in scans of the single crystal substrate.

The methods used for the optical measurement of α-PbO films included absorption spectroscopy and ellipsometry. Determination of the spectral absorption coefficient was achieved by transmission spectroscopy and reflection spectroscopy via a PerkinElmer Lambda 950 UV-Vis spectrophotometer. Analysis of the square and square root of the absorption coefficient yielded values for the direct band gap and the indirect band gap of α-PbO. These values were $E_{g,dir} = 3.2$ eV and $E_{g,ind} = 1.9$ eV, respectively. To date, spectral ellipsometry measurements had never been performed on α-PbO. These initial measurements yielded the first recording of the spectral complex index of refraction. This is useful for analyzing how light interacts with α-PbO material. The data was used to help measure the thickness of the thin films.

Study of the electronic and transport properties of α-PbO is important in order to understand how the material will behave as a radiation detector. In general, photoconductive detectors have a very large applied voltage bias in order to ensure efficient charge collection. Therefore, high resistivity is needed to keep the resultant leakage current at a manageable level. Resistivity was determined current-voltage characteristics. The resistivity of the α-PbO thin films via this two-point probe measurement ranged from 10^{10} Ω cm to 10^{13} Ω cm. However, two-point probe analysis involves errors due to contact and probe resistance. The four-point probe measurements are underway.

Spectral photoconductivity was measured to ensure that α-PbO's response to light was large enough for it to be a useful detector material and to confirm the band gap measurements. The photocurrent onset occurred at the energy corresponding to the indirect band gap and it peaked at the energy corresponding to the direct band gap. The maximum photocurrent measured at a bias voltage of 60 volts was 4.7 nA. This value is four orders of magnitude greater than the photocurrent displayed at energies below the direct band gap.

In the field of detector materials, the μτ-product is commonly used as a figure of merit because it enables a measurement of the trapping length of the charge carriers within the detector. Many's equation, which is a derivation of the photocurrent with respect to the applied voltage across a wide band gap semiconductor, is one of the methods used to determine the μτ-product. The photocurrent voltage measurements were obtained from the 0.5 V to 80 V range. This data was difficult to fit with Many's equation over that whole range. Higher voltages displayed deviation from ideal behavior due to the contact effects, but at the lower voltages the data were unaffected. Fits to the lower voltage range, from 0.5 V to 10 V, yielded $\mu\tau = 6.8 \times 10^{-4}$ cm^2/V.

Room temperature photoconductors will ultimately be used to detect γ-rays; however, thin films do not have enough stopping power to absorb the total energy of a γ-ray. Therefore, we study the α-PbO detector response to radiation in the form of alpha particles because they are large, charged, and relatively easy to stop. SRIM calculation estimated that alpha particles have a range of up to 16 μm in α-PbO. The initial long-duration film growth yielded films that were ~ 8 μm thick. Therefore, a full energy peak from alpha particles was not seen in α-PbO. We did see a shoulder protruding out of the noise peak due to the charge carriers that were created before the alpha particles escaped the detector volume.

Table of Contents

List of Figures

List of Tables

Acknowledgments

I am very grateful to have the opportunity to do my graduate work in the research group of Professor Eugene Haller. He has given great support and advice while also allowing me the discover myself as a scientist. He pushed me to understand the science and improve my own research skills. I will always remember late nights working with him in the laboratory. He taught me so much, from understanding how a radiation detection system works to making electronic gadgets, preparing samples, building circuits and so much more than I could possibly list here.

I also would like to thank Professor Daryl Chrzan for his incredible support, especially in the writing phase of this dissertation. He is an incredible theorist and truly understands how to question each aspect of the research in order to better understand it. Discussing research with him taught me to critically examine each issue until I truly understand it. I am grateful to him for his encouragement and support, both scientifically and personally.

I owe Jeffery Beeman considerable gratitude. Not only does he keep the lab running, he also taught me so much about device-making. He was always willing to listen to whatever project I was trying to do and gave good advice and helpful ideas. He also fabricated parts for me and performed implants when I was learning to make diodes.

I was fortunate enough to have the opportunity to work with Professor Ramamoorthy Ramesh in his lab, where I learned about the growth and structural characterization of thin film metal oxides. He allowed me to grow films in his lab and gave me good advice when I needed it. I am also grateful to have been able to work with his students over the years, Morgan Trassin for his advice, Guneeta Singh Bhalla for her advice and friendship, and James Clarkson for being willing to discuss ideas and lend a hand whenever I needed it while rebuilding my growth chamber.

I would like to thank Professor Ronald Gronsky for chairing my qualifying exam committee and Professor Daryl Chrzan, Professor Oscar Dubon and Professor Tsu Jae King Liu for serving on my qualifying exam committee. I would also like to thank Professor Eugene Haller, Professor Daryl Chrzan and Professor Tsu Jae King Liu for reading this dissertation.

I am indebted to Bill Hansen, Professor Oscar Dubon, Professor Ronald Gronsky, Dr. Kin Man Yu, Dr. Joel Ager, Dr. Wladek Walukiewicz, Dr. Lothar Reichertz and Dr. Corsin Battaglia, for good conversations and advice or a push in the right direction. I was also fortunate enough to work with Dr. Paul Luke, Dr. Mark Amman, and Dr. Craig Tindall during the setup of the radiation detection portion of this research. They are amazing scientists and I feel lucky to have had the opportunity to work with them.

Dr. Marie Mayer was the best first officemate (and roommate) I could have had. She helped show me the ropes and was an invaluable person to talk to and brainstorm ideas with. It was fun to work with her in the lab. She was great at pushing me to try new experiments and taught me that nothing is too complicated to try and fix. I am also grateful for the support of my fellow grad students, Dr. Karen Bustillo, Dr. Doug Detert, and Alex Luce for support, great conversations about science, research, and life while we made our way through grad school. I am grateful to Dr. Ruben Lieten at KU Leuven and IMEC in Belgium for help with ellipsometry measurements. Finally, I would like to thank John Bowe, retired from American President Lines (APL), for organizing a tour of the Port of Oakland APL terminal for my entire research group.

My research was supported by the Domestic Nuclear Detection Office (DNDO) and the National Science Foundation (NSF) through the Academic Research Initiative (ARI). I am indebted to them for 5 years of funding, annual trips to the east coast for grantee conferences, and a project that truly felt like a worthwhile cause.

Graduate school has its ups and downs, with trials, tribulations and triumphs. I don't think I would have made it through without the love and support of my family and friends. From my parents I received unconditional love and support. To my dad I owe the love of the science, he is the one who helped me find my way to graduate school in the first place. I really appreciated the technical conversations and the love and support over the years. My mom has always been an inspiration to me and encouraged me to further my scientific education. From her I have received many pep talks and encouragement when I needed it most. I thank my sister, Heather, and my brother, Patrick, for being there for me and cheering me along the path.

I want to thank my husband Kristian for encouraging me to apply to Berkeley for a doctoral degree, for sticking by me even when it felt like graduate school would never end, and for always pushing me to be my best self. He is the one who experienced the graduate process with me on a daily basis. He has been very supportive in pushing me to push myself to finish. I also want to thank my parents-in-law, Robert and Kristi Hanelt, for being so supportive, for feeding me home-cooked meals when I needed them, and for being the best parents-in-law anyone could ask for.

Chapter 1: Introduction

1.1 Overview

Every year, tens of millions of shipping containers enter seaports and cross borders around the globe. This high throughput of shipping containers increases the opportunity and likelihood that illicit nuclear materials used for nuclear proliferation or terrorism will be transported. To combat this threat, researchers are developing methods to detect these materials with the lowest possible cost and the highest possible efficiency. To achieve that end, it is necessary to develop detection systems that can identify radioactive materials based on their decay products. To further this aim, we propose original research into the growth and characterization of a novel material for room temperature radiation detection.

1.2 Background

In the last decade or two, the United States (US) and many other countries have begun to recognize the threat posed by nuclear terrorist attacks via cargo shipment. As the global transport of goods has increased over the years, so has the opportunity to slip a nuclear threat through the cursory spot check system that has been employed at ports, worldwide. This poses a problem of scale. On a one-by-one basis, each shipping container could be checked and determined to be threat free, with 100% accuracy. However, the logistics of doing this for the approximately 50,000 [1] shipping containers coming into US ports each day are impossible and would immediately cripple the shipping industry. Globally, the maritime shipping industry comes into contact with 90% of all traded goods [1]. Any delay in shipment due to content analysis would have a significant impact on the global economy.

Naturally occurring and non-nefarious radioactive material is everywhere and it can impede the detection of threat materials. Isotopes in the uranium, thorium, and potassium families have very long half-lives and they exist at low levels in all natural earthenware materials [2]. Building materials originating in Italy, including bricks, concrete, and mortar, commonly exhibit measureable levels of radon (^{226}Ra), thorium (^{232}Th), and potassium (^{40}K) [3]. Similar results occur for ceramic tile originating from China [4]. Medical isotopes that are man-made and can legally be shipped via container include americium (^{241}Am), barium (^{133}Ba), and cesium (^{137}Cs), among others [2]. Even flour [5] and bananas [6] from Brazil have been found to have significant levels of radioactive radon isotopes due to uptake from soil. Other sources of radiation that are commonly contained in shipping containers can be found in fertilizer, glazed ceramics, including Fiestaware$^{\text{TM}}$ that was manufactured before the 1970s [7], pottery, dental materials, aircraft parts, camera lenses, and even kitty litter [2]. This abundance of non-threatening nuclear radiation can set off alarms when goods are moving through ports in shipping containers. Therefore, it is necessary to implement methods to determine which radioactive materials are dangerous and which are harmless.

In a 2011 tour of the American Presidents Line (APL) terminal in Oakland, California, we learned that glorified spot-checking is the method that is used to verify port security. All incoming containers travel through portal detection systems that consist of scintillator detectors that determine whether or not they house radioactive materials. Those containers that are not radioactive are allowed to proceed to their next destination. In situations in which the alarms are set off, the cargo manifest is compared to the weight of the shipping container and the location of origination. If no red flags arise, the containers are cleared to move on to their final destinations. Any containers that do raise red flags are pulled aside for further monitoring. First, those containers are X-rayed to determine if they house any heavy materials that could act as shielding for radioactive substances. If all appears to be normal, the container may be sent on. If more red flags arise, the container may be opened and a cooled germanium detector will be used to search its contents.

Unfortunately, this entire process has significant security holes and only ~5% of all shipping containers are checked. In August 2003, an exposé by ABC News investigative reporter, Brian Ross, shipped 15 pounds of depleted uranium that was packaged to appear like a weapons grade threat in order to test the efficacy of current screening methods. The material was shipped to Los Angeles, via a private shipping company from Jakarta, a hot spot of terrorist activity, and then it was driven by truck through the center of the city to a warehouse where the news team filmed the opening of the pristinely sealed container. The material was hidden in a suitcase, within a trunk amidst furniture and earthenware pottery [1]. This breach in security underscores the need for research into new protocols for radiation detection.

One of those protocols involves detection of γ-radiation as the primary decay product. The type of decay product to be detected dictates the type of radiation detector that is used. In the case of nuclear security, high-energy γ-rays hold the most interest because they are the radioactive decay products that will transmit through the walls of a shipping container. We focus on semiconductor γ-ray detectors, wherein γ-rays create electron-hole pairs within the semiconductor. These pairs are swept out of the material by an applied electric field creating a signal that is, ideally, proportional to the energy of the γ-ray. Deviation from ideality, for example due to charge trapping by material defects, reduces spectral resolution. Thus, high quality semiconductor materials are needed to manufacture a detector with high spectral resolution. These detectors would need to be low in cost and easily mass-produced so that, in theory, they would be used on every shipping container in every port. The best-case scenario is to detect threat materials before they are loaded onto a container ship.

Currently, two materials dominate the search for a state-of-the-art detector to identify nuclear threat materials: high-purity germanium (HPGe) and cadmium zinc telluride (CZT). HPGe detectors operate optimally at liquid nitrogen (LN2) temperatures, as this reduces the leakage current and the associated noise. While HPGe detectors have high resolution in the 0.2% range for γ-ray energies of 662 keV [8] (662 keV is the energy of the γ-ray emitted by ^{137}Cs, often used as a standard for detector measurement), detector cooling is impractical for searching large numbers of shipping containers in transit through seaports and at borders. In order to avoid these cooling issues, research is investigating ways to develop materials that are capable of high resolution, low-leakage current, and radiation detection at room temperature. To date, CZT is the most advanced room temperature detector material that is being used. It has a sufficiently large band gap to enable room temperature function without large leakage current. Its relatively high atomic number yields good stopping power for high-energy γ-rays. The resolution of CZT is on the order of 1.8% for γ-ray energies of 662 keV [9]. However, CZT is costly, due to a difficult crystal growth process and the low yield of the detector-grade material.

Thus, the search for cost-effective room temperature detector materials continues. Upon initial inspection, lead oxide (α-PbO) is an interesting candidate [10]. Its band gap is sufficiently large (its indirect band gap is 2.0 eV and its direct band gap is 2.6 eV [11]) and it has very high Z and density and, therefore, large radiation stopping power. Despite this, little research has been conducted to investigate its detector properties.

1.3 Purpose of the Study

The purpose of this study is to address the lack of "perfect" room temperature detector materials through an investigation of novel materials. This is achieved by the development of a growth process for a new material, α-PbO, and subsequent characterization of that material. In order to address the most basic and initial characterization needs in an efficient manner, the material is grown in a thin film format. That growth is achieved through pulsed laser deposition (PLD). Characterization of the structural quality of the material is the first concern that is addressed. Development of the growth process in conjunction with characterization of the material structure enables optimization of quality thin film material.

After achieving high quality thin films of α-PbO, the next step is to characterize the optical and electronic properties. Optical properties measurements include measurement of the optical constants of α-PbO, as well as measurement of the band gaps (indirect and direct). Measurement of the electronic properties of α-PbO encompasses photoconductivity and μτ-product. Finally, we use alpha particles to test the material's ability to serve as a radiation detector. In this way, we seek to determine the suitability and potential of α-PbO as a room temperature semiconductor radiation detector material.

1.4 This Dissertation

This dissertation consists of seven chapters. In Chapter 2, we will look in detail at the photoconductive detector and its use as a room temperature radiation detection device. This chapter also discusses the requirements for the materials that are suitable for use in room temperature photoconductive detectors.

In Chapter 3, we address the growth of the α-PbO material. We discuss the growth process by which single-phase, highly oriented epitaxial α-PbO is grown in a vacuum chamber via PLD. We employ X-ray diffraction (XRD) techniques to enable characterization of the structural quality of the material. We use feedback from the structural characterization to optimize the growth process in order to increase the quality of the material.

Chapter 4 discusses the study and measurement of the optical properties of the material. The reflection and transmission measurements enable the calculation of an absorption coefficient spectrum that, in turn, allows for measurement of the band gaps of the material. These data are collected using a UV-Vis spectrophotometer. Further optical characterization is obtained by taking ellipsometry measurements of the material, which yields data about the complex index of refraction and the thin film's thickness.

Chapter 5 discusses the electronic measurements that are used in this study. A monochromator, a white light source, and a current measurement device are used to measure the spectral photocurrent. Photocurrent vs. voltage measurements yield a value for the μτ-product of the material.

Chapter 6 addresses the detection of alpha particles by α-PbO. That measurement is performed using an alpha particle detection system built at the Lawrence Berkeley National Laboratory. Chapter 7 will conclude this work.

Chapter 2: Detectors and Materials

2.1 How a Photoconductive Detector Works at Room Temperature

A photoconductive or resistive detector consists of a semiconductor with two electrical contacts. A voltage bias across the contacts creates an electric field within the material that functions as the active region of the detector. An incident γ-ray interacts with the semiconductor material to create electron-hole pairs, effectively increasing the conductivity of the material [12]. The electric field in the material sweeps the electrons toward the positively biased electrode and sweeps the holes toward the negatively biased electrode. A schematic of a photoconductive detector is shown in Figure 1. The number of electron-hole pairs created is directly proportional to the amount of energy that the γ-ray deposits into the detector, allowing for direct measurement of that energy by analysis of the resultant signal [8].

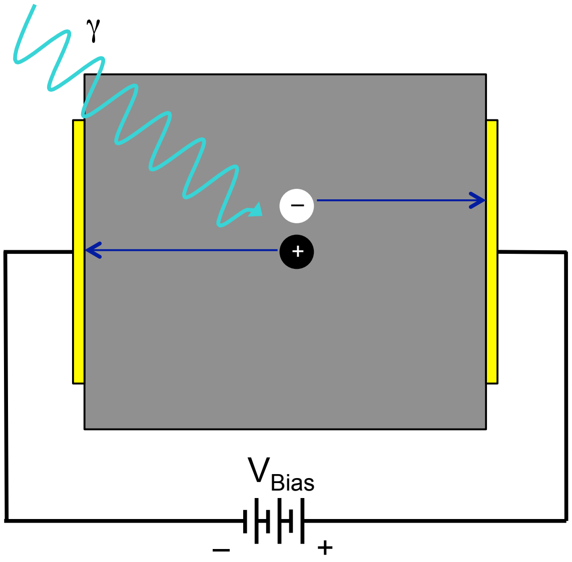

Figure 1: A schematic of a photoconductive detector.

The details of the process described above determine the properties of the materials that are suitable for this application. These properties include: the atomic number (Z) and the atomic density of the semiconductor, the band gap, the resistivity, and the charge carrier transport properties. The remainder of this section discusses the details of those requirements. It should be noted that high purity germanium (HPGe) is the state-of-the-art detector of γ-rays. Although it is not a photoconductive detector, we make comparisons to its cooled function because the goal of this field of research is to develop room temperature detectors that function as well as the HPGe detector functions in a cooled state.

2.1.1 High atomic number and density

To appreciate the effect that high atomic number (Z) has on the detection of gamma rays, it is necessary to provide some background on γ-ray absorption. There are three main processes by which a γ-ray can interact with material: photoelectric effect, Compton scattering, and pair production. The photoelectric effect occurs when a photon (i.e. a γ-ray in our case) interacts with an atom in the semiconductor during an absorption event. The atom absorbs the photon completely, causing the ejection of a bound shell electron. This electron is known as a photoelectron, and it has an energy of $E_{e^-} = h\nu - E_b$, where E_b is the binding energy of the electron in the bound shell of the atom [12]. This process is shown schematically in Figure 2.

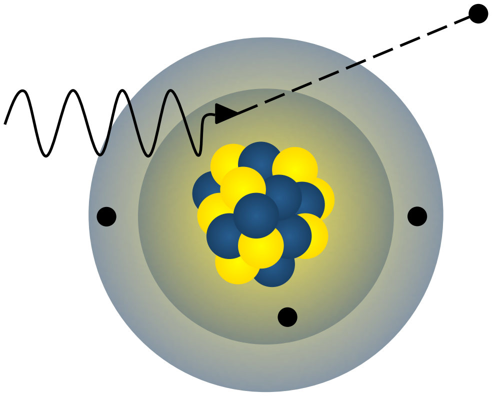

Figure 2: Schematic of the photoelectric effect.

When dealing with high-energy γ-rays, the photoelectron will likely originate from an inner K-shell electron. Ejection of the photoelectron leaves a hole in the inner shell. Electrons from the outer shells fill the holes quickly, causing the emission of characteristic X-rays, or more rarely, an Auger electron. Although it is possible for characteristic X-rays or Auger electrons to escape the detector, these secondary particles are normally reabsorbed rapidly by the photoelectric effect. When the energy of the incident γ-ray is converted into photoelectrons, the total integrated charge is directly proportional to the energy of the γ-ray [8]. For mono-energetic γ-rays, absorption by photoelectric effect results in the formation of a photopeak, or a full energy peak, in the final energy spectrum, as shown in Figure 3.

Compton scattering is an interaction between the incident gamma rays and the electrons in the semiconductor material. Instead of being totally absorbed, the γ-ray is deflected by an angle θ from its original direction and it loses a fraction of its energy to the electron [12], as shown schematically in Figure 4.

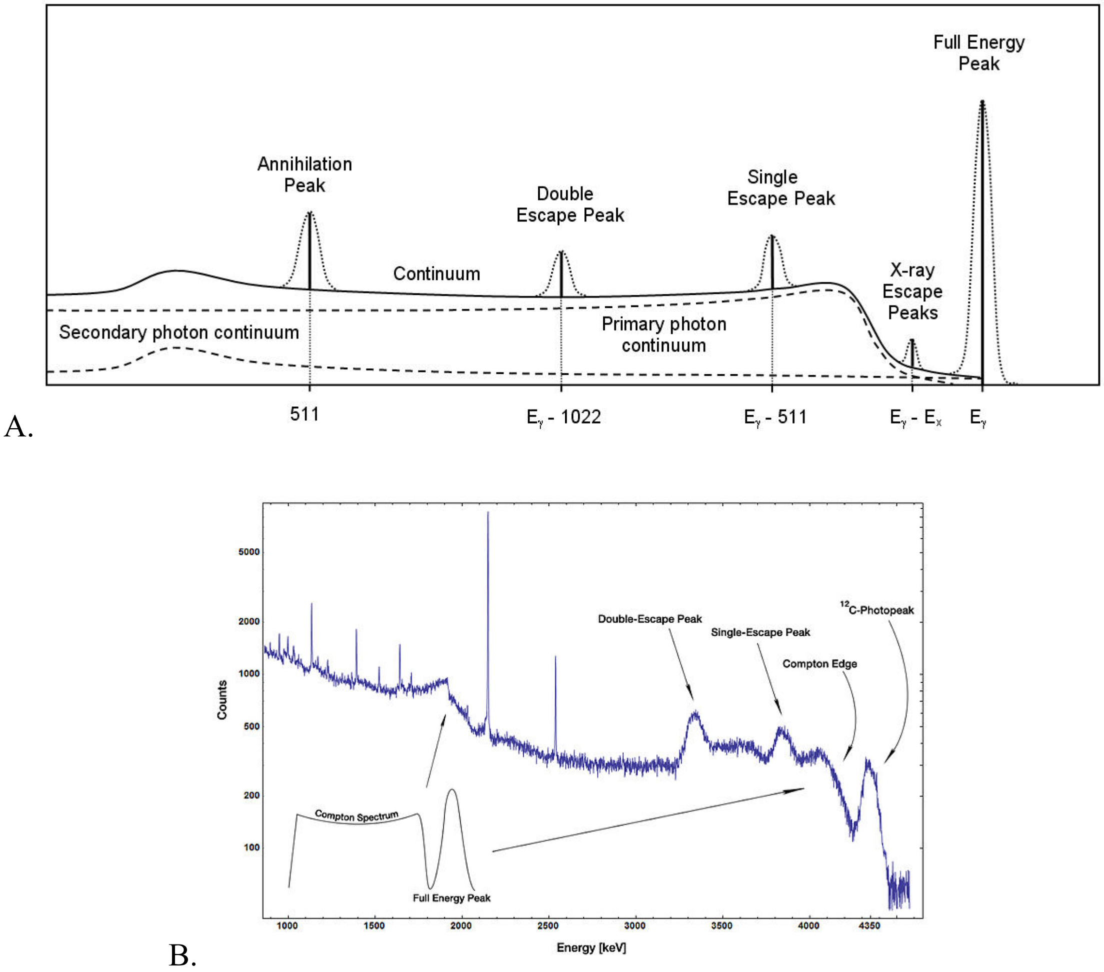

Figure 3: A.) Schematic of a semiconductor detector γ-ray spectrum showing the characteristic properties of the three main absorption processes: photoelectric effect, Compton scattering, and pair production [13]; B.) A real spectrum showing many of the characteristics of the three processes [14].

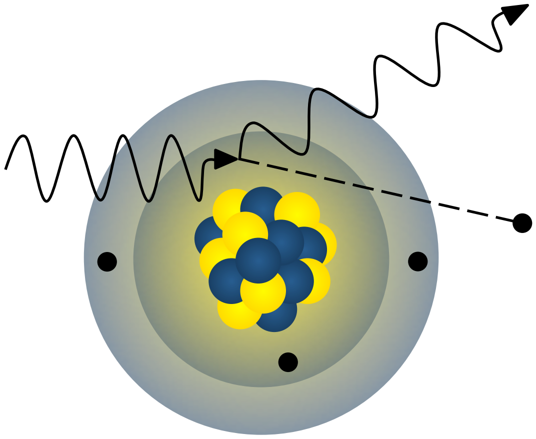

Figure 4: Schematic of Compton scattering.

The electron, called a recoil electron, is ejected with the amount of energy lost by the initial γ-ray. The final energy of the γ-ray is calculated using the formula:

$$h\nu' = \frac{h\nu}{1 + \frac{h\nu}{m_0c^2}(1 - \cos\theta)}$$

where m_0c^2 is defined as the rest mass energy of the electron (0.511 MeV). As the γ-rays can be scattered at any angle, the energy transferred to the electron varies from zero to a large percentage of the initial γ-ray energy. As seen in Figure 3, this shows up as a Compton plateau where the gamma spectrum has a fairly uniform height across a significant part of the energy spectrum below the full γ-ray energy peak [12].

Pair production is the final process of γ-ray absorption; this is the result of an interaction between the γ-ray and the coulomb field of the atom nucleus. Pair production becomes possible when the incident γ-ray energy is at least 1.02 MeV (twice the rest mass of an electron). In actuality, the probability of pair production is quite low until the γ-ray energy is more than a few hundred keV above the threshold. In this process, the energy of the γ-ray is converted into an electron-positron pair, as shown schematically in Figure 5. Any γ-ray energy over 1.02 MeV goes into the kinetic energy of the new pair [12].

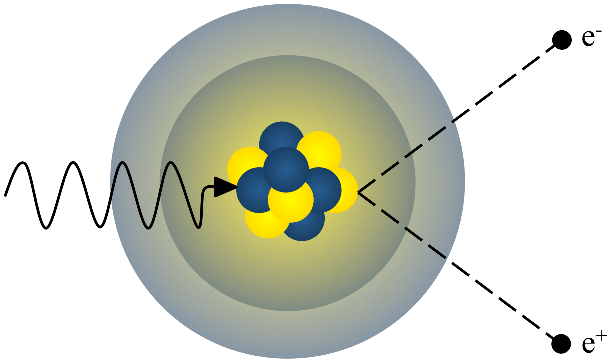

Figure 5: Schematic of pair production.

In most cases, the positron can only travel a short distance before it encounters an electron, causing annihilation. This pair annihilation process results in the emission of two 0.511 MeV photons. If one of these 0.511 MeV photons escapes the detector material, a new peak (the single-escape peak) forms in the γ-ray spectrum. This single-escape peak will occur at a position 0.511 MeV below the full energy photopeak. Similarly, if both 0.511 MeV photons escape the detector material, a double escape peak forms 1.02 MeV below the full energy photopeak, as noted in Figure 3.

Of all these mechanisms, only the photoelectric effect produces a peak that is directly proportional to the energy of the incident γ-ray. Additionally, when trying to determine the type of material emitting radiation, the Compton plateau and the pair production escape peaks can only cause confusion. Therefore, it is highly preferable to have the incident γ-rays interact with the detector material primarily through the photoelectric effect.

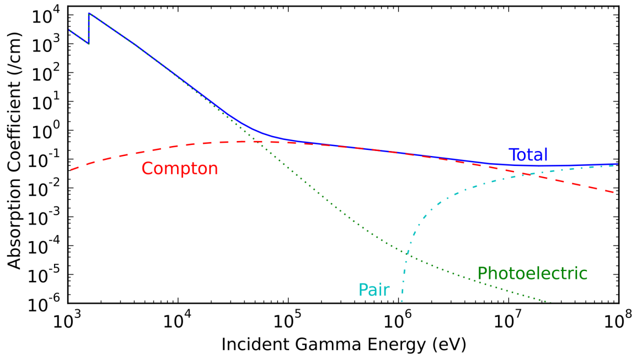

A. Absorption coefficient of γ-rays in aluminum (Z = 13).

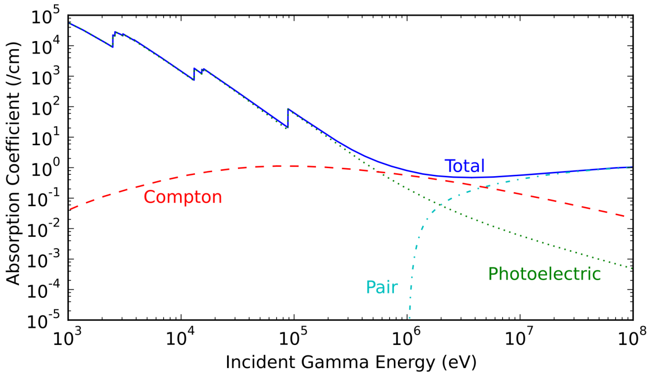

B. Absorption coefficient of γ-rays in lead (Z = 82).

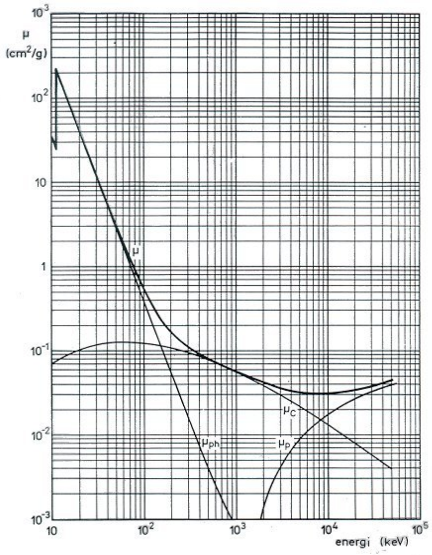

C. Attenuation coefficient of γ-rays in germanium (Z = 32).

Figure 6: Absorption coefficient spectra showing dominant mechanisms of absorption. This shows a comparison of the effect that Z and the incident γ-ray energy have on the absorption in materials: A.) aluminum [15], B.) lead [16], and C.) germanium [17]. Compton scattering overcame photoelectric effect at ~ 40 keV in aluminum, at ~ 75 keV in germanium, and at ~ 500 keV in lead.

A number of factors affect how the γ-ray interacts with the detector material. Two of the most important factors include the energy of the γ-ray and the atomic number (Z) of the detector material. As displayed in Figure 6, the photoelectric effect is the dominant process of absorption for lower energy gamma rays. The Z of the detector material determines the high-energy side of this range. The probability of absorption via the photoelectric effect is proportional to the Z of the material by the following relationship:

$$Probability_{pe} \propto \frac{Z^n}{E_\gamma^{3.5}}$$

where Z is the atomic number of the detector material, E_γ is the energy of the incident γ-ray, and n is a number between 4 and 5. Therefore, the photoelectric effect remains the dominant mechanism of absorption at much greater energies in lead (Pb) than in aluminum (Al) or germanium (Ge). This can be seen explicitly in Figure 6. Compton scattering overcomes the photoelectric effect as the dominant form of absorption at 40 keV for aluminum, at 75 keV for germanium, and at 500 keV for lead. Compton scattering is the dominant method of absorption in the middle range of gamma energies. Like the photoelectric effect, Compton scattering is also dependent upon the Z of the detector material. It scales linearly with Z because the probability of absorption through Compton scattering depends upon the number of electrons that are available to act as scatterers. Although the probability of Compton scattering may be higher in Pb than it is in Al, that fact is still outweighed by the larger power dependence that Z has on the absorption via the photoelectric effect, as seen in Figure 6. The probability of Compton scattering diminishes as energy increases or decreases. Pair production has a roughly square dependence on the Z of the detector material. It is also very dependent upon the γ-ray energy. It is not physically possible for pair production to occur at energies lower than twice the rest mass of an electron, 1.02 MeV. However, pair production becomes the dominant mechanism for absorption at very high γ-ray energies, as shown in Figure 6.

Even though Compton scattering and pair production both increase directly with the detector material Z, the Z-dependence of the photoelectric effect is much more powerful due to the larger (4th to 5th) power. It is most advantageous to use high Z materials to increase the likelihood of absorption through the photoelectric effect. It is important to note that, because of the power law scaling of the photoelectric effect, the probability of photoelectric absorption is much higher for binary materials in which one component has a very high Z versus a binary material in which both components have a moderate Z. For example, PbO contains lead, with $Z_{Pb} = 82$, and oxygen, with $Z_O = 8$, and CdTe has cadmium, with $Z_{Cd} = 48$, and tellurium, with $Z_{Te} = 52$. Assuming constant γ-ray energy and a Z-dependence of $Z^{4.5}$, comparing the two gives:

$$Probability_{PE}(CdTe) \propto \frac{1}{2}(48^{4.5} + 52^{4.5}) = 44{,}751{,}298.8$$

$$Probability_{PE}(PbO) \propto \frac{1}{2}(82^{4.5} + 8^{4.5}) = 204{,}712{,}625.9$$

wherein the effect that Z has on the probability of the photoelectric effect occurring is almost five times larger in PbO than it is in CdTe.

Density is also an important factor in γ-ray detection materials. It plays a role in the stopping power of the material. The stopping power of a material is simply a measure of the energy lost by the γ-ray along a given path length. The plots in Figure 6 show the attenuation coefficients for lead, aluminum, and germanium. These attenuation coefficients are dependent upon the density of the absorbing material. A lower density material will have a lower attenuation coefficient because the incident γ-rays have a lower likelihood of encountering the atoms in the detector. Higher density materials have shorter mean free paths for high-energy photons.

2.1.2 Range of the band gap material

The advantage of using large band gap material is fairly straightforward. At room temperature, a small band gap semiconductor has a number of electrons in the conduction band due to thermal excitations. This will lower the resistivity of the material. A large band gap semiconductor has fewer excited electrons, and a higher resistivity. In order to function properly, the photoconductive detector requires a large voltage bias. According to Ohm's Law, $I = V/R$, if the resistivity of the material is reduced due to thermally generated carriers, a larger leakage current will result. Associated noise can be large enough to drown out any signal and render the detector useless. Analysis of the material requirement for high resistivity will be discussed in Section 2.1.3. A large band gap of at least 1.5 eV is necessary to suppress the thermally generated leakage current during the operation of a room temperature detector.

There is a limit to how large the band gap of the detector should be. There are advantages to having a smaller band gap. The average energy required to create an electron-hole pair scales roughly as three times the band gap energy [18]. The larger the band gap, the smaller the number of excited charge carriers that will be produced; this results in a smaller signal. Therefore, to optimize the detector's performance at room temperature, it is necessary to maintain a balance between the low thermal leakage noise of a large band gap and the high signal of small band gap material. In this field, it is common to define room temperature detector materials as those that have band gaps in the range of 1.5 eV to 3 eV.

2.1.3 High resistivity

As mentioned in Section 2.1.2, photodetectors that operate at room temperature must have a high resistivity. This is especially important because, in order to achieve efficient charge collection, one must use large bias voltages on the order of 100s of volts or 1000s of volts. Large voltage bias can induce large leakage currents in materials with low resistivity. If the leakage current is too large, it can drown out the signal from the incident γ-rays. For example, if a radiating source creates 10^5 charge carriers, the resultant peak current could be expected to be on the order of 10^{-6} A. In order to be able to measure the signal reliably, the leakage current should be on the order of 10^{-9} A [12].

Realistic leakage current can be estimated by looking at the theoretical leakage current of the detector materials in room temperature conditions. The geometry and resistance of a sample are related to the resistivity as:

$$\rho = R\frac{A}{\ell}$$

where R is the electrical resistance, A is the cross-sectional area, and ℓ is the thickness of the sample. To simplify this example, assume all samples have a cross-sectional area of 1 cm^2 and a thickness of 1 mm. High purity Si has a resistivity of approximately 5×10^4 Ω-cm. A sample of Si in this geometry, with ohmic contacts on the top and bottom faces of the sample, has a resistance of 5000 Ω. Assuming a bias voltage of 500 V across the Si sample mentioned above, the resultant leakage current would be 0.1 A and the signal from the radiation source would not be distinguishable. Similar calculations can be done for HPGe, with a resistivity of 50 Ω-cm and a resulting leakage current of approximately 100 A. These two detectors are not suitable for room temperature operation. CZT has a resistivity in the 10^{10} Ω-cm range [9], which corresponds to a leakage current of 5×10^{-7} A. That level of leakage current is much closer to a manageable level. To find the ideal detector resistivity, and assuming geometry that is identical to the geometry mentioned in the previous example, a detector would have a leakage current of 10^{-9} A at 500 V bias. This leads to a resistivity in the range of 10^{12} Ω-cm in order to keep the noise three orders of magnitude smaller than the signal.

2.1.4 Good charge carrier transport properties and detector resolution

When a photon of energy larger than the band gap of a semiconductor excites an electron, it transitions from the valence band to the conduction band, where it is free to conduct electricity. The excited electron leaves behind a hole in the valence band that can also move through the material. In the absence of an electric field, the electron-hole pairs eventually recombine. However, if an electric field is present in the semiconductor, as is the case for a photoconductive detector, the electron-hole pair separates and the electrons flow against the electric field while the holes move with the electric field. This motion of the charge carriers contributes to the conductivity of a material [12].

Study of the characteristics of the flow of electricity in semiconductors would not be complete without a thorough examination of two quantities: lifetime and mobility. The lifetime, τ, is the mean free time between scattering events for the charge carriers. The mobility, μ, relates to the ability of the charge carriers to move through the material [19]. When the applied electric field is not very large, the charge carriers flow with a velocity that is proportional to the field [12].

If a photon incident on the detector has a large amount of energy compared to the detector band gap, for example a high-energy γ-ray, each of the incoming photons will create many charge carriers. The average amount of energy required to create each of those electron-hole pairs is known as the ionization energy, which is approximately equal to the band gap energy multiplied by 3 [18, 20]. Additionally, for ideal photoelectric effect absorption, the total amount of charge created within the detector is directly proportional to the energy of the γ-ray. If every electron-hole pair could be collected through the contacts of the detector, perfectly, it would be possible to determine the precise measurement of the energy of the incident radiation.

However, no real material is ideal. Materials contain defects that act as traps and recombination centers, removing charge carriers from the signal, thereby resulting in energies that are not quite as large as the incident γ-ray. This causes a spread in the photopeak. Measurement of this peak spread, or full width at half maximum (FWHM), is a common method used to determine the performance or resolution of the detector. Energy resolution can be defined as the FWHM of the photopeak divided by the position of the photopeak [12]. The better the detector resolution, the narrower the peak, which means that two peaks that are located near each other in the energy spectrum can be resolved in a detector with good resolution, but they may not be resolved in a detector with poor resolution, as demonstrated in Figure 7.

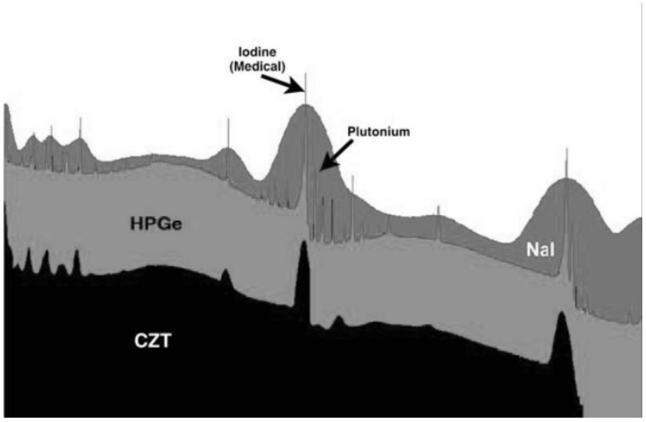

Figure 7: A comparison of detector resolution between scintillator NaI, and semiconductors HPGe and CZT [21]. It is important to note that while the resolution of the CZT detector is not as good as the resolution of the HPGe detector, the CZT resolution has improved since this data was taken.

For example, cooled high purity germanium (HPGe) has the best energy resolution of all the gamma ray detectors at approximately 0.2% FWHM at 662 keV [8]. The detector resolution arises from a combination of statistical fluctuations and broadening due to the charge carrier trapping by defects in the material. The statistical fluctuations arise in the following manner. As a γ-ray enters the semiconductor detector, electron-hole pairs are formed. The total number of charge carrier pairs created can be determined using:

$$N = \frac{E}{\varepsilon} \ ,$$

where ε is the average energy required to create an electron-hole pair or ionization energy as previously discussed, and E is the energy deposited into the detector by the γ-ray. If N is identical for each γ-ray and all charge is completely and perfectly collected, the resulting photopeak would be a delta function at the total integrated charge, proportional to the γ energy. However, the value of N contains statistical fluctuations, causing broadening of the photopeak that cannot be removed by more perfect charge collection. Assuming that charge carrier generation follows a Poisson process, there will be a standard deviation in the number of charge carriers that are created, N, that is equal to $\sqrt{N}$. Due to the linear response we expect from the semiconductor detectors, the amplitude of the pulse height, H_0, is linearly dependent upon the number of charge carriers generated, as follows:

$$H_0 = CN,$$

where C is a proportionality constant. The standard deviation of the peak is defined by Poisson statistics as:

$$\sigma = C\sqrt{N}.$$

N is a large value, so the peak can be assumed to have a Gaussian shape. The FWHM of the peak can then be determined as:

$$FWHM = 2.35\sigma = 2.35\, C\, \sqrt{N}.$$

However, careful experimentation has shown that carrier generation cannot be accurately described by Poisson statistics alone. This departure from the above formulation is quantified by a constant called the Fano factor [12]:

$$F \equiv \frac{Observed\ variance\ in\ N}{Poisson\ variance\ in\ N},$$

which is applied to the fluctuation in N as follows:

$$\Delta N = \sqrt{FN}.$$

Looking specifically at the change in energy resolution due to fluctuations in N, we have:

$$\Delta E = \varepsilon \Delta N = \varepsilon \sqrt{FN} = \varepsilon \sqrt{\frac{FE}{\varepsilon}} = \sqrt{F\varepsilon E},$$

which yields the statistical energy uncertainty [8]:

$$\Delta E(rms) = (F\varepsilon E)^{1/2}.$$

This statistical contribution to the resolution can be calculated for any detector material. The Fano factor of germanium is 0.08 [22] and the average energy per electron-hole pair is approximately 2.98 eV [23]. For a γ-ray of energy E = 662 keV, such as that obtained from ^{137}Cs,

$$\Delta E_{Ge}(rms) = 0.399\ keV$$

$$\%\ FWHM = \frac{\Delta E}{E} * 100 = 0.06\%.$$

A similar analysis can be repeated with CZT, which has a Fano factor of F = 0.14 [24] and a pair creation energy of 4.6 eV [25], yielding:

$$\Delta E_{CZT}(rms) = 0.653\ keV$$

$$\%\ FWHM = \frac{\Delta E}{E} * 100 = 0.099\%.$$

These predicted values are significantly smaller than the experimentally determined resolution for the HPGe and CZT detectors. The difference between the experimental values and the statistical FWHM arises from the trapping and recombination of the charge carriers caused by defects in the material. To obtain optimum detection performance, the charge carrier transport must be measured and understood.

In the room temperature detector industry, the μτ-product is a conventional metric of the distance a charge carrier will travel in the detector material before it is trapped or before it recombines [12]. To quantify the amount of charge loss, this product takes into consideration both the mobility and the lifetime of the charge carriers. When this value is multiplied by the electric field in the detector, that calculation yields the trapping length. This enables an understanding of how large a detector can be before charge carriers stop being able to escape the detector volume. Values of μτ for cooled HPGe exceed 1 cm^2/V for both electrons and holes [26], which are the highest values for all known semiconductors. Values of μτ for CZT are in the range of 10^{-2} cm^2/V to 10^{-3} cm^2/V for electrons and 10^{-4} cm^2/V to 10^{-5} cm^2/V for holes [27].

2.2 Selection of the Material to Study

2.2.1 Reasons for choosing α-PbO

Because of the powerful effect that atomic number has on the absorption of γ-radiation, we reviewed many materials with high Z to find suitable prospects for new radiation detector materials. Lead has one of the highest atomic numbers of all stable materials and is the most prevalent heavy metal on the planet. A study of the various lead compounds showed lead oxide, PbO, to be an interesting material.

Upon initial inspection, the phase of lead oxide, α-PbO, is an interesting candidate [10]. Its band gap is sufficiently large (its indirect band gap is ~ 2.0 eV and its direct band gap is ~ 3 eV [11]), and it has very high Z and atomic density, 9.34 g/cm^3 [28], which results in its having large radiation stopping power.

A statistical spread of its theoretical photopeak can be calculated in the same manner that was previously used to calculate the photopeaks for Ge and CZT. Electron-hole pair formation energy for α-PbO can be estimated to be in the 6-8 eV range [10, 18, 20]. The Fano factor for α-PbO is not known. However, a Fano factor is known to increase with increasing band gap [10]. For this reason, we estimate that the Fano factor for α-PbO will be similar to the Fano factor of ~ 0.4 for TlBr, which has a similar band gap [29]. At a γ-ray energy of 662 keV:

$$\Delta E(rms) = (F\varepsilon E)^{1/2} = 1.26$$

$$\%\,FWHM = \frac{\Delta E}{E} * 100\% = 0.19\%.$$

Even for a scenario with a Fano factor of 1, $\Delta E(rms) = 1.99$, and $\%FWHM = 0.3\%$, the energy resolution due to statistical fluctuations for α-PbO is still well within the desired range for room temperature semiconductor detectors (~1%). As was the case for HPGe and Si, the energy resolution will primarily depend upon the charge trapping and recombination in this proposed α-PbO detector.

Lead and oxygen display a rich phase diagram; a section of that is displayed in Figure 8. The oxygen-rich side of the phase diagram shows many complex, and for our purposes undesirable, oxides. Stoichiometric PbO appears in two polymorphs, an α-phase and a β-phase, with the transition from α to β occurring at roughly 485°C [30] (the α-phase is stable below the transition temperature). The α-PbO phase is reported to have a higher μτ-product than the β-phase [11].

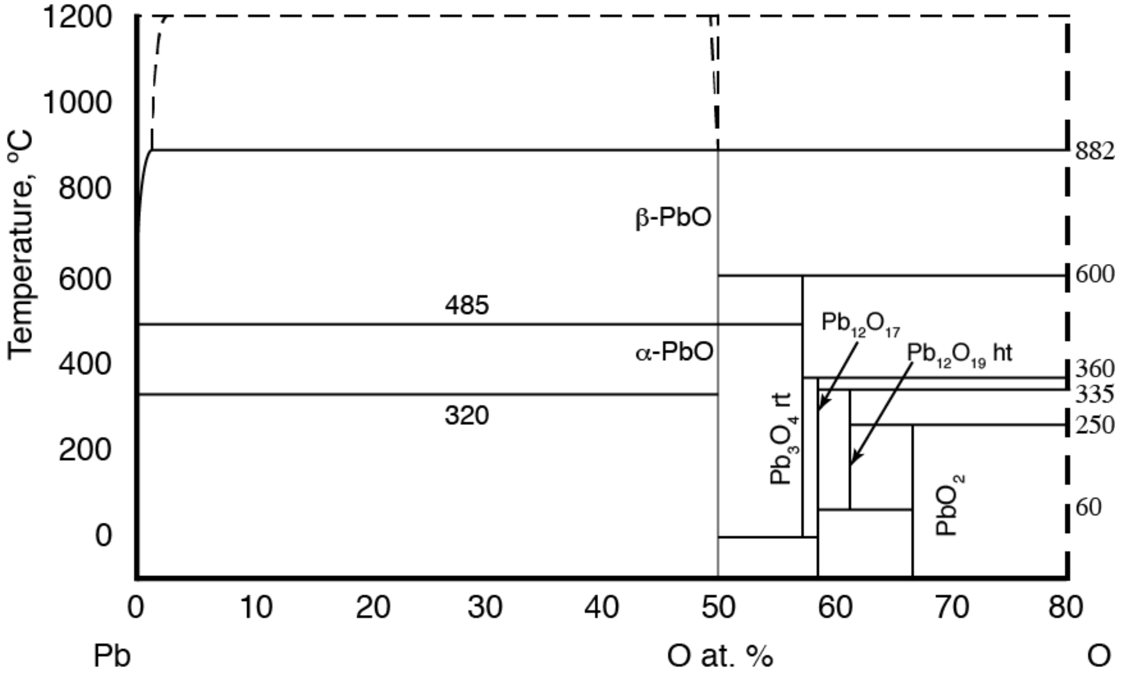

Figure 8: A section of the Pb-O phase diagram showing numerous phases on the oxygen-rich side and only the lead monoxides on the lead-rich side [31].

2.3 History of α-PbO in the Literature

Lead oxide first gained interest in the 1950s and 1960s as a photoconductive layer in television pickup tubes. The initial interest started at the Bell Laboratories, as reported in an article in *Nature* in 1954, which cites an earlier article that was published in the *R.C.A. Review* in 1951 [32]. Each of these articles commented on the usefulness of these lead photoconductive devices to convert both light and X-rays into electrical signals. In the early 1960s, interest in α-PbO as a photoconductive television tube material began to generate interest in PbO as a sensitive X-ray detector. One study discussed the favorable properties of PbO, such as its good photoconductive gains and its high atomic weight, as reasons for its potential use in replacing CdS as a sensitive X-ray photoconductor [18].

By 1966, the PbO-type television tube was being compared to other TV tubes used during that time period [33]. The interest in PbO for television purposes lasted through the 1970s, by which time it was being called a “Plumbicon” [34]. The PbO-type television tube soon began showing up in textbooks and entire chapters were devoted to its physical properties and its operating characteristics [35, 36]. Mention of the Plumbicon can still be found in textbooks as late as 2008, citing its historical use as a PIN junction layer with the ability to provide a fast response and a high quality picture at low light levels [37].

Real scientific interest in PbO as a television tube material petered out over the 1970s and 1980s as new technologies took its place. It wasn’t until 1990 that PbO started to appear again, this time as a potential optical data storage media due to its multiple available phases in multiple valued logic storage for “write once read many” applications [38]. In the early 1990s, PbO also drew interest as a solid lubricant for elevated temperature use in oxidizing environments for air and space vehicles [39], as well as for use as a semiconductor CO_2 sensor [40]. By the mid-1990s, PbO started to gain attention as a potential material for solar energy conversion [41], an interest that would continue to generate future studies, in 2010 and 2012, of PbO as a nanoparticle and thin film photovoltaic material [42, 43].

Interest in PbO for direct X-ray conversion purposes re-emerged in 2005 in the medical imaging market as a replacement for scintillator detectors that were in use at that time [44]. It received further notice in 2005 in a review of radiation detection materials as a material with potential that required further study [10]. Another study, published in 2010, focused on PbO’s potential use in X-ray detection as a replacement for amorphous silicon [45]. In 2013, the most recent study done with PbO was a theoretical modeling of the material as a magnetic semiconductor due to non-magnetic dopants [46].

2.4 Summary

In order to function well, room temperature photoconductive radiation detectors require specific material properties. These properties include: a high atomic number and atomic density, a wide band gap ranging between 1.5 eV and 3 eV, high resistivity in the 10^{12} Ω-cm range, and good transport properties and detector resolution. Lead oxide, α-PbO, meets several of those requirements and more research is necessary to better understand the transport properties of its charge carriers. However, α-PbO has had a rich history dating back to the 1950s, and many previous researchers have expressed great interest in its photoconductivity for a variety of uses.

Chapter 3: Synthesis of Thin Film α-PbO

3.1 Historic Growth of PbO Crystals

In the 1960s, the use of PbO crystals in television pickup tubes generated awareness of and interest in crystals, which led a number of research groups to focus on developing methods to grow single crystals of PbO [47, 48]. Those researchers used a hydrothermal synthesis technique in which a supersaturated, heated, solvent carrying dissolved PbO was allowed to cool under specific pressures in order to precipitate plate-like single crystals of PbO. Some researchers used X-ray Laue patterns to confirm the phase of the materials [47]. In other cases, researchers noted the color of the crystal and assumed that they had produced a single-phase material [48, 49].

Research involving hydrothermal synthesis of PbO tapered off after 1980, at which point researchers focused on another method to grow PbO crystals: pulling crystals of PbO from a molten medium. To obtain tetragonal crystals, PbO was mixed in a solvent to create a solution. Orthorhombic crystals could be pulled from the pure PbO melt using the Czochralski method [50].

To insure the continuation of research on α-PbO as a radiation detector, it is necessary to successfully grow α-PbO crystals in bulk format. Bulk materials will eventually be necessary for the production of γ-ray detectors, should α-PbO prove to be suitable for further testing as a γ-ray detector material.

Thin film growth is useful for preliminary materials research, and it is the primary method of material growth addressed in this dissertation. PbO has a rich history of thin and thick film growth via various methods dating back to the 1950s. At that time, researchers began to study the use of thin film as a photoconductive medium in television pickup tubes [32]. Studies performed in 1961 [51] and 1966 [11] used an evaporation approach. Researchers conjectured about the possibility of a tetragonal phase of crystal growth, but they provided no hard evidence of any phase data [11]. In 1980, another research group revised the technique used to perform reactive evaporation in oxygen and water vapor environments [52]. In that study, SnO_2 was used as the substrate, and the PbO films were either porous or they had very rough surfaces. That study did not report grown phase. Further use of evaporative techniques occurred in 2005 and 2010, yielding samples of both phases in non-oriented, polycrystalline films [45], as well as samples of mixed phase α and β-PbO on amorphous silicon substrates [44].

In the 1970s, PbO gained interest as a barrier layer on Pb metal. In 1974 [53] and 1979 [54], studies examined the use of thermally oxidized ultra-thin layers of PbO on Pb. In general, those layers were found to be the orthorhombic polymorph. In 1994, an electrochemical growth method yielded thick films with an orientation along the [110] direction; however, X-ray diffraction (XRD) did not conclusively exclude other phases [41]. In 2000, researchers grew PbO films using spray deposition, thereby yielding alpha phase polycrystalline films with no preferred orientation [55].

3.2 Introduction to Pulsed Laser Deposition

3.2.1 Background

Pulsed laser deposition (PLD) is a form of physical vapor deposition in which thermal energy, in the form of a laser pulse, is supplied to a target. Vaporized material is ejected from the target into a forward-focused plasma plume that deposits film material onto a substrate [56]. PLD allows for the precise stoichiometric transfer of target materials to a substrate and can produce highly oriented, crystalline films [57].

Initial attempts to grow α-PbO via PLD were not entirely successful. In 1992, the growth of PbO on stainless steel substrates by PLD yielded mixed α-phase and β-phase materials along with metallic Pb [39]. In 1994, further attempts to grow PbO film via PLD yielded films grown on glass slides and quartz substrates that were "predominantly orthorhombic" or "predominantly tetragonal" in phase [40, 58]. In order to achieve high quality PLD film growth of single-phase, highly oriented α-PbO, we must have a full understanding of the parameter space.

3.2.2 Experimental PLD setup

The PLD process begins with the alignment of a high energy, pulsed 248 nm KrF excimer laser, and its subsequent optics, in order to achieve a clean, uniform spot at the target position within a vacuum chamber, as seen in Figure 9. The chamber is evacuated to a background pressure in order to remove the atmosphere and the water vapor through a two-step process. First, the chamber is roughed out using an Edwards GVSP30 dry scroll pump to a pressure of 60 mTorr. Next, the chamber is isolated and a gate valve is opened between the chamber and a CTI Cryo-Torr 8F high vacuum pump. This brings the chamber pressure to a final background pressure of 1 μTorr. As oxygen is introduced, an MKS Baratron® capacitance manometer monitors the pressure inside the chamber. A flutter valve on the cryo pump removes the oxygen at a set rate. Using a feedback loop, a controller opens and closes a needle valve to maintain stable chamber pressure. The target is a compressed pellet composed of stoichiometric PbO powder, commercially available at Alfa Aesar. The final laser spot on the target is an image of the initial rectangular laser aperture. Imaging of the laser aperture through high quality UV mirrors and lenses is required in order to achieve uniform laser intensity across the spot and, therefore, to insure a uniform ablation environment during a single pulse. The spot size can be determined by measuring the dimensions of a single pulse onto a target, which is seen as a blackened area where the material was ablated. When the laser pulse strikes the target, the material vaporizes into a plasma plume. The plume spans the 5 cm distance between the target and the substrate. The material in the plume deposits a thin film onto a crystalline substrate that is cemented to a heating plate kept at the growth temperature. The parameters can be fine-tuned to influence the growth of the film. These parameters include the background oxygen pressure, the temperature of the substrate, the fluence of the laser onto the target, and the mismatch between the substrate and the film in the lattice parameter.

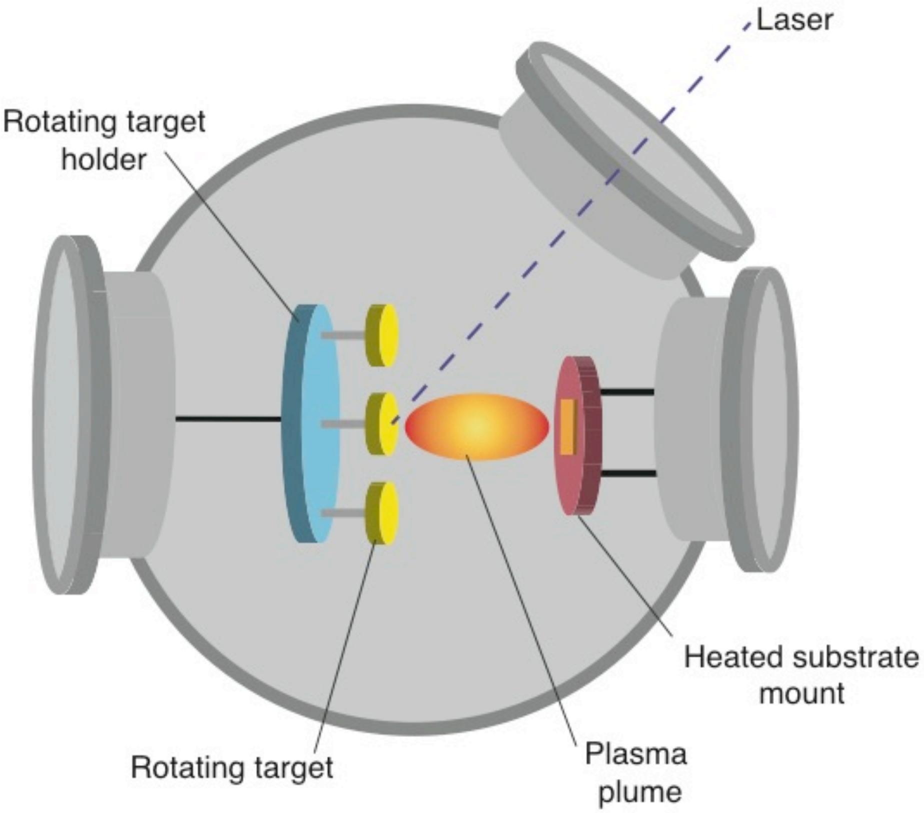

Figure 9: A schematic of a PLD chamber. The pulsed laser enters the chamber through the laser port and strikes the compressed powder pellet that makes the target. The PbO material is vaporized into a plasma plume, which deposits a film onto a heated substrate.

3.3 Characterization of the Thin Films

The crystal structure of the thin films is characterized using a PANalytical X'Pert diffractometer with three modes: 2θ-ω scans, rocking curves, and reciprocal space mapping (RSM).

3.3.1 X-ray diffraction: 2θ-ω scans

The 2θ-ω scan produces a diffraction pattern showing the peaks of all the phases and the orientations that are present in the film and the substrate. Film peak indexing is performed using powder diffraction patterns obtained from CaRIne Crystallography software [59]. This is accomplished by entering the lattice positions of the α-PbO atoms into the software interface. The software then calculates a model of the material, as shown in Figure 10. After modeling the crystal lattice, CaRIne calculates the expected Bragg peaks in a powder diffraction sample. This displays all the possible peaks that may be seen for all orientations of α-PbO. This peak data is compared to the measured peak positions obtained from an X-ray diffraction pattern of a PLD-grown film, and the orientations of the crystallites within the film are determined.

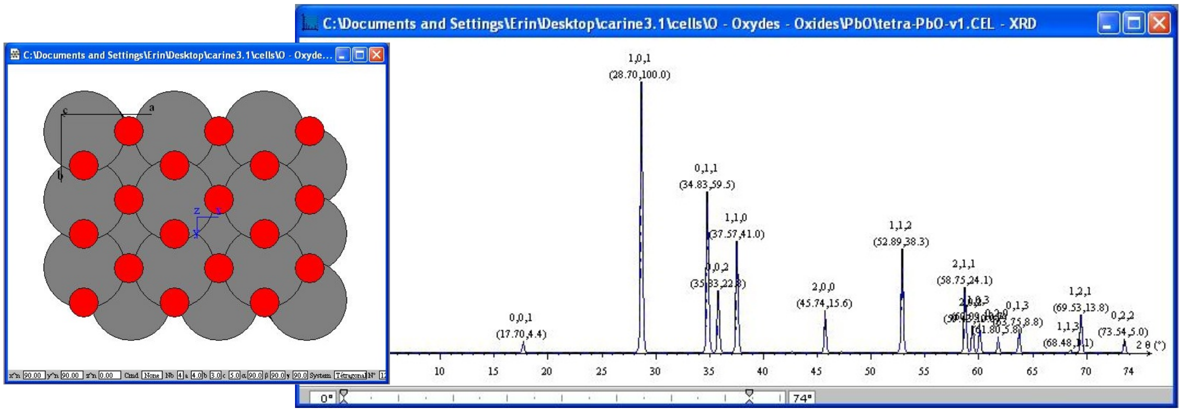

Figure 10: Model of α-PbO and the calculated X-ray powder diffraction pattern containing all possible diffracting orientations [59].

For highly oriented films grown along the [001] direction, the full width at half maximum (FWHM) of the 002 film 2θ peak enables coarse characterization. Choosing to analyze the 002 peak reduces peak broadening due to the instrument function of the diffractometer, which is at a minimum in the 2θ = 30-40° range [60]. As the FWHM of the 002 peak decreases, the crystal quality increases. This is because as the crystallite size increases, the peak broadening due to the crystallite size decreases. This is only helpful as long as the crystallites are small enough so that broadening due to the instrument function does not overwhelm the size broadening.

An analysis of the FWHM of the 2θ curves using the Scherrer equation,

$$L = \frac{K * \lambda_{xray}}{B(2\theta)\cos\theta},$$

yields an estimate of the crystallite size within each of the films. K is a shape factor that depends upon the form of the crystallites within the material. If platelet formation is assumed, due to the layered structure of α-PbO, K = 0.886 [61]. λ_{xray} is the wavelength of the X-ray beam that is used to create the diffraction pattern. B(2θ) is the FWHM of the full peak in 2θ in radians.

The Scherrer equation can only give a lower limit on crystallite size because it does not include peak broadening due to instrument function or strain and defects in the film. Additionally, there is a limit to the crystallite size that this equation can estimate. As a crystallite gets larger, the FWHM of the diffraction peak will become smaller until it is smaller than the broadening caused by the instrument function of the X-ray diffractometer. Consequently, the Scherrer equation is no longer valid for crystallite sizes greater than approximately 100 nm [62].

3.3.2 X-ray diffraction: Rocking curves

Rocking curves enable one to further analyze the quality of a crystal. From this data, we observe the relative mosaicity of the crystal, which is a measure of the disorientation between the crystallites that create the film. A decrease in the rocking curve FWHM infers a decrease in the mosaicity of the crystal. This corresponds to increasing the quality of the film. The rocking curves of the epitaxial films are often noticeably wider than the rocking curves of a single crystal substrate, and the former can be used to determine the relative quality of films during growth process refinement [60]. The 002 film peaks are analyzed for the same reasons stated in Section 3.3.1

3.3.3 X-ray diffraction: Reciprocal space mapping

Reciprocal space mapping (RSM) yields accurate lattice parameters that are used to assess the epitaxial strain in the material. A diffraction peak that has both in-plane and out-of-plane direction components is measured along the ω-direction in incremental steps along the 2θ axis. This creates an intensity distribution over the entire diffraction spot. Any displacement of the spot from its ideal, single-crystal location indicates epitaxial strain between the film and substrate. Converting the location of the center of the peak from reciprocal space to real space yields actual lattice parameters and, therefore, it is possible to identify the effective strain in the film due to lattice mismatch [60].

3.4 The Effect of Parameter Space on Thin Film Growth

Growth of single-phase, high quality, highly oriented films requires optimization of the available growth parameters. The growth parameters considered here include: epitaxial strain, substrate temperature, chamber oxygen pressure, and laser fluence.

3.4.1 The effect of epitaxial strain

Epitaxial strain results in tension or compression in the film, and it can have a profound effect on the growth and quality of the film. To test the effect of epitaxial strain on film quality, very thin films of α-PbO were grown on different substrates, each of which has a different degree of lattice mismatch. The growth conditions were identical for each substrate; the substrate temperature was 495°C, the chamber oxygen pressure was 10 mTorr, and the fluence was 5.5 J/cm^2.

This study used the following substrates: magnesium oxide (MgO), strontium titanate (STO), dysprosium scandate (DSO), and potassium tantalate (KTO). The RSM scans presented in Figure 11 indicate whether the film is strained to the substrate or relaxed. If the material is strained to the substrate, the RSM scans also provide a measure of the effective strain in the material. The 103 diffraction peak from the α-PbO powder diffraction data is known to have good intensity [59] as well as an in-plane and out-of-plane component that is accessible by the X-ray diffractometer. This allows for direct measurement of both the in-plane and the out-of-plane lattice parameters. The FWHM of 2θ and the rocking curve 002 peaks provide a measure of the relative quality of the thin film material, as displayed in Figure 12 and Figure 13. Table 1 presents the lattice mismatch between α-PbO and the various substrates, the FWHM of the 2θ scans of the film 002 peaks, the FWHM of the rocking curves of the film 002 peaks, and the size of the crystallites making up each film.

The lattice mismatch between α-PbO and the MgO substrate appears to be too large for epitaxial growth. Consequently, films grown on MgO are not highly oriented or epitaxial and both the α and β crystalline phases are present. Highly oriented films with a single crystalline phase are achievable on all of the other substrates. Reciprocal space maps of the films grown on the STO, DSO, and KTO substrates are displayed in Figure 11. The RSM peaks for all three of those films are displayed vertically with identical x-axes representing the reciprocal of the in-plane lattice parameter, $1/d_{100}$. The vertical black line marks the reciprocal of the value of the bulk α-PbO in-plane lattice parameter. The film grown on KTO has a peak center to the left of the vertical line. This position corresponds very closely to the lattice parameter of KTO, which implies that the film grown on KTO is strained to the substrate. This means that the strain in the film due to lattice mismatch is not large enough to drive the formation of the defects to relieve the strain.

The films that were grown on the STO and DSO substrates show peak centers that correspond to the bulk lattice parameter of α-PbO. This means that those films have relaxed and they are no longer rigidly strained to the substrates. This can be explained by the greater lattice mismatch between the α-PbO film and the STO and DSO substrates. Greater lattice mismatch creates greater strain in the film. This acts as a driving force for the creation and propagation of defects in the crystalline structure of the thin film. The presence of these misfit dislocations can harm the electronic performance of a semiconductor by introducing diffusion paths for impurities or by creating recombination centers [63].

Table 1: A list of the materials used as substrates for growth of α-PbO. Included are their lattice mismatch and the FWHM of the 2θ peaks and rocking curves for films grown on each substrate under identical conditions.

Substrate Material	Lattice Mismatch (%)	FWHM of 2θ 002 Film Peak	FWHM of Rocking Curve	Crystallite Size (nm)
MgO	6%	No single-phase α-PbO	No single-phase α-PbO	No single-phase α-PbO
STO	1.7%	0.50°	0.65°	16.5
DSO	0.8%	0.32°	0.59°	25.5
KTO	0.3%	0.25°	0.12°	32.6

Applying the Scherrer equation to the 2θ peaks in Figure 12 yields the crystallite size for the films grown on each of the substrates. The α-PbO film grown on STO has a FWHM of 0.40°, which yields a crystallite size of 16.5 nm. The film grown on DSO has a FWHM of 0.29°, which yields a crystallite size of 25.5 nm. The film grown on KTO has a FWHM of 0.24°, which corresponds to a crystallite size of 32.6 nm.

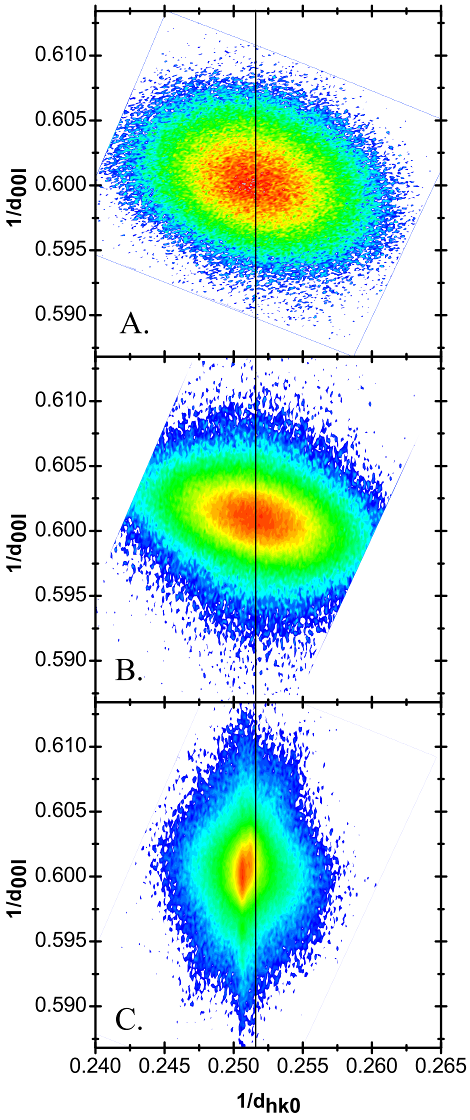

Figure 11: Reciprocal space map of the 103 peak of the α-PbO films grown on the A.) STO; B.) DSO; and C.) KTO substrates. The films are grown with a substrate temperature of 495°C, a chamber oxygen pressure of 10 mTorr, and a laser fluence of 5.5 J/cm^2. The vertical black line marks the reciprocal of the value of the bulk α-PbO in-plane lattice parameter. This plot implies that films grown on STO and DSO are not strained to the lattice, whereas the film grown on KTO is.

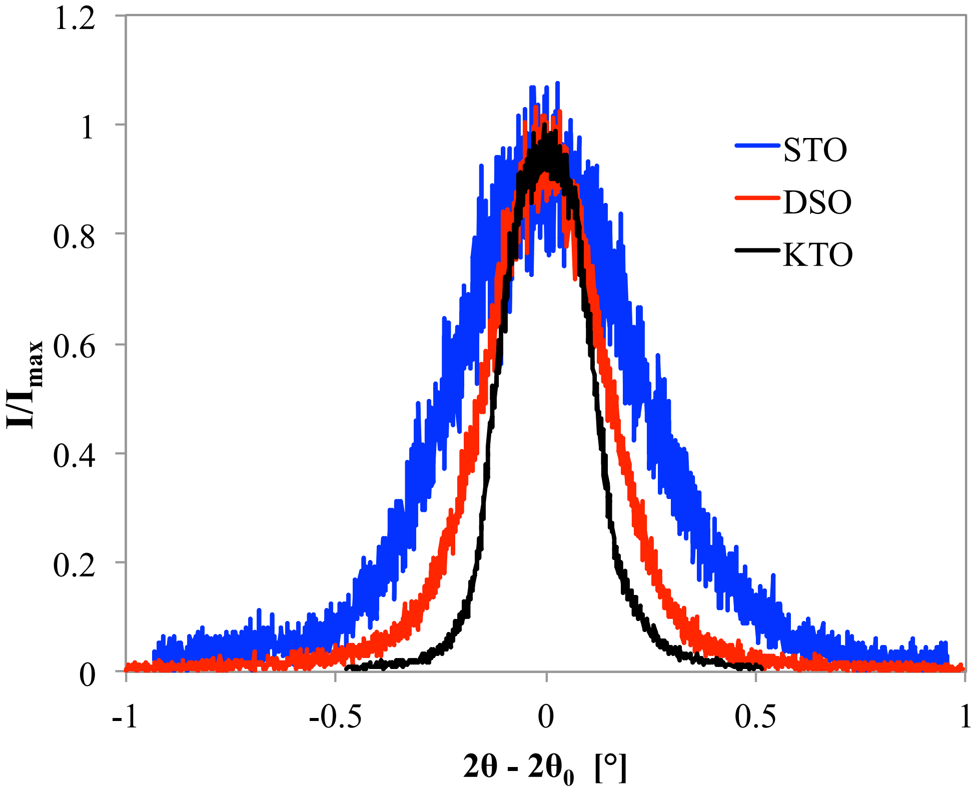

Figure 12: 2θ-scans of the thin α-PbO films grown on STO, DSO, and KTO at 495°C, with a chamber oxygen pressure of10 mTorr, and at a fluence of 5 J/cm^2.

While the substrate-film mismatch does have a noticeable effect on the film quality and the size of the crystallites, it has a remarkable effect on the mosaicity of the films. Figure 13 displays the peak broadening of the rocking curves for the films grown on the STO, DSO, and KTO substrates. The films grown on both the STO and DSO substrates exhibit a large degree of broadening, with a FWHM greater than 0.5°; this implies that a high degree of disorientation exits between these crystallites. The film grown on the KTO substrate shows comparatively low mosaicity, with a FWHM of 0.12°. The small FWHM may be due to the fact that the film grown on the KTO substrate is not relaxed and, therefore, it is held in a rigid alignment with the substrate. The films grown on the STO and DSO substrates exhibit evidence of relaxation that likely leads to a greater disorientation between the crystallites, resulting in broadening of the rocking curves.

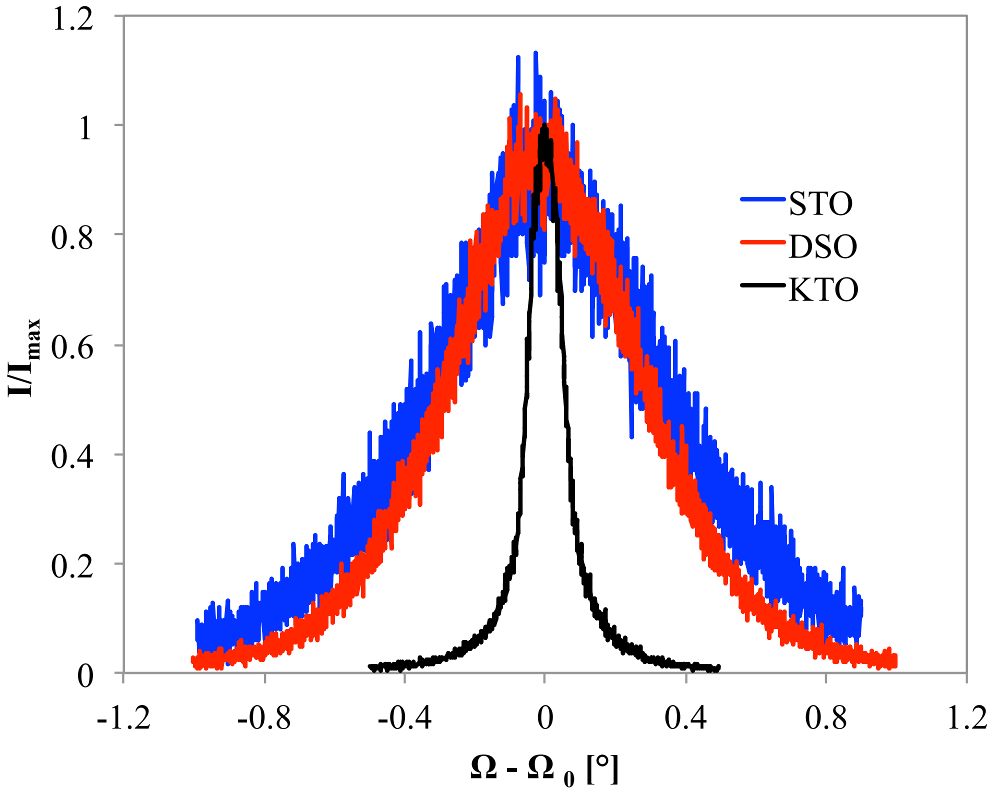

Figure 13: Rocking curves of films grown on various substrates at 495°C, with a chamber oxygen pressure of 10 mTorr, and at a fluence of 5.5 J/cm^2. The substrate materials include: KTO, DSO, and STO.

3.4.2 The effect of substrate temperature

Substrate temperature has a direct effect on adatom surface mobility, adatom desorption and sticking, substrate and film thermal expansion, and the thermodynamics of the film material. All of these factors will affect the quality of the epitaxial film [63]. To examine the effect that substrate temperature has on the quality of the film, α-PbO films were grown at various temperatures on KTO substrates with a chamber oxygen pressure of 10 mTorr and at a fluence of 5.5 J/cm^2.

An analysis of the rocking curves of the α-PbO 002 film peak is presented in Figure 14. As noted, the FWHM narrows as the temperature rises from 465°C to 495°C. At 495°C, the α-to-β transition should have already occurred; however, it is likely that the epitaxial strain from the highly matched KTO substrate made formation of the α-phase more favorable than formation of the β-phase. Above 495°C, the FWHM broadens until the temperature reaches 510°C, indicating degradation in the film quality with increasing temperature. The film grown at 520°C has a narrower FWHM than the film grown at 510°C. Additionally, this film shows the first evidence of β-phase formation in the 2θ-ω scan. Table 2 displays the relationship between the substrate temperature and the rocking curve FWHM.

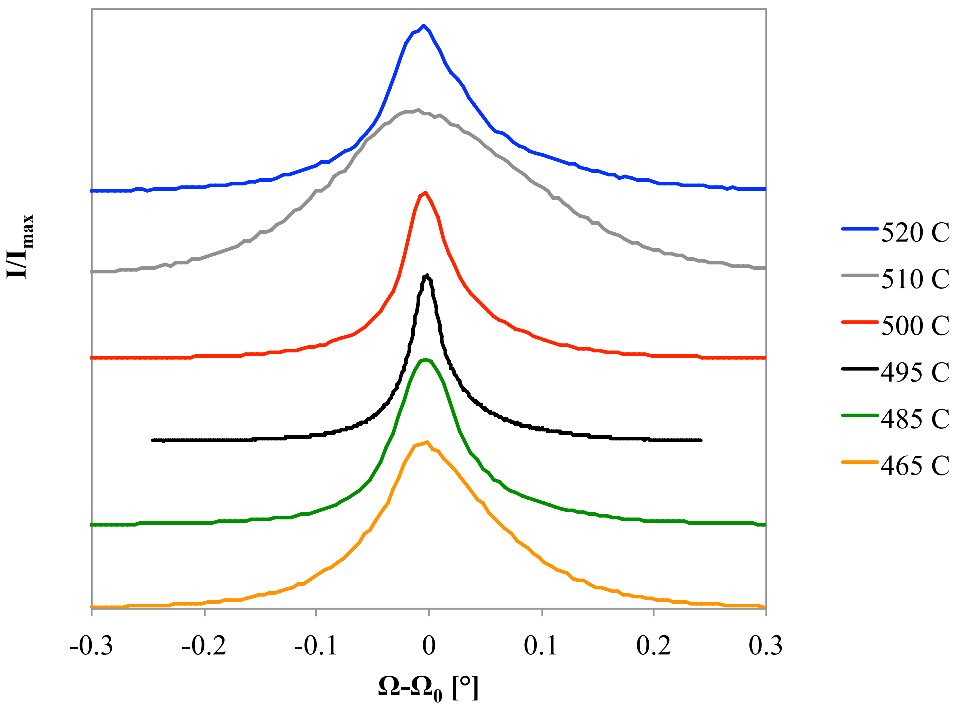

Figure 14: The rocking curves of the α-PbO thin films grown at various temperatures on KTO substrates with a chamber oxygen pressure of 10 mTorr, a fluence of 5 J/cm^2. Rocking curves are offset according to temperature for clarity.

Table 2: Substrate temperature and crystalline quality via analysis of the FWHM of the rocking curves.

Substrate Temperature during Growth	Rocking Curve FWHM
520 °C	0.087
510 °C	0.206
500 °C	0.056
495 °C	0.037
485 °C	0.068
465 °C	0.118

3.4.3 The effect of oxygen pressure

During the growth process, the oxygen pressure in the growth chamber affects oxygen incorporation into the film. This enables fine-tuning of the stoichiometry of the film. Additionally, the oxygen pressure in the chamber during growth can affect the preferred phase of the film. To optimize the oxygen pressure during growth, films are grown at a temperature of 495°C and at a fluence of 5.5 J/cm^2, with the oxygen pressure varying between 0.001 mTorr and 500 mTorr. XRD analysis of the 2θ-ω scans shows the effect of oxygen pressure on the film phase and the crystalline quality.

An initial study of the effect of oxygen pressure was conducted on the films grown on STO substrates. As seen in Figure 15, the films grown below 50 mTorr showed highly oriented, single-phase α-PbO films. However, at pressures of 50 mTorr and higher, the diffraction peaks in the 2θ-ω scans shift, which implies a change in the crystal structure of the material. Indexing these new peaks using CaRIne crystallography shows the formation of the (310) family of planes in Pb_3O_4. This is expected from the phase diagram referred to in Chapter 2, Figure 8, as Pb_3O_4 is the next phase expected at higher oxygen percentages. Therefore, 10 mTorr of oxygen is the preferred oxygen pressure for the growth of α-PbO on the STO substrate.

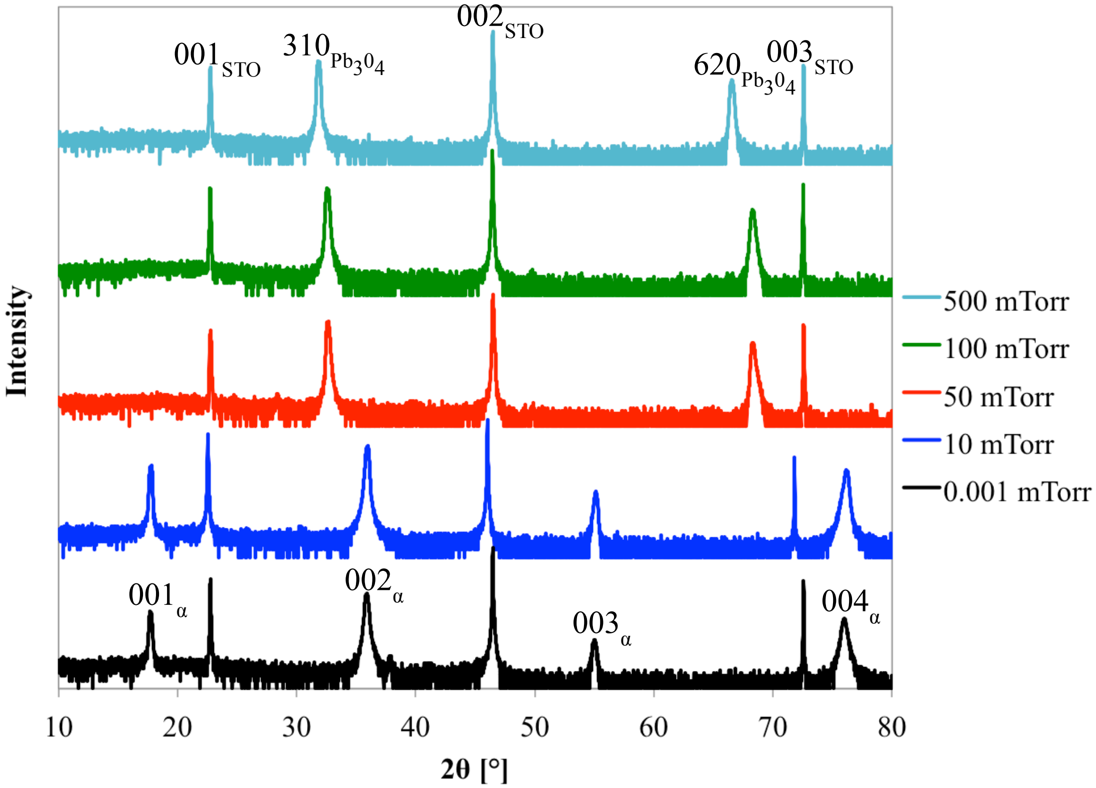

Figure 15: XRD patterns of the α-PbO films grown on the STO substrates at 495°C and at a fluence of 5.5 J/cm^2. During growth, the oxygen pressure varied from 0.001 mTorr to 500 mTorr.

A similar study was performed on the α-PbO films grown on the KTO substrates. Figure 16 exhibits the XRD patterns of the 2θ-ω scans for the films grown at 495°C and at a fluence of 5.5 J/cm^2. During the growth, the oxygen pressure varied from 0.001 mTorr to 500 mTorr. Unlike the films grown on the STO substrate, the films grown on the KTO substrate displayed α-PbO growth at all of the oxygen pressure ranges. The film quality of α-PbO appears to be at an optimum at 10 mTorr of oxygen pressure and it degrades with increasing pressure. At 500 mTorr, a small α-PbO 002 peak is still visible; however, the (320) family of peaks for Pb_3O_4 is now apparent. This work also confirms that 10 mTorr is the optimal oxygen pressure for growth of α-PbO. This result reinforces the important role that the type of substrate plays in the epitaxial growth of α-PbO. The close lattice match between the KTO substrate and α-PbO favors growth of the α-PbO phase and causes suppression of the phase change to Pb_3O_4, despite evidence of its occurrence at oxygen pressures as low as 50 mTorr on less highly-matched substrates.

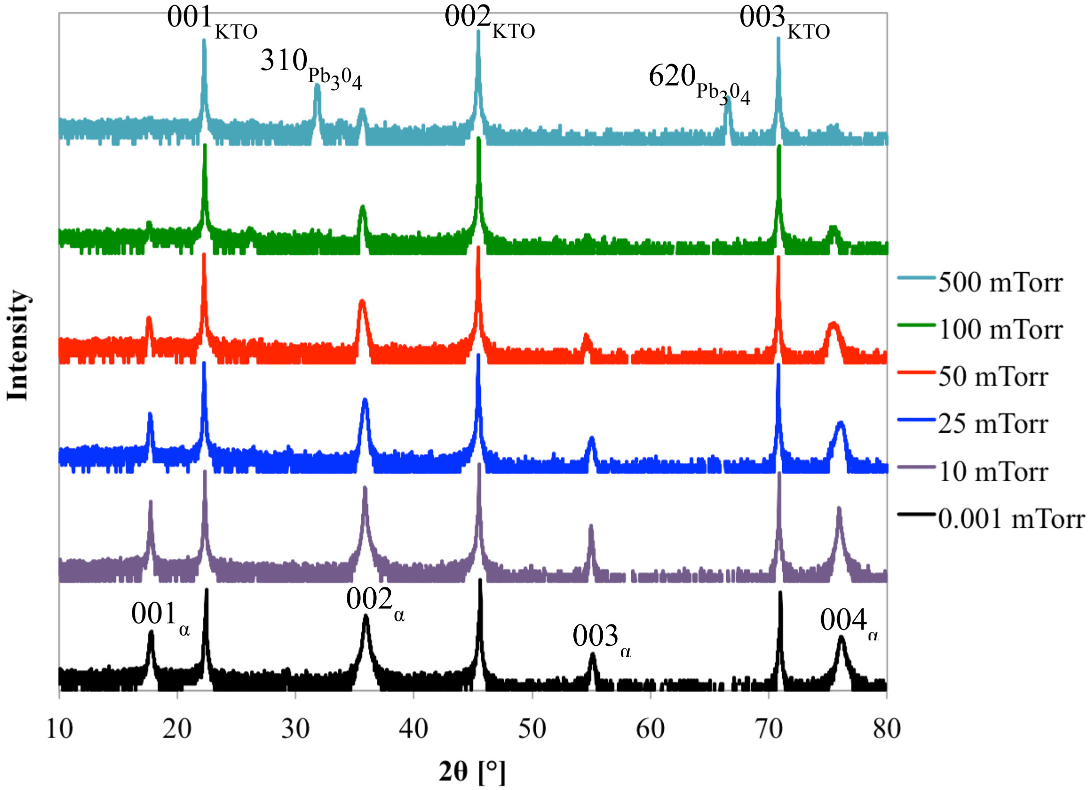

Figure 16: XRD patterns of the films grown on the KTO substrate at a temperature of 495°C and at a fluence of 5.5 J/cm^2. During the growth, the oxygen pressure varied from 0.001 mTorr to 500 mTorr. The phase change, which occurred at 50 mTorr in the films grown on the STO substrate, is suppressed. Only α-PbO is seen in the films grown with an oxygen pressure as high as 100 mTorr. Based on the shape of the 002 film peak, it is clear that 10 mTorr of oxygen pressure is the optimal growth pressure and that film quality degrades as the oxygen pressure increases. At 500 mTorr of oxygen pressure, a small α-PbO peak is still visible and the peaks corresponding to the (320) family of planes of Pb_3O_4 are present.

In order to understand the effect that oxygen pressure has on crystalline quality, a closer inspection of the 002 peak rocking curves of the films displayed in Figure 16 is warranted. The rocking curves of the film grown in the 500 mTorr oxygen pressure condition are disregarded, as that film is most likely predominantly Pb_3O_4. The rocking curve FWHMs that are compared in Figure 17 indicate that 10 mTorr is unquestionably the optimal pressure for growth of α-PbO.

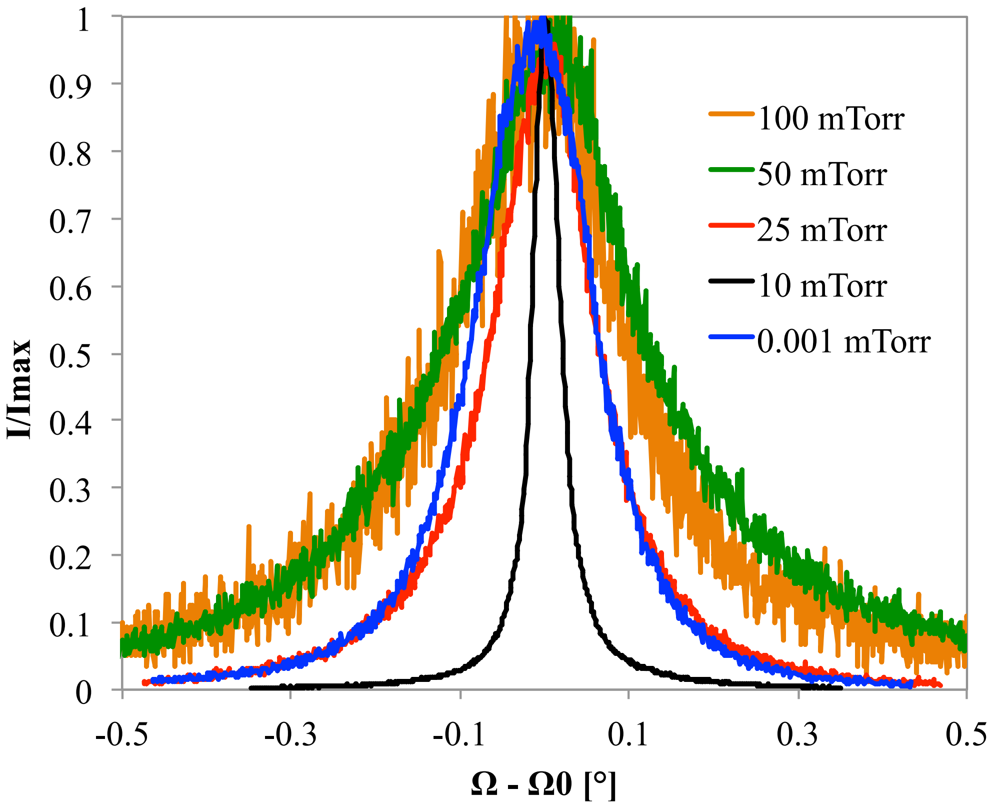

Figure 17: The rocking curves of the α-PbO films grown on KTO, at a substrate temperature of 495°C and at a fluence of 5.5 J/cm^2. During the growth, the oxygen pressure varied from 0.001 mTorr to 100 mTorr.

3.4.4 The effect of laser fluence

During the film growth, the laser fluence onto the target must be large enough to achieve ablation of the material into a plasma plume. If the laser fluence is too low, the target might only experience heating. This leads to evaporation of the target species, in which the evaporation rate of each of the species would depend upon the vapor pressure. Except in materials whose constituents had identical vapor pressures, this would eliminate the ability for stoichiometric transfer to the film. In order to achieve stoichiometric transfer, it is necessary to achieve the minimum threshold fluence. Above this threshold, a small volume of target material absorbs a large amount of energy, causing stoichiometric vaporization. The threshold for ablation depends upon the absorption coefficient of the target and on the wavelength of the laser [56]. Excessive fluence can lead to large boulders of material being splattered onto the film surface and should be avoided. To optimize laser fluence, the films are grown on a KTO substrate with the fluence varying from 2.4 J/cm^2 to 6.1 J/cm^2. The film substrate temperature is 495°C and the oxygen pressure is 10 mTorr. A comparison of the FWHM of the rocking curves of the 002 peaks for each film is shown in Figure 18.

Table 3 presents a comparison of the laser fluence during the film growth and the subsequent rocking curves of the 002 peak of all the films. All the films are free of boulders.

Table 3: Fluence of the laser used for film growth and the resulting FWHM of the rocking curve of the 002 peaks. A decreasing trend in the value of FWHM implies an increasing level in the crystallites' orientations to each other and to the normal substrate surface.

Fluence J/cm^2	FWHM
2.4	0.151
4.52	0.121
5.12	0.097
6.095	0.044

The implications of this data are that, as the laser fluence increases, the FWHM of the rocking curve of the 002 peak decreases, which implies a higher crystalline quality. The KTO substrate rocking curve of the 002 peak is also included in Figure 18. This enables a comparison between the highest quality film peak, grown at 6.095 J/cm^2, and the single crystal substrate. The FWHM of the substrate rocking curve is 0.023°, whereas the FWHM of the film peak is 0.044°. This indicates a very high level of crystal quality.

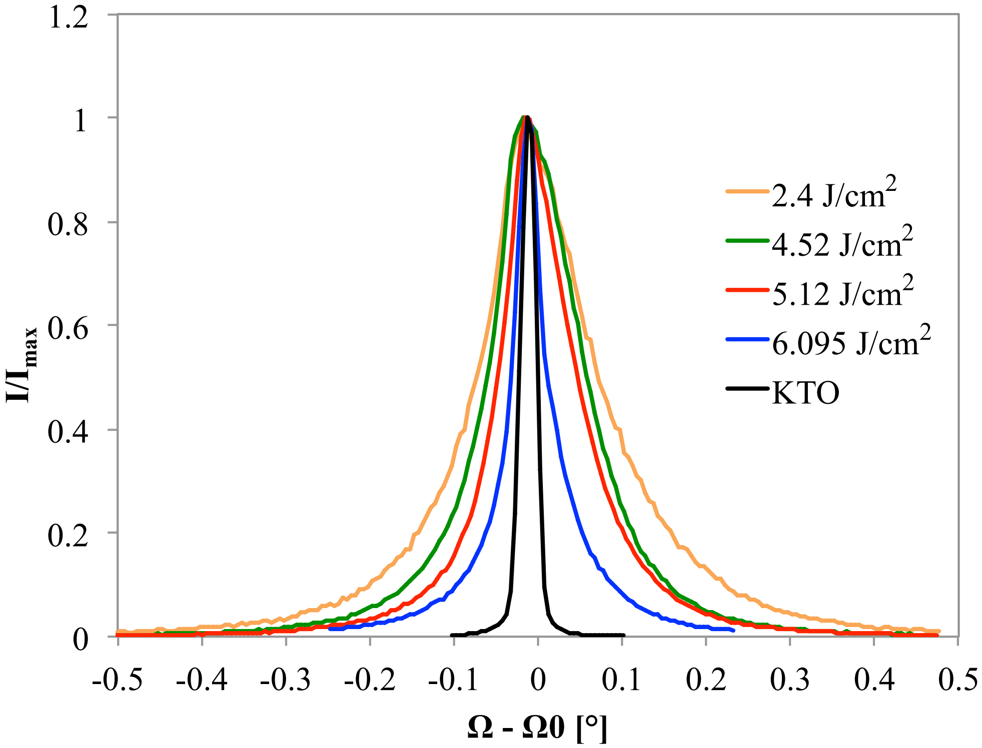

Figure 18: The rocking curves for various fluences during growth of the α-PbO thin films on the KTO substrates.

3.5 Summary

In order to determine the best method for growing epitaxial α-PbO, this chapter focused on a thorough study of the parameter space for pulsed laser deposition thin film growth. Highly oriented films with a single, crystalline α-PbO phase were grown on STO, DSO, and KTO substrates. The film quality is inversely related to the lattice mismatch between the film and the substrate. Therefore, the highest quality films were those grown on the KTO substrate, which has the lowest mismatch. The films with the best crystal quality were grown using a substrate temperature of 495°C, a chamber oxygen pressure of 10 mTorr, and a fluence of ~6 J/cm^2. The films were characterized using X-ray diffraction 2θ-ω scans ranging from 10° to 80°, the 2θ scans and the rocking curves of the 002 peaks, and the reciprocal space mapping of the 103 peak.

Chapter 4: The Optical Properties of α-PbO

4.1 The Optical Measurement of Semiconductors

The measurement of optical properties is a common and important method that is used to determine how light interacts with semiconducting materials. These measurements enable one to determine the band structure and optical constants of a semiconducting material. This chapter focuses on optical absorption spectroscopy, via transmittance and reflectance measurements, and ellipsometry measurements.

4.2 Optical Absorption Spectroscopy

4.2.1 Background and theory of optical absorption spectroscopy

Measuring the absorption spectrum of a semiconductor material is one of the most straightforward ways to probe its band structure. Absorption spectroscopy refers to the measurement of the absorption coefficient of a material as a function of the energy of the incident photons [64]. During the process of absorption, the incident photon energy is transferred to the semiconductor. The photon has a known energy that excites an electron from a lower energy state. If the energy of the photon is smaller than the energy gap between the semiconductor valence band and the conduction band, the light will not be absorbed; instead, it will transmit through the material. If the photon energy is greater than the band gap, the electron is excited into the conduction band from the valence band, leaving an electron-hole pair. Therefore, if one passes light onto a semiconductor film and measures the light transmitted and reflected, analysis of the changes in the transmitted and reflected light can yield information about the transitions occurring within the material with respect to the energy of the incident photon [65].

For any given material, absorption is defined using the absorption coefficient, $\alpha(h\nu)$, which encompasses the relative rate of the decrease in light intensity with respect to the distance the photon has traveled along its propagation path through the material. This study is principally interested in fundamental, or band-to-band, absorption. This refers to the excitation of an electron from the valence band maximum into the conduction band minimum. This is manifested in a sharp rise in absorption, indicating the energy gap of the material.

It is important to note that in comparing the crystal momentum (h/a, where a is the lattice parameter) to the momentum of a photon (h/λ, where λ is the wavelength of light), the photon momentum is negligible compared to the momentum of the crystal. This is because the wavelength of light here is thousands of times as large as the crystal lattice parameter. Therefore, the absorption process can be considered to conserve momentum.

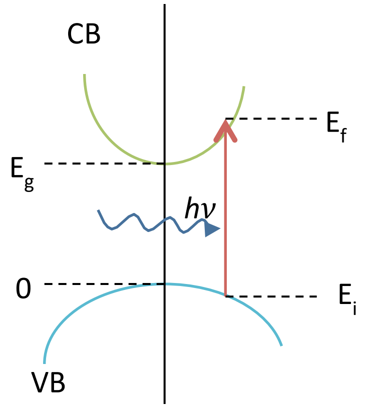

Figure 19: The band structure of a direct gap semiconductor, showing incident, above-gap energy photons exciting an electron from the valence band to the conduction band.

For a direct band gap semiconductor, the band structure of the system can be assumed to form a structure, as shown in Figure 19. Every initial state is associated with a final state. These states have energies E_i and E_f, respectively. For the absorption process, the relationship between them is defined as:

$$E_f = h\nu - |E_i|.$$

An electron with an unexcited energy of E_i, absorbs a photon of energy hν and is excited to an energy state, E_f. Assuming parabolic bands, we can then write:

$$E_f - E_g = \frac{\hbar^2 k^2}{2m_e^*}$$

for the excited state, and

$$E_i = \frac{\hbar^2 k^2}{2m_h^*}$$

for the initial state of the electron. Inserting the last two relations into the relationship between the initial state and the final state, yields:

$$h\nu - E_g = \frac{\hbar^2 k^2}{2}\left(\frac{1}{m_e^*} + \frac{1}{m_h^*}\right).$$

The reduced mass is abbreviated as:

$$\frac{1}{m_r} = \frac{1}{m_e^*} + \frac{1}{m_h^*}$$

Inserting this into the previous equation and solving for k yields:

$$k = \left[\frac{2m_r}{\hbar^2}\left(h\nu - E_g\right)\right]^{1/2}$$

For a direct gap semiconductor, α is proportional to the joint density of states, which has the following form:

$$g_{cv}(h\nu) \propto \sum \delta\left[E_f(k) - E_i(k) - h\nu\right].$$

Performing the summation yields the following form of the density of states:

$$g_{cv}(h\nu) \propto \left[\frac{m_r}{\pi^2\hbar^2}k\right]_{E_f - E_i = h\nu}.$$

Replacing k with the definition derived above yields:

$$g_{cv}(h\nu) \propto \left[\frac{m_r}{\pi^2\hbar^2}\left(\frac{2m_r}{\hbar^2}(h\nu - E_g)\right)^{1/2}\right]_{E_f - E_i = h\nu}.$$

Because α is proportional to the density of states, we can simplify the above equation to:

$$\alpha(h\nu) \propto \left(h\nu - E_g\right)^{1/2}.$$

This yields an expression for the relationship between the absorption coefficient and the band gap for the incident light of the known energy. This expression will enable the determination of the experimental band gap of the semiconductor material, as discussed in Sections 4.2.3-4.2.5.

For an indirect transition, a change in momentum and a change in energy are both required. Therefore, phonon interaction is needed in order to provide the necessary momentum, as shown in Figure 20.

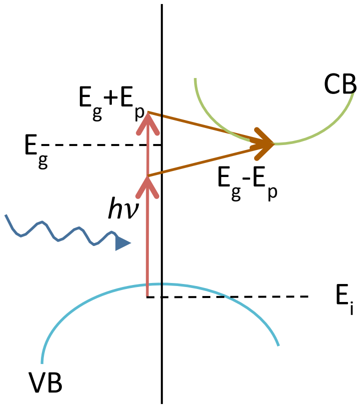

Figure 20: The band structure of an indirect band gap semiconductor, showing incident, above-gap energy photons and the emission or absorption of a phonon in order to excite an electron from the valence band to the conduction band.

In order for the transition from E_i to E_f to occur, a phonon must be absorbed or emitted as shown in the following relationships:

$$h\nu_e = E_f - E_i + E_p$$
$$h\nu_a = E_f - E_i - E_p.$$

In this indirect band gap situation for E_i and E_f, the density of the states becomes:

$$N(E_i) = \frac{1}{2\pi^2\hbar^3}(2m_h^*)^{3/2}|E_i|^{1/2} \text{ and}$$
$$N(E_f) = \frac{1}{2\pi^2\hbar^3}(2m_e^*)^{3/2}\left(h\nu - E_g \mp E_p + E_i\right)^{1/2}.$$

The absorption coefficient is proportional to the densities of the states integrated over the initial states to the final states in all possible combinations separated by hν±E_p, where E_p is the phonon energy. The probability of an interaction with a phonon depends upon the number of phonons, N_p, and the phonon energy. This probability is also a factor in the calculation of the absorption coefficient. The complete form of the absorption coefficient is:

$$\alpha(h\nu) = Af(N_p)\int_0^{-(h\nu - E_g \mp E_p)} |E_i|^{1/2}\left(h\nu - E_g \mp E_p + E_i\right)^{1/2} dE_i$$

For the purpose of this discussion, this can be simplified to reveal the relationship between the absorption coefficient, the band gap energies, and the phonon absorption and emission energies for the known photon energies. Thus, the following form is achieved:

$$\alpha(h\nu) \propto \left(h\nu - E_g \pm E_p\right)^2.$$

This reviews the calculation of the dependence of the absorption coefficients on the band gap energy for the known incident energy and for both the direct band gap and indirect band gap semiconductors. These relationships enable one to determine the experimental band gap of the semiconductor thin films. In order to analyze the material band gap, the absorption coefficient must be measured.

A number of factors lead to the large range of reported values for the band gaps of α-PbO. These factors include: various material formats, various stoichiometry defects, phase mixing, and human interpretation of the data. Studies of optical absorption and the band gap of α-PbO have reported using materials produced via evaporation [11], spray pyrolysis [55], vacuum thermal evaporation [45], and single crystal growth [47]. The reported values for the band gap of α-PbO range from 1.7 eV to 2.3 eV for the indirect band gap and 2.6 eV to 3.38 eV for the direct band gap [11, 47, 55, 66].

4.2.2 Experimental setup

Study of the absorption coefficient, or absorption spectroscopy, is achieved through the measurement and analysis of the transmission and reflection spectra, which is discussed in Sections 4.2.3 and 4.2.4. Transmission and reflection spectroscopy are measured experimentally using a PerkinElmer Lambda 950 UV-Vis spectrophotometer. This system measures the transmitted and reflected light of a sample and compares it to a reference beam to provide reflectance and transmittance data.

The Lambda 950 includes two light sources, a tungsten halogen bulb and a deuterium bulb; these light sources cover the wavelength range of interest, which is 300 nm to 800 nm. The light from the source passes through a monochromator so that light with a narrow bandwidth is incident on the sample. The transmitted light passes through optics and into a photomultiplier tube (PMT) detector, recording a transmittance spectrum. A detailed schematic can be seen in Figure 21.

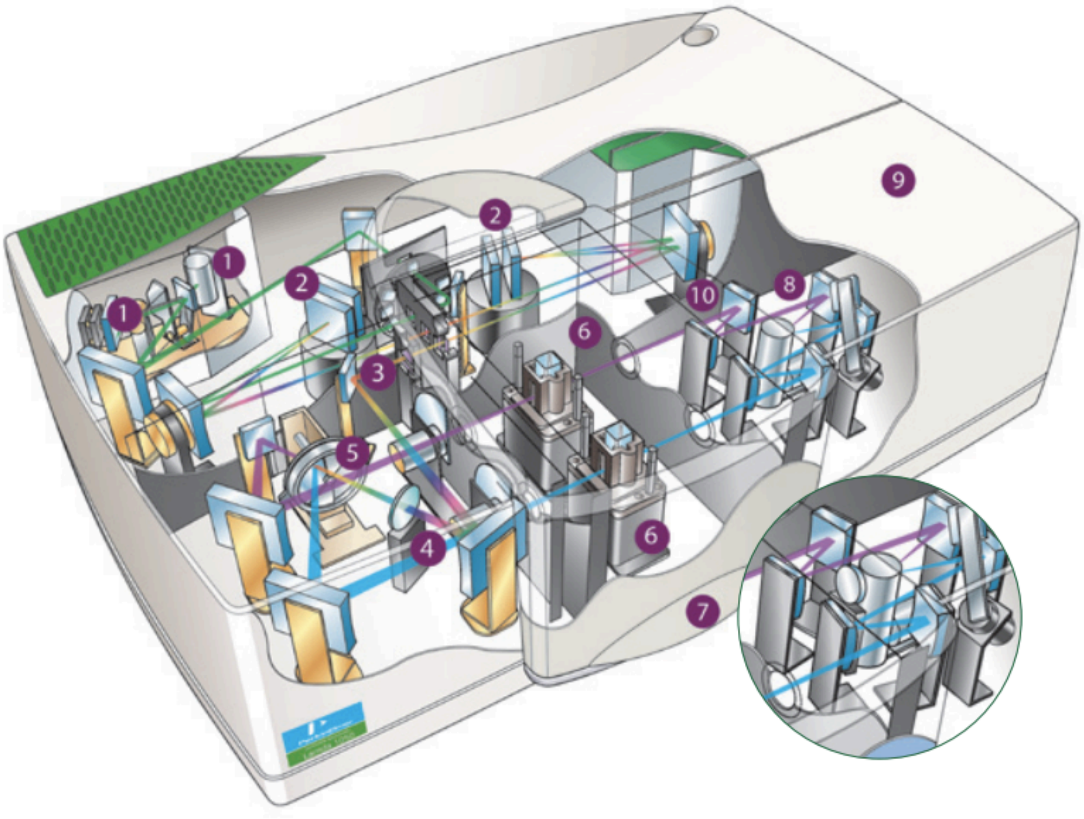

Figure 21: A schematic of the PerkinElmer Lambda 950 UV-Vis spectrophotometer used for transmission and reflection spectroscopy [67]. The light enters from the light sources shown in step 1. The wavelength is selected by the monochromator in step 2. Beam shaping and chopping occur in steps 3-5. At step 6, the sample attenuates the light in the sample beam. The reference beam is nearby. The attenuated light is incident on the detector at step 8.

The Universal Reflectance Accessory (URA) measures the reflected light. This unit is an attachment on the Lambda 950 and it takes the monochromatic light and applies it to the sample surface. Because it is not possible to both apply and measure light normal to the sample surface, the light is applied at an 8° angle. The detector then measures the reflected light. A schematic of the system is displayed in Figure 22. The system software adjusts the data to remove the effects from the angle of reflection.

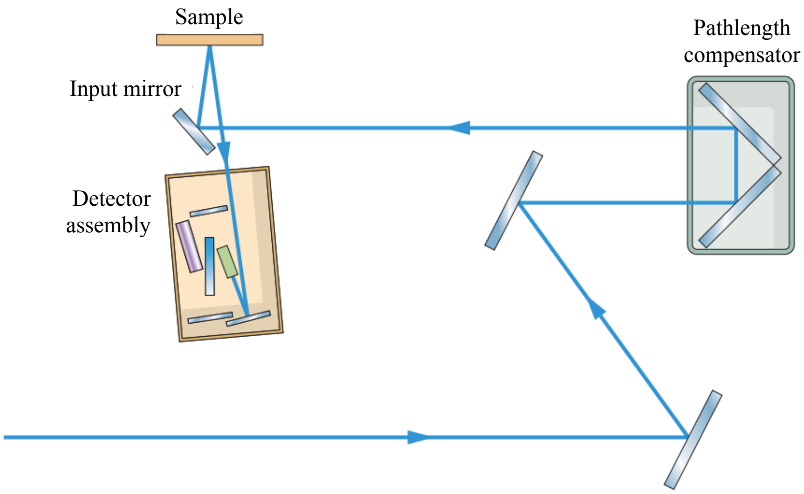

Figure 22: A schematic of the light path in the Universal Reflectance Accessory (URA) used for the reflectance measurements [68]. The light travels through the sample compartment shown in Figure 21 and then enters the URA. The beam path is reflected by a number of mirrors. After the final mirror, the beam is applied to the sample at an angle of 8°, then the beam from the sample surface reflection is reflected to the detector to record the reflectance of the sample.

The sample consists of a thin film of α-PbO on a KTO substrate that has two polished sides. Two black plates, which have the same size hole through their center, are mounted in the sample compartment of the Lambda 950 and aligned to the beams in the sample and the reference paths. Before the measurement is taken, the system records a measurement with nothing in the sample or the reference beams. This is known as the measurement background. The thin film sample is then mounted over the hole in the black plate in the sample beam. The transmission measurement can then be performed. The same sample is then placed face down on the URA and reflection spectroscopy is conducted.

4.2.3 Transmission spectroscopy

Transmission spectroscopy is a part of the measurement that is required to calculate the spectral absorption coefficient of a material. During a transmission measurement, light is incident on the sample and the light that is transmitted is measured as a function of the wavelength, as shown in Figure 23. The sample being measured has physical properties that define it, such as the reflection coefficient at each surface, R, the absorption coefficient, α, the complex index of refraction, n+ik, and the thickness, d, of the sample.

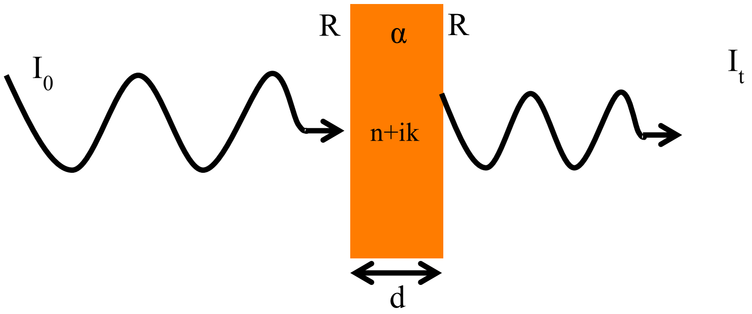

Figure 23: A schematic of a transmission measurement.

Light intensity, I_0, is incident from the left, interacts with the material, and transmits to the right with intensity, I_t. The transmittance is defined as:

$$T = \frac{I_t}{I_0}.$$

However, reflections from both the front and the rear surfaces of the material must be taken into account. The light incident from the left is transmitted through the sample, but some percentage is reflected at the initial surface with intensity equal to:

$$I_{r1} = R_1 I_0$$

where R_1 is the reflection coefficient on the first air-film interface. Therefore, what is transmitted is the fraction that is not reflected:

$$I_{t1} = (1 - R_1) I_0$$

This light travels into the film and experiences absorption by the material according to the Beer-Lambert Law:

$$I_t = I_0 exp(-\alpha d).$$

When it reaches a depth, d, where the film and the substrate interface, a percentage is again reflected with intensity equal to:

$$I_{r2} = R_2 (1 - R_1)\, I_0\, exp(-\alpha d).$$

This reflected light then travels back to the front surface where part of it is reflected back into the film and part is transmitted out of the film, and so on. In order to explain the behavior of the transmission data, these multiple reflections must be taken into account. Additionally, it is now clear that some percentage of the incident light will be lost to the transmission measurement by reflection instead of the absorption in the material. The reflected light must also be measured and taken into account in order to obtain a total view of how the light interacts with the film. Further explanation of the reflection process will be discussed in Section 4.2.4. The addition of all the individual transmitted intensities yields a relation for transmittance:

$$T = \frac{(1 - R_1)(1 - R_2) e^{-\alpha d}}{1 + R_1 R_2 e^{-2\alpha d} - 2\sqrt{R_1 R_2} e^{-\alpha d} \cos\varphi},$$

where $\varphi = 4\pi n d/\lambda$ [69]. When the film is thin enough that the multiply reflected intensities are still coherent, constructive and destructive interference will occur, causing a fringe pattern known as the Fabry-Perot fringes.

For general analysis of the material, a number of simplifications can be made that reduce the complexity of the equation for transmittance. This simplification yields the following transmission relation:

$$T = \frac{(1 - R)^2 e^{-\alpha d}}{1 + R^2 e^{-2\alpha d}}.$$

Solving for the absorption coefficient yields:

$$\alpha = -\frac{1}{d}\ln\left(\frac{\sqrt{(1-R)^4 + 4T^2R^2} - (1-R)^2}{2TR^2}\right).$$

This equation can be further simplified in cases when the product of α and d is large. When this is true, the denominator of the equation for T can be neglected [65], yielding:

$$T = (1-R)^2 e^{-\alpha d}.$$

Solving for this simplified absorption coefficient yields:

$$\alpha = -\frac{1}{d}\ln\left[\frac{T}{(1-R)^2}\right]$$

This equation enables the calculation of the absorption coefficient from the measured transmission and the reflection spectra. The reflection spectrum will be addressed in the next section. The transmission spectrum data is plotted in Figure 25. At energies below the band gap of a semiconductor, the transmission should be quite high. However, the transmission spectra from α-PbO films also include transmission through the substrate. While the KTO substrate is very transmissive in the energy range of 1.5-3.5 eV, it is not 100% transmissive, as can be seen in Figure 24.

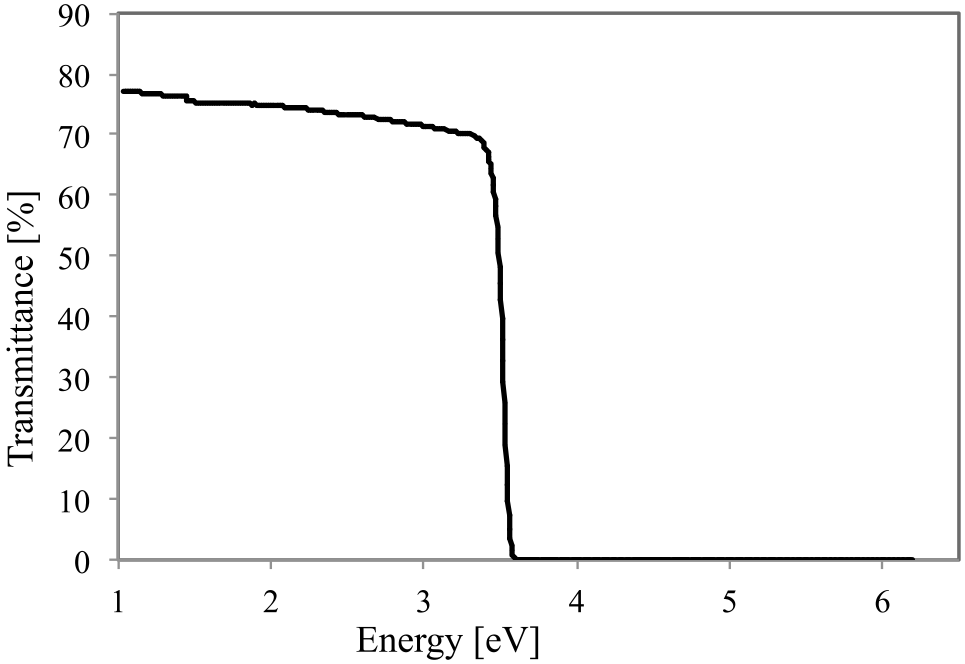

Figure 24: Transmission spectrum for the KTO substrate.

As the energy range nears 3.5 eV, the transmission from the KTO substrate drops precipitously to 0%. Therefore, spectra from α-PbO that is grown on the KTO substrate with energies above 3.5 eV will not provide any information, and they are not collected. In the KTO substrate, the strong decrease in absorption at energies below 3.5 eV is due to the excitation of charge carriers across the band gap. The transmission spectrum from the α-PbO thin film grown on the KTO substrate is displayed in Figure 25. As expected, the transmission at low energy is high, at ~60%. Additionally, the spectrum displays the oscillations that arise from multiple reflections within the film, as is expected from a thin film. Additionally, the fall off of the transmission, or the onset of the absorption, is much more gradual than it is in the KTO substrate. This implies that α-PbO is an indirect gap material [70]. Further measurement and analysis will confirm this.

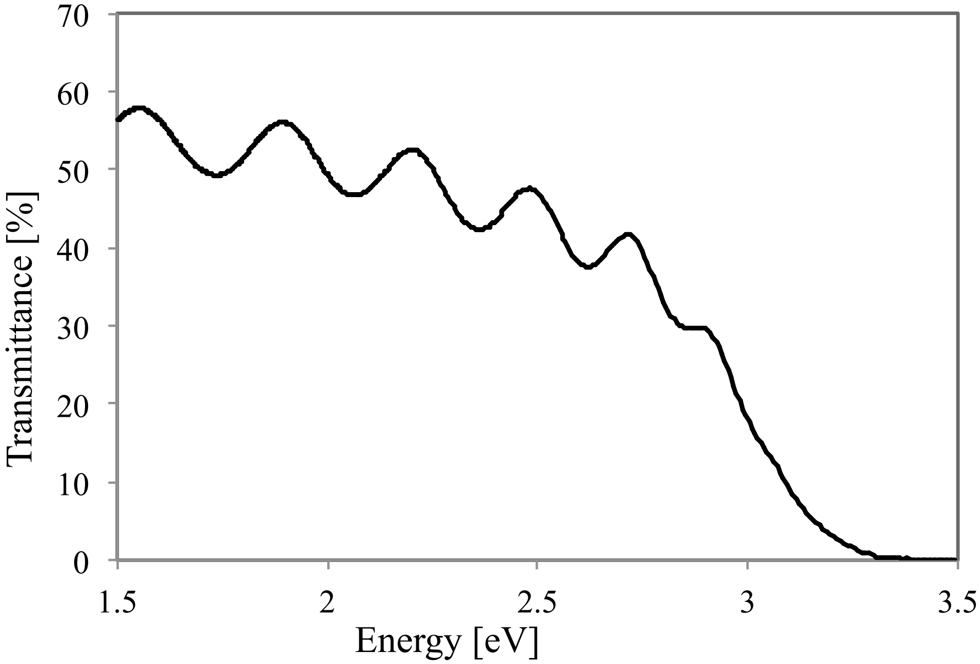

Figure 25: Transmission spectrum from the α-PbO thin film on the KTO substrate as a function of energy.

4.2.4 Reflection spectroscopy

Reflection measurements are needed to complete the calculation of the absorption coefficient spectrum. They can also be useful in determining the thickness of the thin film. The reflectance is defined as:

$$R = \frac{I_r}{I_0}.$$

In can also be defined in terms of the Fresnel reflection coefficients via the following relation:

$$R = \frac{r_1^2 e^{\alpha d} + r_2^2 e^{-\alpha d} + 2 r_1 r_2 \cos(\varphi_1)}{e^{\alpha d} + r_1^2 r_2^2 e^{-\alpha d} + 2 r_1 r_2 \cos(\varphi_1)}$$

where

$$r_1 = \frac{n_0 - n_1}{n_0 + n_1}, \qquad r_2 = \frac{n_1 - n_2}{n_1 + n_2}, \qquad \varphi_1 = \frac{4\pi n_1 d \cos(\phi')}{\lambda},$$

and

$$\phi' = \arcsin\left[\frac{n_0 \sin(\phi)}{n_1}\right].$$

This form of the reflectance, R, has oscillations that reach a maximum or minimum at particular wavelengths defined by:

$$\lambda = \frac{2n_1 d \cos(\phi')}{m},$$

where, m is an integer denoting the order of the oscillation. The separation between two of the maxima or minima in the reflection spectrum gives the thickness of the thin film. To extract this thickness, it is easier to work with the reflectance as a function of wavenumber, λ^{-1}. This will look similar to the plot of the reflectance versus the energy spectrum shown in Figure 26, which also has a $1/\lambda$ dependence.

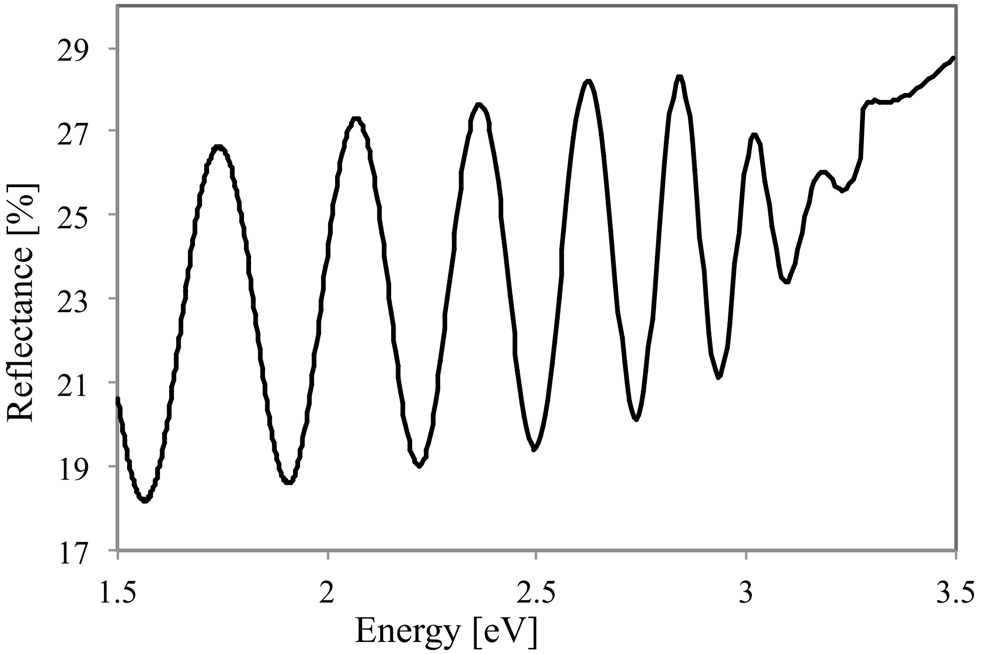

Figure 26: Reflection spectrum of α-PbO as a function of energy.

The above equation will have error due to the fact that it neglects the extinction coefficient, k. For α-PbO, k is at a minimum at the low energy range of the spectrum. Therefore, two of the lowest energy minima will be used for this calculation. Rewriting the above equation in terms of wave number yields:

$$\lambda^{-1} = \frac{m}{2n_{1,m} d \cos\phi'},$$

where $2n_{1,m}\cos\phi' = 2\sqrt{n_{1,m}^2 - n_0^2 \sin^2\phi}$. The index of refraction, $n_{1,m}$, refers to the specific value of n in the film at the mth minimum wavelength. The equation can be further simplified because the refractive index of air $n_0 = 1$. Normal incidence can be assumed, so $\sin^2\phi = 0$ and $\cos\phi' = 1$. Subtracting the wavenumber for two minima yields:

$$\lambda_2^{-1} - \lambda_1^{-1} = \frac{m+1}{2n_{1,2}d} - \frac{m}{2n_{1,1}d} = \frac{1}{2d}\left[\frac{m+1}{n_{1,2}} - \frac{m}{n_{1,1}}\right].$$

Solving this equation for d and m = 1 yields:

$$d = \frac{1}{2(\lambda_2^{-1} - \lambda_1^{-1})}\left[\frac{2}{n_{1,2}} - \frac{1}{n_{1,1}}\right].$$

The wavenumber values for the two lowest energy minima are: $\lambda_1^{-1} = 1.26\ \mu m^{-1}$ and $\lambda_2^{-1} = 1.54\ \mu m^{-1}$. The index of refraction values calculated using ellipsometry, which are discussed in Section 4.3, include: $n_{1,1} = 2.433$ and $n_{1,2} = 2.674$. These yield a value for the thickness of the film that is ~ 600 nm.

4.2.5 Absorption spectroscopy

We now calculate the absorption coefficient spectrum based on the measured transmission and the reflection spectra using the equation:

$$\alpha = -\frac{1}{d}\ln\left[\frac{T}{(1-R)^2}\right].$$

Figure 27 displays the results of this analysis. To further understand the band structure, analysis of the square and square root of the absorption coefficient is warranted.

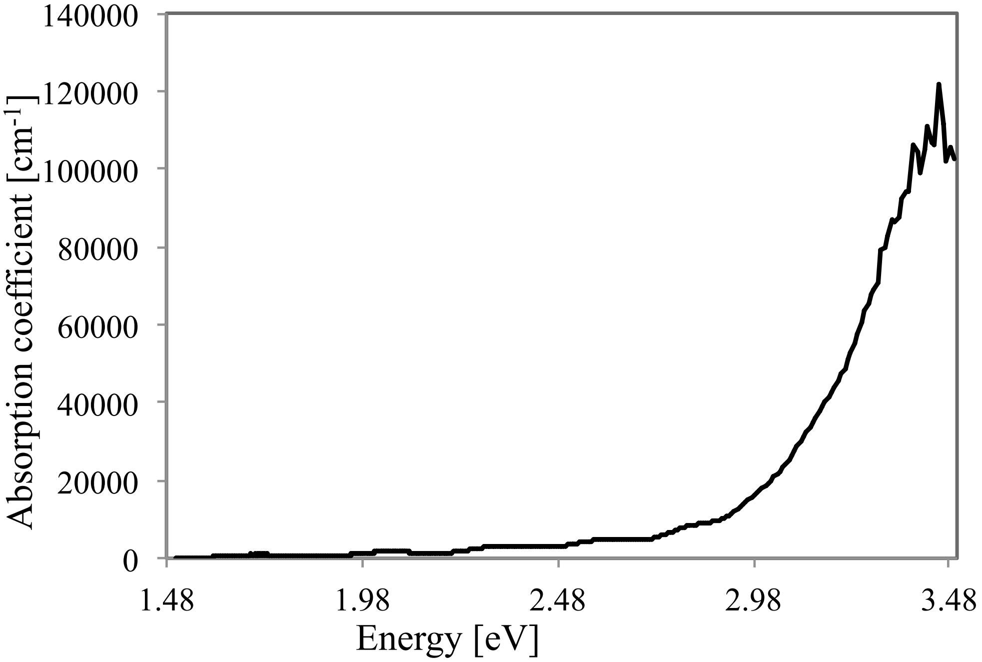

Figure 27: Absorption coefficient of α-PbO.

We previously derived relationships between the absorption coefficient and the indirect band gaps and the direct band gaps of the material. For the direct gap situation, the band gap of the material is linearly dependent on α^2 as follows:

$$\left(h\nu - E_{g,dir}\right) = \alpha^2.$$

When the square of the absorption coefficient is plotted, the direct absorption event will appear to be linear. Fitting a line to that region and extrapolating to $\alpha^2 = 0$, will leave $E_{g,dir}$ equal to the photon energy, hν, at that point. In this way we can measure the direct band gap of the material from a plot of the squared absorption coefficient. A plot of the square of the absorption coefficient versus energy is shown in Figure 28.

After a gradual onset, a strong absorption takes over and a linear region is apparent. The linear fit is plotted in red. The fit line reaches the energy axis, where the square of the absorption coefficient is zero, and it marks the energy of the direct band gap transition. This energy is $E_{g,dir}$ = 3.2 eV.

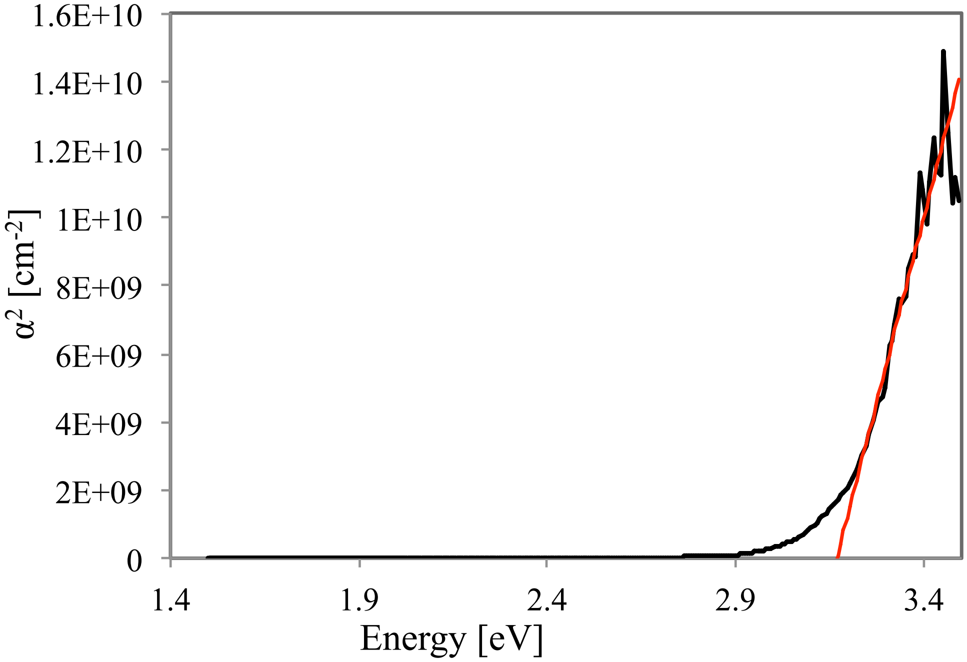

Figure 28: The square of the alpha coefficient spectrum of α-PbO. The red line is a linear fit to the portion of the spectrum that denotes a direct transition. The value of energy where the fit line crosses the axis is the direct band gap energy for the film. In this case, E_g = 3.2 eV.

The same calculation can be done for the indirect band gap situation. The indirect band gap energy is linearly related to the square root of the absorption coefficient, as follows:

$$\left(h\nu - E_{g,ind} \pm E_p\right) = \alpha^{1/2}.$$

In this case, we can assume that the energy of the phonon is negligible compared to the energy of the band gap and, indeed, the equipment measuring the absorption spectrum is not sensitive enough to pick up the effect that the phonon energy has on the absorption spectrum data. Therefore, we can simplify the indirect gap case to:

$$\left(h\nu - E_{g,ind}\right) = \alpha^{1/2}.$$

A plot of the square root of the absorption coefficient spectrum will have a linear region where the indirect absorption takes place. Fitting a line to this region, and extrapolating to $\alpha^{1/2} = 0$, will leave $E_{g,ind}$ equal to the photon energy, hν, at that location.

The plot of the square root of the absorption coefficient versus energy is presented in Figure 29. A gradual onset of absorption starts at an energy near 2 eV. The Fabry-Perot fringes complicate the analysis of the data; however, a general linear fit can be made through the center of the fringes. When the linear fit reaches the energy axis, the square root of the absorption coefficient is zero, and the indirect band gap energy is determined to be $E_{g,ind}$ = 1.9 eV.

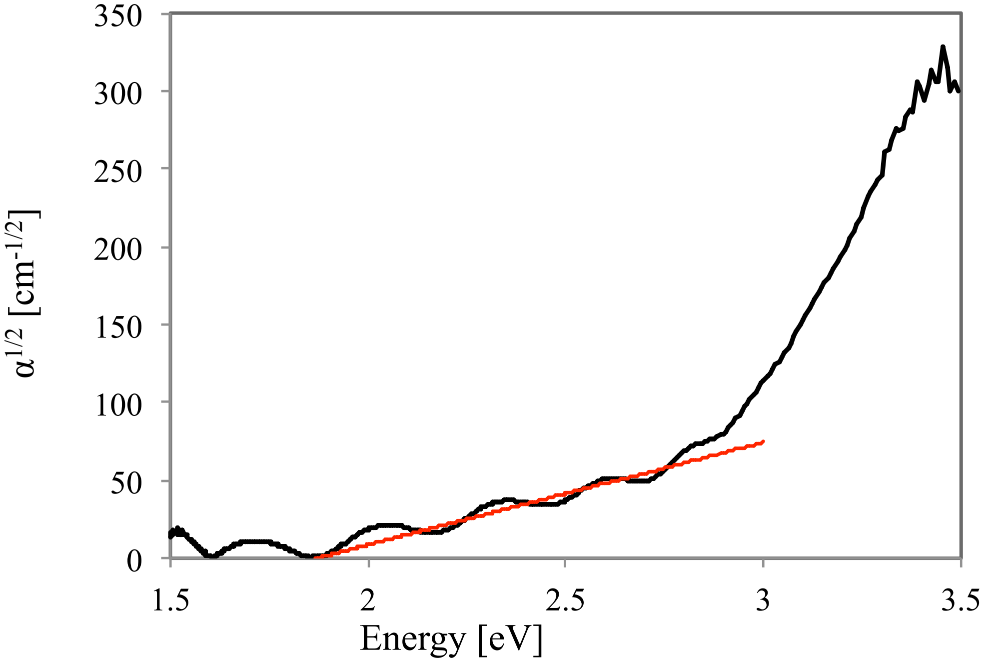

Figure 29: The square root of the absorption coefficient of α=PbO. A linear fit to the onset around 2 eV denotes the indirect transition. Due to constructive and destructive interference between the reflections on the front and back surface of the film, the Fabry-Perot fringes complicate the analysis. The linear fit crosses the energy axis giving a value for the indirect band gap of Eg = 1.9 eV.

4.3 Spectral Ellipsometry

4.3.1 What is ellipsometry and why should it be used?

When polarized light strikes a surface at an angle causing a specular reflection, it experiences a change in its polarization state. Ellipsometry is a form of optical spectroscopy that measures the change in the polarization state of light reflected off a sample's surface. During measurement, a sample surface is illuminated using linearly polarized light. Upon reflection, the polarization state of the light changes to elliptical polarization. The ellipsometer measures the change in the phase and amplitude of both orthogonal electric field components. The data is fit to a model that enables the user to calculate the physical properties of the thin film [71].

Ellipsometry has the advantage of high sensitivity even for extremely thin films. It depends upon the measurement of the polarization of light instead of the intensity of the light source. Consequently, it is unaffected by fluctuations in the light source. Therefore, it is a high precision technique that is capable of measuring very thin films with high sensitivity [71]. Additionally, the measurement is contactless and non-destructive, making it a convenient way to study a material [72].

This measurement is commonly used to determine the complex dielectric function:

$$\varepsilon(\omega) = \varepsilon_1 + i\varepsilon_2,$$

which is used to calculate the complex index of refraction,

$$\tilde{N} = \tilde{n} + i\tilde{\kappa}.$$

The refractive index, n, determines how light is refracted upon entering a material. The value, κ, is the extinction coefficient and it determines the attenuation of light that enters the material. κ is particularly important in absorbing materials, such as semiconductors or metals. The complex dielectric function and the complex index of refraction are related to each other in the following manner [71]:

$$\varepsilon_1 = n^2 - \kappa^2,$$

$$\varepsilon_2 = 2nk,$$

$$n = \left[\frac{\varepsilon_1 + (\varepsilon_1^2 + \varepsilon_2^2)^{1/2}}{2}\right]^{1/2},$$

$$\kappa = \frac{\varepsilon_2}{2n}.$$

The polarization of the incident and the reflected light is measured as a function of the angle of incidence, ϕ, and the frequency of light, ω [73]. The reflectance of each of the two components of polarization, s-polarized light (perpendicular to the plane of incidence) and p-polarized light (parallel to the plane of incidence), are related to the Fresnel reflection coefficients through:

$$R_s = |r_s|^2$$

$$R_p = |r_p|^2.$$

The Fresnel coefficients have the form:

$$r_s = \frac{\widetilde{N}_a \cos\phi - \widetilde{N}_s \cos\phi_t}{\widetilde{N}_a \cos\phi + \widetilde{N}_s \cos\phi_t}$$

and

$$r_p = \frac{\varepsilon_s \widetilde{N}_a \cos\phi - \varepsilon_a \widetilde{N}_s \cos\phi_t}{\varepsilon_s \widetilde{N}_a \cos\phi + \varepsilon_a \widetilde{N}_s \cos\phi_t}.$$

in which

$$\widetilde{N}_s \cos\phi_t = (\varepsilon_s - \varepsilon_a sin^2\phi)^{1/2}.$$

In the above equations, ε_s and $\widetilde{N}_s$ are the complex dielectric function and the complex index of refraction, respectively, of the semiconductor material, and ε_a and $\widetilde{N}_a$ are the complex dielectric function and the complex index of refraction, respectively, of the surrounding medium, which in this case is air.

The incident linearly polarized light is reflected at the sample surface as elliptically polarized light. The measurement of the actual change in the polarization state is related to the ratio of the reflectance of the two Fresnel reflection components as follows:

$$\frac{r_p}{r_s} = \tan(\psi)\, exp(i\Delta),$$

where ψ and Δ are the measured ellipsometric angles [72]. From these measurements the complex dielectric function is determined for the semiconductor via the following relation for each frequency [73]:

$$\varepsilon_s = \varepsilon_a sin^2\phi + \varepsilon_a sin^2\phi\, tan^2\phi \left(\frac{1 - \tan\psi\, e^{i\Delta}}{1 + \tan\psi\, e^{i\Delta}}\right)^2$$

where $\varepsilon_a = 1.00059$ [74] in air. From this, the complex index of refraction can be calculated using the relationships defined above.

4.3.2 Ellipsometry on α-PbO

Very little ellipsometry data is available from measurement of α-PbO. A number of research groups have grown very thin β-PbO films on lead as a barrier layer and they used ellipsometry to study the film's index of refraction and thickness [53, 54, 75, 76]. Of these, only one group used spectroscopic ellipsometry to study a comprehensive frequency ranging from 1.4 eV to 5.4 eV [54].

Only one journal article could be found that addressed ellipsometry measurement of α-PbO. In that study, single crystals of α-PbO were grown via hydrothermal synthesis. However, the measurements were performed only at a single wavelength, λ=632.8 nm [49]. No data about the spectral index of refraction of α-PbO is currently available.

4.3.3 Experimental setup

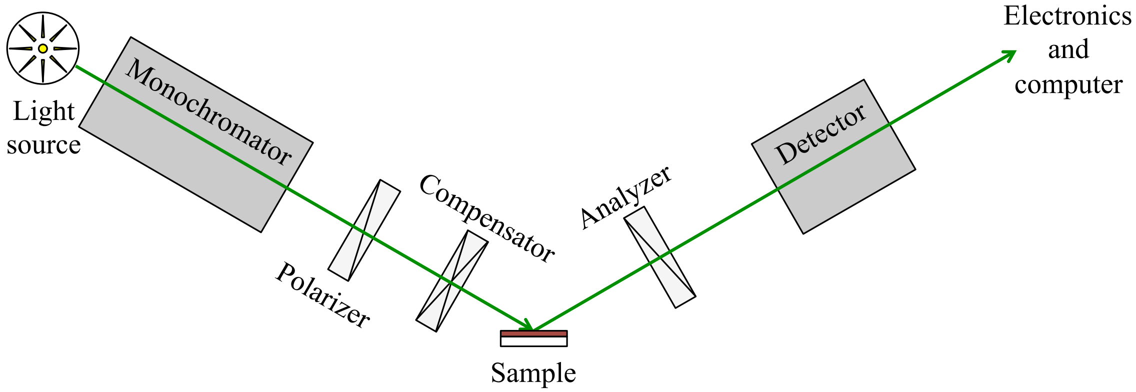

Figure 30: A schematic of a spectroscopic ellipsometer [71, 73].

A light beam passes through a monochromator, which selects the frequency, ω, at each step of the measurement. The light then travels through the polarizer and the compensator, which determines the light's initial polarization state before it interacts with the sample surface. After reflection off of the sample surface, the analyzer measures the polarization state of the light and the detector records the signal [71]. A schematic of the system is displayed in Figure 30.

4.3.4 Data and analysis

As a first step in the collection and analysis of the data, the spectral ellipsometry measurements on α-PbO were performed with the help of Dr. Ruben Lieten at KU Leuven and IMEC in Belgium. Ellipsometry measurements involve data fitting and an analysis to create a model to fit the data, which yields the spectral index of refraction and the spectral extinction coefficient, as displayed in Figure 31 and in Figure 32, respectively.

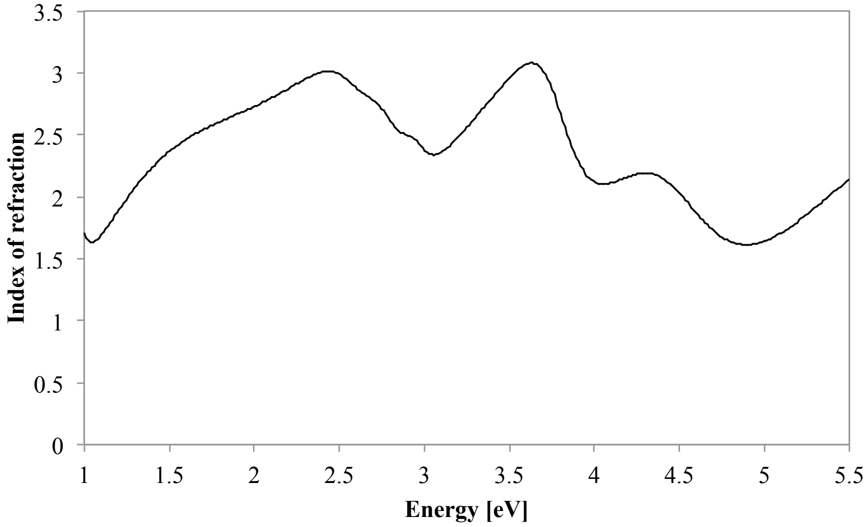

Figure 31: Spectral index of refraction for α-PbO.

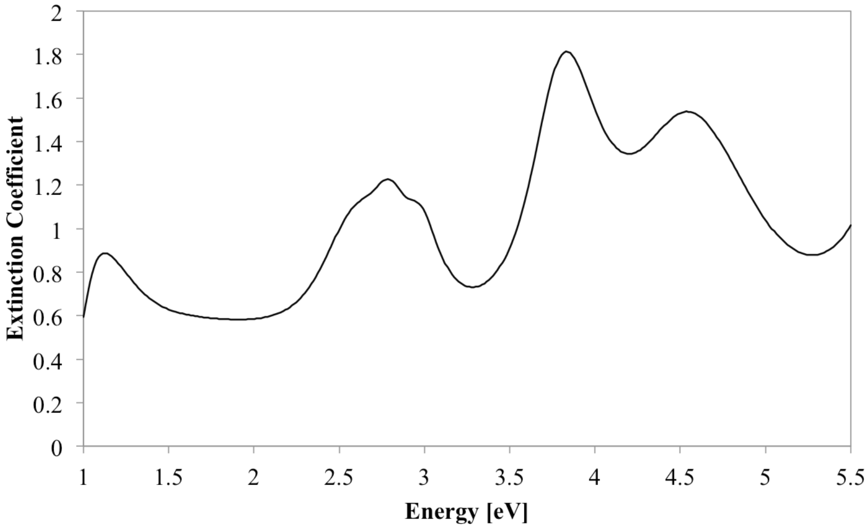

Figure 32: Spectral extinction coefficient for α-PbO.

4.4 Summary

Measurement of the optical properties of semiconductor thin films enables an understanding of how light interacts with the material. Optical absorption spectroscopy is performed by measuring the transmission and reflection of light off of a thin film sample. From these data, the spectral absorption coefficient has been calculated. Fitting the linear regions of the square and square root of the absorption coefficient spectrum yields values for the direct band gap and the indirect band gap, respectively. The direct band gap was measured to be $E_{g.dir}$ = 3.2 eV and the indirect band gap was measured to be $E_{g,ind}$ = 1.9 eV. These values align with the values that were previously reported in the literature for the indirect band gap and the direct band gap of α-PbO. This current study is the first to perform spectral ellipsometry measurements on α-PbO thin films. Data analysis yielded plots of the index of refraction and the extinction coefficient of α-PbO.

Chapter 5: The Electronic and Transport Properties of α-PbO

5.1 Motivation for the Study of Electronic and Transport Properties

In order to judge the suitability of a material as a semiconductor radiation detector, one must have insight into the electronic and transport properties of the material. Any physical measurement that requires the flow of charge carriers into and out of the material will necessitate an understanding of the factors that will effect that measurement.

It is important to probe the charge creation and transport properties of the charge carriers in the material. Spectral photocurrent measurements enable one to both confirm the photoconductive behavior and check on the band gap of the material. The carrier transport properties determine how well the signal from the incident radiation can be recorded. Measurement of the $\mu\tau$-product lends insight into the transport properties of the material.

5.2 The Spectral Photocurrent

5.2.1 Motivation for the spectral photocurrent measurements

Spectral photocurrent measurements are a good way to study the effect that illumination has on the semiconductor material. At the most basic level, it is helpful to determine whether or not the semiconductor exhibits photoconductivity; and, if it does, whether or not the photocurrent response produced is large enough for the material to be considered to be a detector. Spectral photocurrent is also a convenient way to confirm the band gap of the material.

Willoughby Smith first discovered the phenomenon of photoconductivity while working for a telegraph construction company in 1873. He inadvertently exposed selenium to light during a resistivity measurement and noticed a 20% increase in the conductivity of the material. His initial discovery has led to the subsequent discovery of many other photoconductive materials over the years. In the early days of the study of photoconductors, most photosensitive compounds were seen to have cations that did not have a noble-gas configuration in their electronic structure. Pb^{+2} was one such material. Photoconductivity is particularly interesting to the field of detection because of the fact that photoconductors can convert incident photons, such as γ-rays, directly into electrical signals.

In a large band gap semiconductor, the number of free carriers present in a dark environment is very small, leading to a high resistance. Equilibrium exists between the rate of excitation and the rate of recombination of the carriers, which determines the number of carriers present within a material. Upon illumination by light with energy above the band gap, the electrons and the holes are optically excited, increasing the density of the charge carriers and decreasing the resistivity of the material, thereby creating a signal. The structure and the imperfections in a crystal determine whether the optical excitation will induce a large enough photocurrent to be useful in a detection setting.

A number of articles have discussed various types of photocurrent measurements that have been performed on PbO. In some cases, only the β-phase was measured [51], although other reports have indicated that very little or no photocurrent can be measured from the β-phase [47]. Other groups have reported photocurrent spectra from both the α-phase and the β-phase, with the α-phase exhibiting a higher photocurrent than the β-phase [11]. A number of those studies involved a solution electrode [41, 77], while the rest generally deposited contacts such as gold, indium, indium tin oxide, and silver [11, 47, 52]. In general, the photocurrent measurements tended to confirm the expected band gap of the PbO samples [11, 47], and quantum efficiencies of ~1 were reported [41, 52, 77].

The outcome of the photocurrent measurements tends to vary with the type of material being tested. A granular or polycrystalline sample will have a different degree of photoconductivity than a single crystal. Therefore, photocurrent testing is highly desirable for these epitaxial films in order to determine how well this form of α-PbO will respond to illumination.

5.2.2 Experimental setup

Figure 33 presents a schematic of the experimental setup used to measure the spectral photoconductivity in the epitaxial thin films of α-PbO. The light source is a broadband halogen bulb. A chopper creates light pulses at a programmable frequency. The pulsed light enters a monochromator, and various slits and apertures shape the beam into a rectangular spot. A bandpass filter is used to remove second harmonics from the measurement. A concave mirror focuses the beam and creates a rectangular image of the aperture on the sample. The sample has two side-by-side contacts. A bias voltage is applied to the first contact by a Hewlett-Packard 4140B pA meter/voltage source, which will be discussed further in Section 5.4.3. The photocurrent passes out of the second contact as a very small current signal and enters into a current preamplifier. The preamplifier is the Stanford Research Systems Model SR570 Low-noise Current Preamplifier. The preamplifier passes the signal to the Stanford Research Systems Model SR850 DSP Lock-in Amplifier. The lock-in amplifier inputs data from the chopper in order to determine the signal from the dark noise. This also enables the measurement of the phase offset between the measurement and the signal.

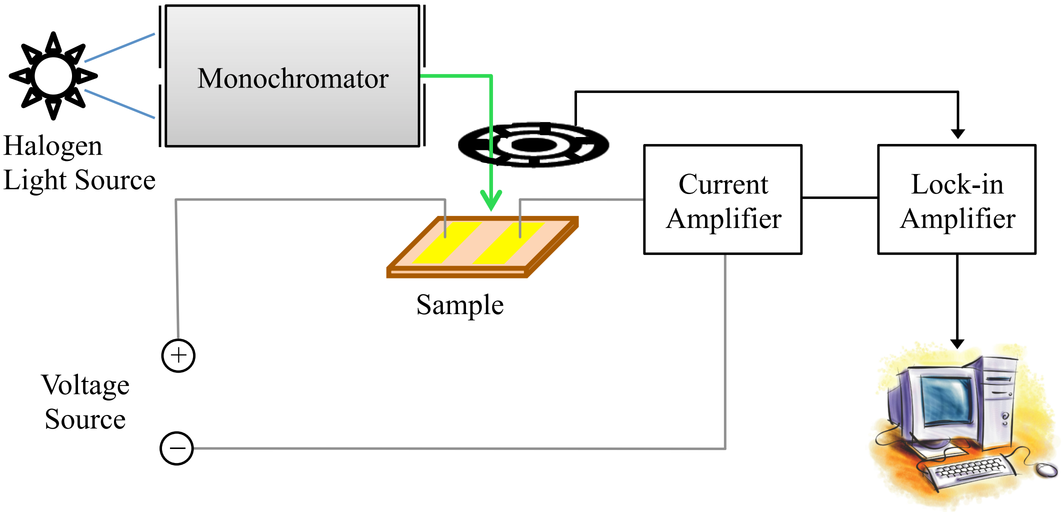

Figure 33: A schematic of the spectral photocurrent measurement system.

The phase data is used to determine when the measurement contains a signal versus when the measurement is only recording noise. The phase of noise is random. Therefore, the output of the phase measurement will be random when the measurement is all noise. An example of this is displayed in Figure 34.

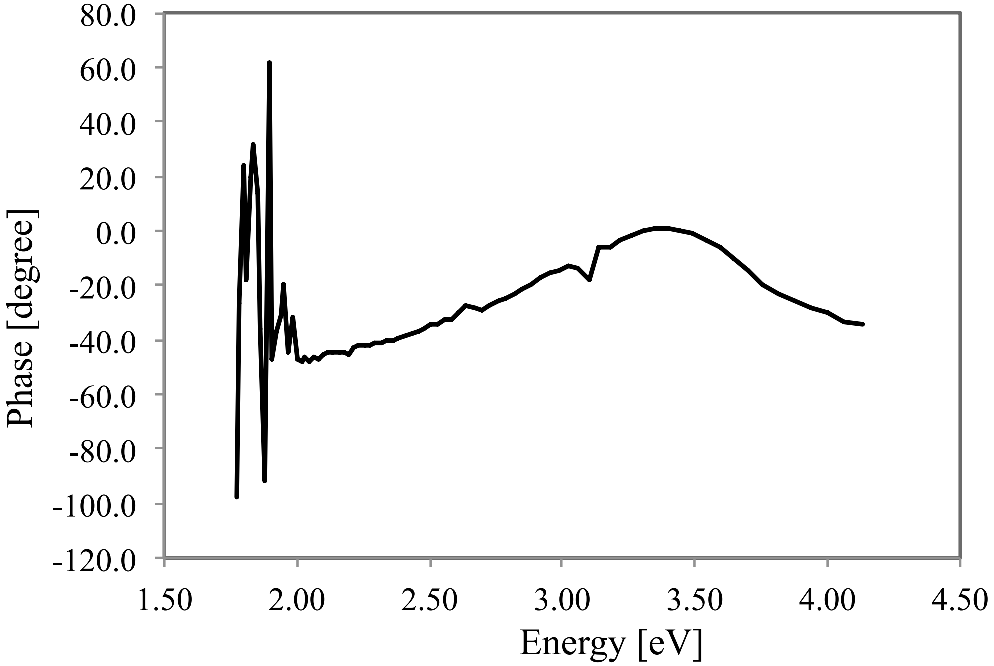

Figure 34: The phase response during a spectral photocurrent measurement. In this case, the phase is random and varies between 180 and -180 until ~ 2 eV, at which point the signal overcomes the noise in the system and the phase is no longer random.

The sample consists of a α-PbO film with a thickness of ~ 600 nm. The contacts were made by e-beam deposition of 15 nm of aluminum and 200 nm of gold. The wires are attached using conductive epoxy. The sample is shown in Figure 35.

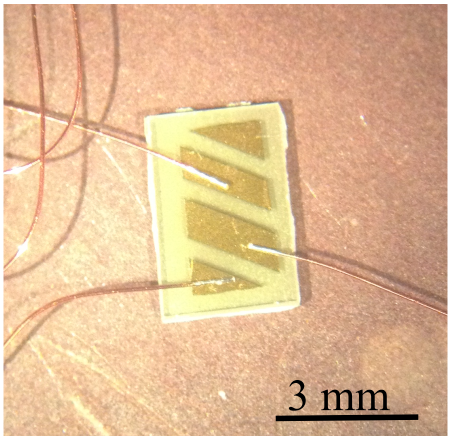

Figure 35: A contacted sample of α-PbO. The sample is being prepared for wire bonding.

The spectral responsivity data of a silicon diode (Si-diode) used for the calibration is loaded into the LabVIEW software program. This diode is used to calibrate the system based on the known responsivity of the Si-diode and the actual, real-time output from the light source. After calibration, the sample is inserted into the light beam and the measurement process can proceed.

5.2.3 Data and analysis

A photocurrent spectrum is measured in the range of 1.6 eV to 4.13 eV, as shown on the plot in Figure 36. This converts to a wavelength range of 300 nm to 775 nm. The onset of the photocurrent occurs at ~ 1.9 eV. As would be expected, this corresponds well to the indirect band gap. A bandpass filter is inserted into the light path at 3.1 eV or 400 nm in order to remove the effects of second harmonics within the system. The sharp dip in the photocurrent at 3.1 eV, seen in Figure 36, is caused by the introduction of the filter. At 1.55 eV or 800 nm, the second harmonics were observed; therefore, no data was taken above 775 nm. This is not an issue because the signal from photocurrent in α-PbO is negligible at wavelengths below the indirect band gap at ~ 1.9 eV. The phase of this photocurrent measurement is presented in Figure 37.

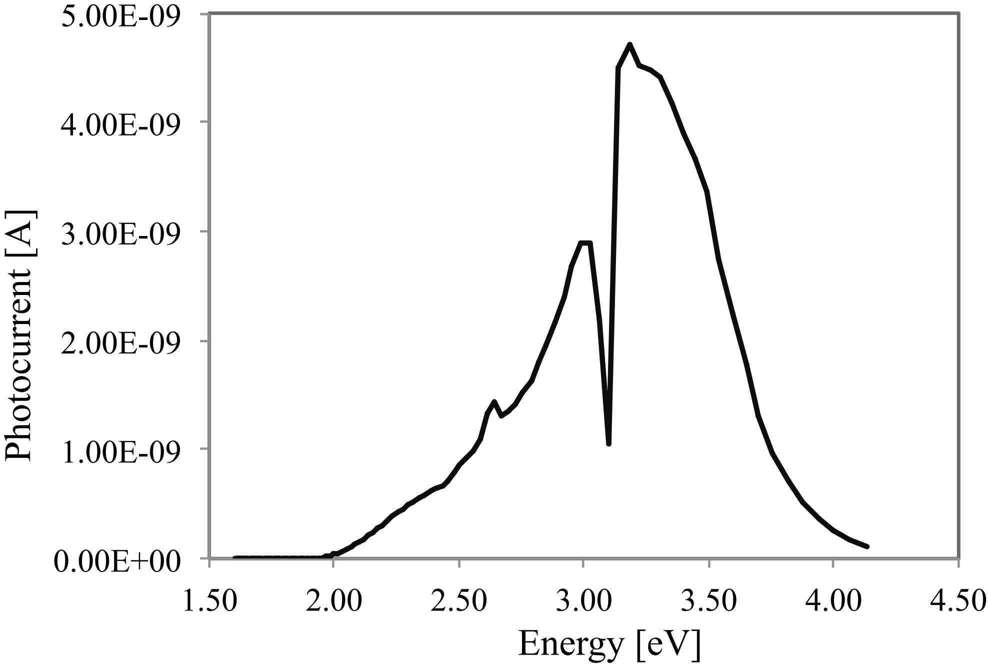

Figure 36: Spectral photocurrent of α-PbO over an energy range of 1.5 eV to 4.5 eV. The onset of the photocurrent occurs around 2 eV, corresponding to the indirect band gap of α-PbO, as expected. During this measurement, the bias voltage across the sample was 60 volts.

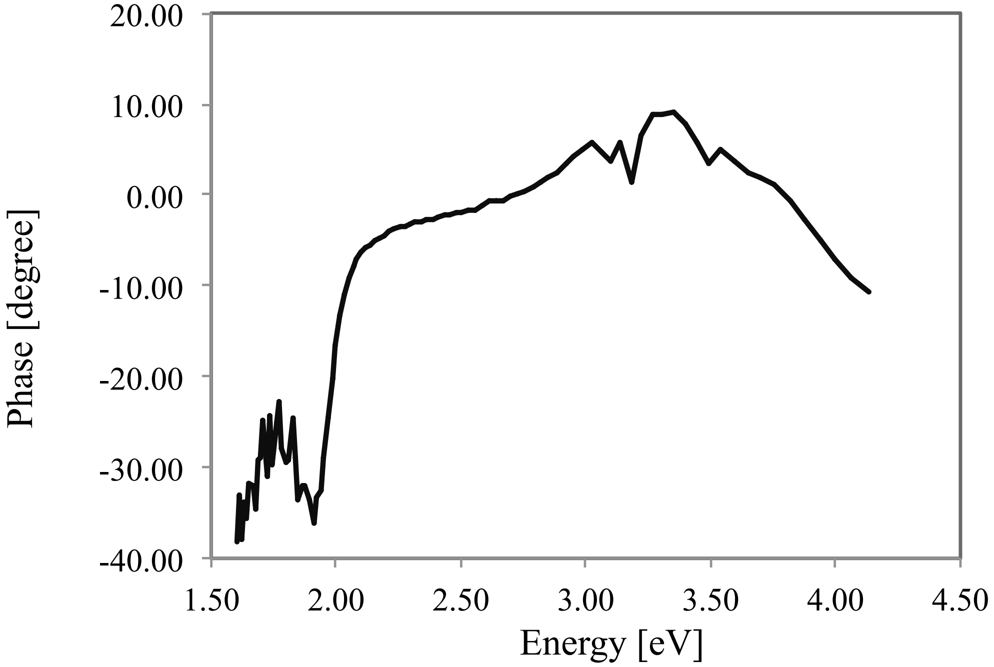

Figure 37: The phase measurement of the spectral photocurrent shown in Figure 36. Although the phase does not appear to become truly random, it increases in noise level when the energy is below ~1.9 eV. This corresponds to the indirect band gap. The noisy segment corresponds to a region of the measurement where the signal is very low, ~ 5 x 10^{-13} A.

The maximum photocurrent has a value of 4.7 nA and it occurs at an energy of 3.18 eV. This correlates very well with the energy of the direct band gap, $E_{g,dir}$ = 3.2 eV, that was calculated and presented in Section 4.2.6. When the photocurrent across the sample is exposed to below band gap light, its amplitude is on the order of 5 x 10^{-13} A. The photocurrent in the sample increases by almost a factor of 10^4 when it is exposed to light near or above the direct band gap, as seen in the logarithmic scale plot in Figure 38.

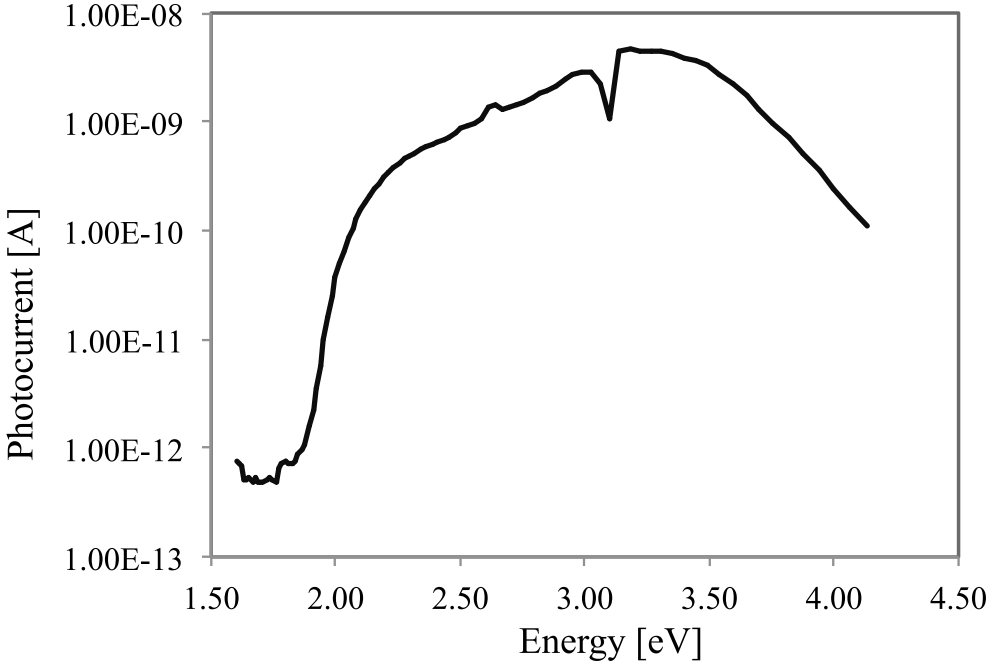

Figure 38: Spectral photocurrent displayed on a log scale to indicate the increase in the photocurrent due to light with energy above the band gap vs. the photocurrent due to light with energy below the indirect band gap.

5.3 The μτ-Product

5.3.1 Importance of the μτ-product

As mentioned in Chapter 2, the μτ-product is a common metric used to evaluate the performance of room temperature detector materials. It is a convenient method to quantify the degree of charge loss due to the charge trapping at the defects. The value consists of the product of the lifetime and the mobility of the charge carriers. The μτ-product is commonly cited in radiation detector work because when it is multiplied by an applied electric field the result is the trapping length. This provides an indication of the maximum size a detector can be and still be able to fully collect all the charge carriers created by an incident photon. This limitation on the size of the detector will limit the range of γ-ray photon energies that the detector is able to absorb before they escape the detector volume. Typically, the μτ values for room temperature detector materials are in the range of 10^{-3}-10^{-6} cm^2/V, and the values for the electrons are generally larger than the values for the holes by an order of a magnitude or more. Several studies have quoted figures for a μτ-product of α-PbO. Two of these studies applied the relation:

$$\mu\tau = \Delta I L^2 / eFV,$$

where ΔI is the photocurrent, L is the sample thickness, e is the charge of an electron, F is the absorbed photon flux, and V is the applied voltage bias. The photocurrent, ΔI, was taken to be the peak photocurrent of the spectral photocurrent measurements similar to those discussed in Section 5.3. When applied to a 54 micron thick polycrystalline film of α-PbO, the above relation yielded $\mu\tau = 4 \times 10^{-7}$ cm^2/V, with a value two orders of magnitude smaller for β-PbO films [11]. When the relation was applied to the case of a 3 mm x 3 mm x 0.1 mm single crystal of α-PbO, a value of $\mu\tau = 10$ cm^2/V was reported [47]. This raises some skepticism because this would imply a trapping length that is 10-times better than the trapping length of HPGe.

Another research group used the equation:

$$\mu\tau = \frac{B^2}{V_s},$$

where B is the barrier width of the sample and V_s is the voltage required to saturate it. This equation was used to study bulk crystals of α-PbO, with the result that $\mu\tau = 2 \times 10^{-9}$ cm^2/V [78]. Another study grew reactively evaporated, polycrystalline, multiphase films that exhibited porosity and rough surfaces. The study used light with energy slightly higher than the indirect band gap and claimed $\mu\tau = 2 \times 10^{-7}$ cm^2/V, but it did not specify how this value was obtained [52].

One fairly common way to measure the $\mu\tau$-product involves a measurement of the photocurrent of the sample with respect to the voltage bias. This photocurrent-voltage (PC-V) data is then fitted to either the Hecht equation or Many's equation [79-82]. After fitting with these equations, the $\mu\tau$-product can be determined. A number of studies have performed PC-V measurements on various α-PbO formats (thin films, bulk crystals, etc.) [11, 52]. However, none of those studies appears to have applied either the Hecht equation or Many's equation. Indeed, the research performed by Schottmiller [11] concluded that, at high voltages, the photocurrent and the dark current become equal. This does not align with data we have gathered on α-PbO, as reported in the rest of this chapter.

5.3.2 Many's equation

In 1964, Many conducted research to understand how large bias voltages, and therefore large applied electric fields, affect charge carrier transport in materials with wide band gaps [83]. He reported that neutral, or ohmic, contacts are not commonly found for insulating materials. Electrodes that begin as neutral, end up losing neutrality in large electric fields due to field emission from the metal electrodes. To eliminate the contact effects, he measured the wide band gap semiconductor CdS using metal electrodes that were capacitively coupled to the sample. By illuminating the sample to create charge carriers, he was able to pulse a voltage across the contacts and measure the photocurrent soon after the onset of the pulse. This effectively acted like blocking electrodes, which eliminated the effects of the aforementioned contacts. In this way, he was able to study charge carrier transport properties without having to worry about the contact effects. His measurement of PC-V characteristics enabled him to isolate the bulk and surface effects and determine the $\mu\tau$-products of the charge carriers.

Using the sample format mentioned above, and light that is absorbed by the sample, measurement of the PC-V characteristic yielded a plot such as the one shown in Figure 39. The photocurrent arises due to the injection of either electrons or holes, depending upon the polarity of the applied voltage. As seen in the figure, the photocurrent is roughly linear to begin with. However, as the applied voltage increases, the photocurrent saturates because the carriers are removed from the sample before they are trapped or before they recombine.

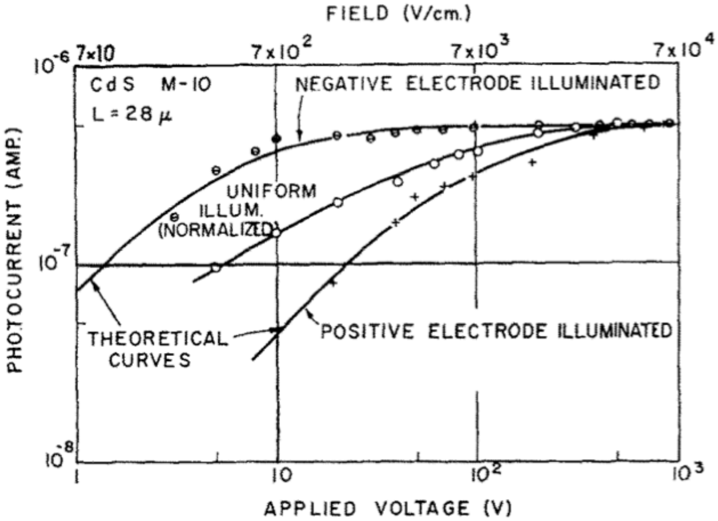

Figure 39: A PC-V characteristic measured by Many on a CdS sample [83]. The sample had capacitively coupled blocking contacts with one transparent contact to allow for illumination.

In order to gain a better physical understanding of the sample parameters it is necessary to derive an equation for the PC-V characteristic. It is assumed that this process includes the following components: two blocking contacts, steady state conditions, uniform carrier excitation within the material, a wafer with sandwich style electrodes, a constant electric field that is perpendicular to the plane of the sample, a charge carrier lifetime that is independent of the position within the sample, and no space charge. In this situation, and neglecting diffusion currents, the continuity equation for electrons is as follows:

$$\mathcal{L} - \frac{n}{\tau_n} - \mu_n \mathcal{E} \frac{dn}{dz} = 0\,.$$

where $\mathcal{L}$ is the volume excitation rate, n is the density of electrons, μ_n is the mobility of the electrons, and τ_n is the lifetime of the electrons. Due to the blocking nature of the contacts, the carriers are swept away by the electric field without being replaced. A boundary condition for this situation is $n(0) = 0$. This enables us to solve the above continuity equation, yielding:

$$n(z) = \mathcal{L}\tau_n[1 - exp\{-z/\mu_n \mathcal{E}\tau_n\}].$$

Using this, we can now solve for the electron current density:

$$j_n = \left(\frac{q\mu_n\mathcal{E}}{L}\right)\int_0^L n\,dz,$$

which leads to:

$$j_n = q\mathcal{L}\mu_n\mathcal{E}\tau_n * \left[1 - \left(\frac{\mu_n\mathcal{E}\tau_n}{L}\right)\left(1 - exp\left\{-\frac{L}{\mu_n\mathcal{E}\tau_n}\right\}\right)\right].$$

A similar mathematical approach leads to an analogous equation for holes:

$$j_p = q\mathcal{L}\mu_p\mathcal{E}\tau_p * \left[1 - \left(\frac{\mu_p\mathcal{E}\tau_p}{L}\right)\left(1 - exp\left\{-\frac{L}{\mu_p\mathcal{E}\tau_p}\right\}\right)\right].$$

These two equations for current density can be added together to obtain the total current density for the sample. An analysis of the form of the equations shows that if the term $\mu_{n,p}\mathcal{E}\tau_{n,p}$ is very large compared to L, the factor with the exponential term goes to 1, and the term after the

* can be neglected. Therefore, the current will display linear dependence on the applied voltage for the low fields, but it will saturate when $\mu_{n,p}\mathcal{E}\tau_{n,p}$ is large. This explains the shape of the curves in Figure 39. It should also be noted that, for a case in which only a single carrier is present, the transition from the linear region to the saturated region becomes quite sharp. However, if both carriers are present and their μτ-products are not equal, the transition between the linear range and the saturation range will be more gradual. This appears to be the case for the curves in Figure 39. For a sample that meets the assumptions presented in this discussion, the equation can now be fitted to the data and the μτ-products can be extracted.

If the sample absorbs light very strongly near the surface instead of uniformly throughout the material, the analysis must include the surface effects in order to have an accurate fit to the data. In this case, carrier excitation will occur only at the illuminated surface at a rate of $\mathcal{L}_s$ per unit area. With the exception of the sample illumination, all the other assumptions remain the same. The electron continuity equation, for z greater than 0, can then be written as:

$$-\frac{n}{\tau_{tn}} - \mu_n \mathcal{E}\frac{dn}{dz} = 0\,,$$

where τ_{tn} is the lifetime for the electron trapping. Moreover, τ_{tn} quantifies the capture of the electrons in traps in the bulk of the material. It can be assumed to be constant because of the low number of carriers in the bulk material for these conditions. The boundary condition for this equation arises from the excitation rate, because it is equivalent to the sum of the charges leaving the surface, $\mu_n\mathcal{E}n(0)$ and the rate of the surface recombination. If the surface recombination is proportional to the surface electron density, we can write:

$$n(0) = \frac{\mathcal{L}_s}{\mu_n\mathcal{E} + s_n}\,,$$

where s_n is the surface recombination velocity. Using this to solve the continuity equation yields:

$$n(z) = \left[\frac{\mathcal{L}_s}{\mu_n\mathcal{E} + s_n}\right] exp\left\{\frac{-z}{\mu_n\mathcal{E}\tau_n}\right\},$$

which, in turn, allows us to solve for the current density of electrons:

$$j_n = \left(\frac{q\mu_n\mathcal{E}}{L}\right)\int_0^L n\, dx$$

$$j_n = \frac{q\mathcal{L}_s s_n}{1 + \frac{s_n}{\mu_n\mathcal{E}}}\left(\frac{\mu_n\mathcal{E}\tau_{tn}}{L}\right)\left(1 - exp\left\{\frac{-L}{\mu_n\mathcal{E}\tau_{tn}}\right\}\right).$$

According to similar calculations for the holes, the current density is:

$$j_p = \frac{q\mathcal{L}_s s_p}{1 + \frac{s_p}{\mu_p\mathcal{E}}}\left(\frac{\mu_p\mathcal{E}\tau_{tp}}{L}\right)\left(1 - exp\left\{\frac{-L}{\mu_p\mathcal{E}\tau_{tp}}\right\}\right).$$

The experimental setup for the measurement of the PC-V characteristic of α-PbO thin films differs from the setup described above in a number of ways. The contacts on the sample are not blocking, although they are probably not ohmic either. Further analysis of the dark current-voltage (IV) characteristic is explored in Section 5.4.4. Because the contacts on the α-PbO sample are deposited onto the surface instead of capacitively coupled, some deviation from ideality in the fitting results will occur.

While Many was conducting research on this process, he studied the effect of non-blocking contacts on the outcome of this method of analysis. He replaced a blocking contact with a silver paste contact and proceeded with measuring the PC-V characteristic. This silver contact will have a depletion layer, which blocks the carrier injection for fields that are less than 5000 V/cm. As previously seen, this will lead to a photocurrent that displays initial linear dependence that reaches the saturation region. However, as the electric field within the sample increases in the saturation region, the photocurrent ceases saturation behavior and increases at a rate greater than the rate seen even in the linear region due to the field emission from the metal electrode. An example of this is displayed in Figure 40. This effect will limit the amount of voltage that can be applied to the α-PbO sample.

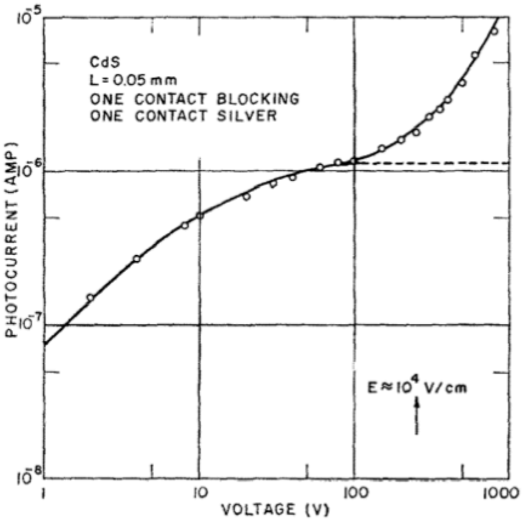

Figure 40: The effect of a non-blocking contact on the PC-V characteristic [83].

Another deviation from the assumptions listed above arises because the sample structure consists of two side-by-side contacts instead of a planar sandwich structure. This is due to the dependence of the growth of α-PbO on the substrate. A bottom electrode is not currently possible. However, two contact bars on the surface with a large separation, with respect to the sample thickness, will have an electric field that can be roughly approximated as a constant, unidirectional field. Still, this will likely be a source of error.

5.3.3 Experimental setup for the PC-V measurement

Before measuring the PC-V characteristics, it is helpful to first look at the dark IV characteristic. This should provide some evidence as to the nature of the electrical contacts on the α-PbO material. A Hewlett-Packard 4140B pA Meter/DC voltage source measures the current produced as it applies the voltage over a user-defined range. The 4140B can apply a voltage range of ±100 volts. It can also measure current in the range of $\pm0.001\text{x}10^{-12}$ A to $\pm1.999\text{x}10^{-2}$ A. The dark IV characteristic measurements are automatically synchronized between the pA meter and the voltage source [84]. The circuit used for this measurement is shown in Figure 41. A LabVIEW software program accepts the user's input of the voltage range and the maximum current allowed, and the output data.

The samples are thin films of α-PbO. The contacts are deposited by e-beam as two side-by-side bar contacts made of 20 nm of aluminum and 200 nm of gold. Data from the IV characteristic measurements are shown in in Figure 42 in Section 5.4.4. The same sample is used for both the IV measurement and the PC-V measurement.

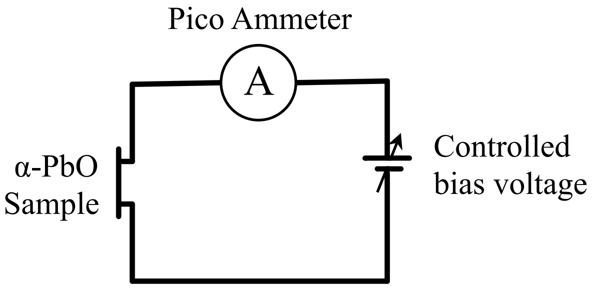

Figure 41: The measurement circuit for the IV characteristics.

The PC-V characteristic measurement is identical in setup to the dark IV characteristic measurement. The addition of a controlled bandwidth light source is the only difference between these two approaches. In the PC-V characteristic measurement, the incident light comes from a tungsten halogen lamp through a monochromator and a number of slits and irises, and it is focused onto the sample by a concave mirror. The light source setup is the same setup that was used for the spectral photocurrent measurement described in Section 5.3.2.

5.3.4 Data and analysis

Measurement of the dark IV characteristic of α-PbO yielded data that is shown in the plot in Figure 42. The measurement was taken using a voltage ranging from -8 volts to 8 volts. The resultant dark current reaches a maximum range of 2 nA to 3 nA. At -8 volts, there is a small onset that is likely caused by capacitive charging of the sample. The IV curve looks fairly linear in the range near zero volts. This might imply ohmic-type behavior of the contacts. Another option is that the sample contacts may not be ohmic at all; instead, a surface leakage current might be present that scales roughly linearly with the applied voltage.

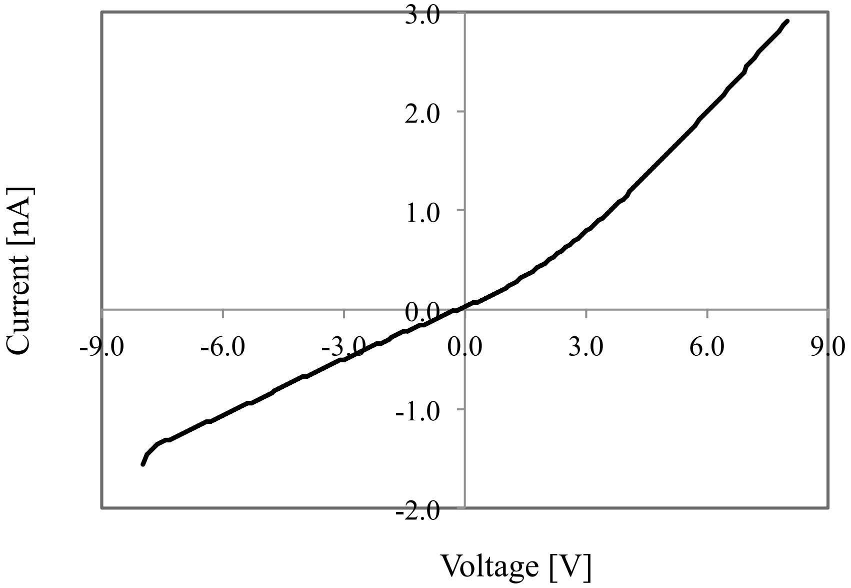

Figure 42: Dark IV characteristics of an α-PbO.

Applying Ohm's law to the data shown in Figure 42 enables the calculation of the approximate resistance of the material during the IV measurement. The result is an average resistance in the $4 \times 10^9\ \Omega$ range. Calculating the resistivity for the α-PbO thin film material yields $5.7 \times 10^{13}\ \Omega$ cm. Based on reports in the literature, this is a fairly high value; however, this value also includes any contact resistance in the measurement.

Adding a light source to the dark IV characteristic measurement yields the PC-V characteristic. The effect that the energy of the light source has on the photocurrent is explored in Figure 43. The PC-V characteristics were measured in the dark (IV), with a below band gap light of 1.55 eV, with an above indirect band gap light of 2.25 eV, and with a near direct band gap light of 3.02 eV. Clearly, the strongest absorption occurs with the use of the highest energy light.

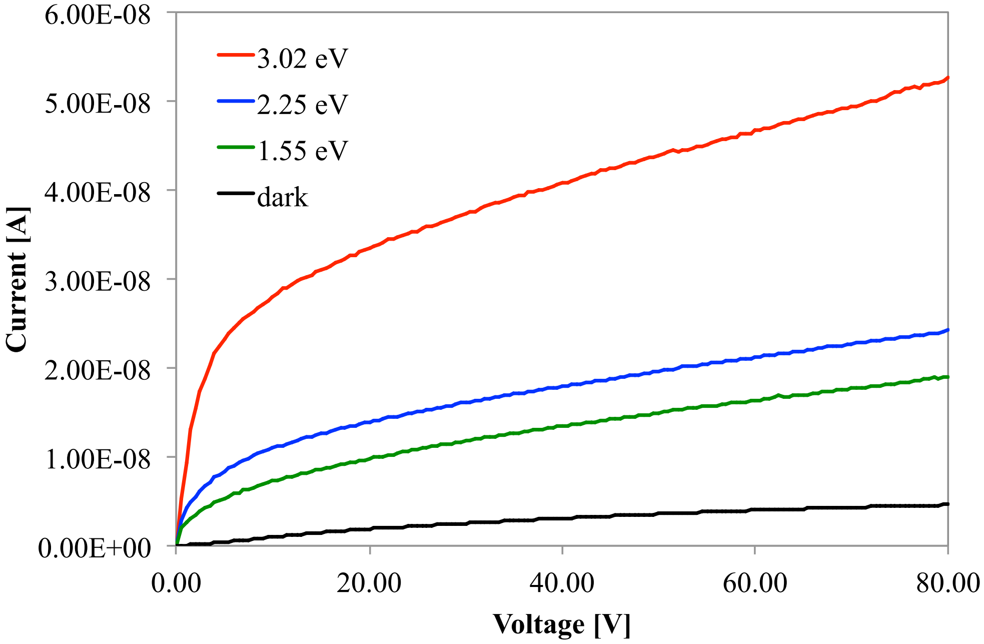

Figure 43: The PC-V characteristics for illumination with varying energy light sources.

The onset displays a linear dependence upon applied voltage, as expected based on the discussion presented in Section 5.4.2. There appears to be a sharp transition between the linear region and the saturation region, which implies a single carrier function. However, initial attempts at fitting Many's equation to the data have been unsuccessful. Therefore, further analysis of the experiment is warranted. We suspect non-blocking contacts are causing the deviation from the fitting equation. To check this, the PC-V measurement under 3.02 eV illumination is plotted and reformatted so that it has similar axes to the plot of the PC-V measurement performed by Many, which used a non-blocking contact, as displayed in Figure 40.

A comparison of these two plots is shown in Figure 44. A definite similarity can be seen in the shapes of the two curves. The linear onset in each plot transitions to a saturation region. At higher applied voltages, both of the plots display a rapid increase in photocurrent. The plot on the left shows more data; however, the plot of the PC-V of α-PbO shows the beginning of the upward trend. Indeed, for this sample, further testing using higher voltages led to instability in the photocurrent and potentially to the initiation of breakdown due to excessive current flow.

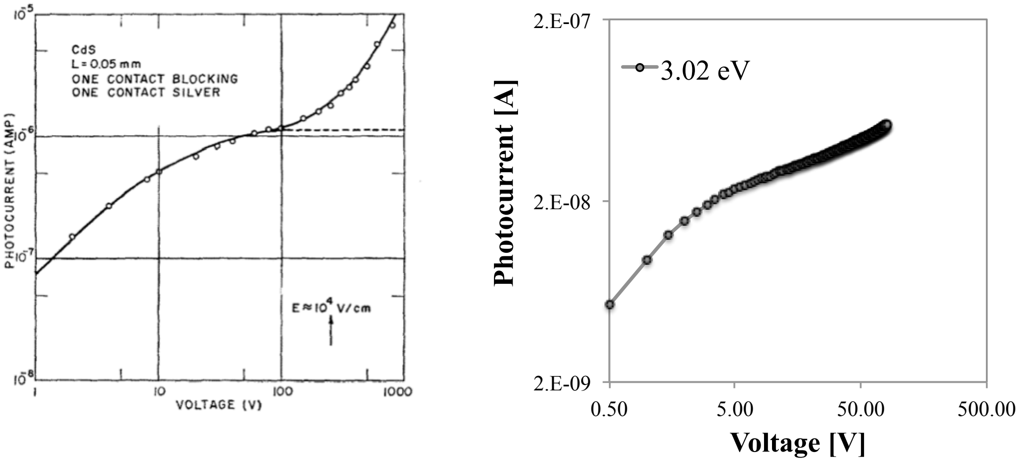

Figure 44: A comparison between the data collected by Many from a sample with a non-blocking contact [83] and an α-PbO thin film.

At low fields, the photocurrent exhibits linear onset. With increasing voltage, the data demonstrates saturation behavior. According to Many [83], these sections of the PC-V plot are very similar to data taken from a sample with two blocking contacts. The photocurrent behavior deviates from the expected behavior only at higher values of applied voltage. Therefore, data below the photocurrent runaway can be fit with Many's equation in order to determine the μτ-product.

A plot showing the fit between the experimentally derived data and Many's equation is shown in Figure 45. For the majority carrier, fitting Many's equation to the experimental data yielded a μτ-product of $\mu\tau = 6.8 \times 10^{-4}$ cm^2/V. This value is much larger than most of the previously reported μτ measurements for α-PbO. However, this value is low compared to the values currently achieved in materials such as CZT, as mentioned in Chapter 2.

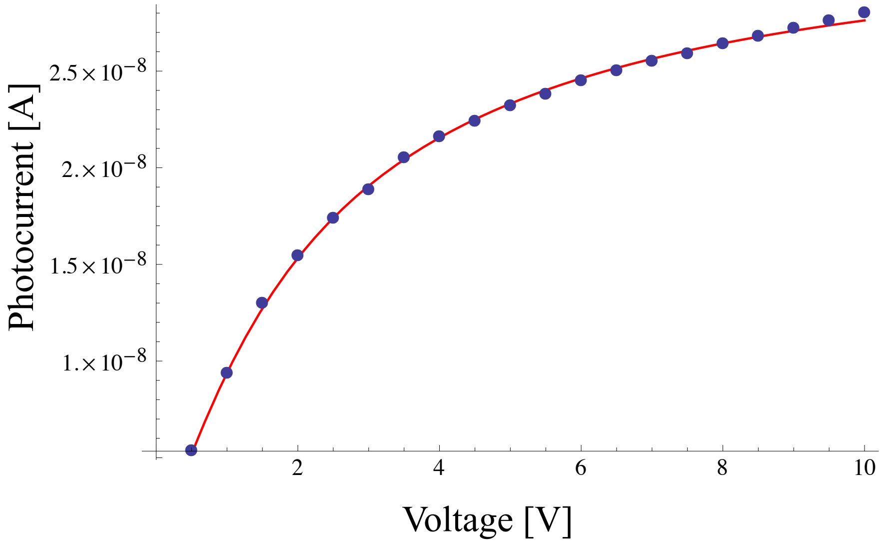

Figure 45: The PC-V data set showing the fit between the experimentally measured data (blue dots) and Many's equation (red line).

5.4 Summary

The study of the electronic and transport properties of a semiconductor is crucial to increasing the understanding of how it will function as a detector material. Only a few α-PbO studies have addressed these topics. To better understand the electronic and transport properties of α-PbO, this chapter focused on the spectral photocurrent and the $\mu\tau$-product of the material.

Spectral photocurrent measurements are a good way to study the effect of illumination on the semiconductor material. At the most basic level, it is helpful to determine whether or not the semiconductor exhibits photoconductivity; and, if it does, whether or not the photocurrent response produced is large enough for the material to be considered to be useful as a detector. Spectral photocurrent is also a convenient way to confirm the band gap of the material. In this study, the thin films of α-PbO did exhibit photoconductivity upon illumination. The onset of measureable photocurrent coincided with the indirect band gap of the material. The peak of the photocurrent occurred near the direct band gap of the material. Illumination of α-PbO by light with energy at or greater than the direct band gap yielded photocurrents of ~ 5 nA. This value was approximately four orders of magnitude larger than the photocurrent from the sample when illuminated by below band gap light.

Measurement of the $\mu\tau$-products yields a convenient metric that is used to compare the function of the detector materials. This value holds interest because, when it is multiplied by the applied electric field, it yields the distance a charge carrier can travel before being trapped or before being recombined. Fitting Many's equation to experimental PC-V data yielded a $\mu\tau$ of α-PbO on the order of 10^{-4} cm^2/V. This value is lower than the values that are commonly seen for other high quality room temperature detector materials. However, this finding is much larger than most other results found in the literature. It can be expected that the $\mu\tau$-product of α-PbO will increase as more research is conducted on the best growth methods for this material.

Chapter 6: Radiation Detection

6.1 Background

6.1.1 Why detect alpha particles?

The detection of γ-radiation is the end product of room temperature semiconductor radiation detection for protection against nuclear threats in ports. However, the material growth process developed for this research is in a thin film format. Although PbO is a high-Z semiconductor, thin films do not have enough power to stop and absorb a γ-ray. Therefore, γ-ray detection testing will be delayed until it is possible to re-establish the growth of suitable sized single crystals.

We looked at alpha particle radiation detection in order to test the initial performance of α-PbO as a nuclear radiation device. We chose to investigate alpha particles because they are relatively massive and have high energy; they also produce small penetration depth. A review of previous research on alpha particle detection by α-PbO identified very few studies examining this topic. One report mentioned the use of an unspecified phase of lead oxide to detect alpha particles via a microchannel plate. In that study, lead oxide was used as a coating on the inside of the channels to absorb the alpha particles, triggering a release of secondary electrons [85]. However, no further information about this application could be found.

6.1.1 An overview of radiation and decay

Radiation occurs spontaneously in unstable heavy elements. This results in a nuclear transformation in which new elements and a variety of decay products are formed. The general process is:

$$Parent \rightarrow Daughter + decay\ 1 + decay\ 2 + \cdots$$

where the parent is the original, unstable nuclide. The products of the radioactive decay include a more stable element, called the daughter, and a number of lighter decay products or particles. Each decay process is often accompanied by γ-radiation.

The results of the various decay processes include: alpha decay, β- decay, β+ decay, γ-emission, isomeric transitions, electron capture, spontaneous fission, proton decay, among a few other decay processes [86]. The specifics of the majority of these decay processes are outside the scope of this dissertation. However, a closer look at alpha decay is warranted to further understand the physics of the detection process discussed in this chapter.

6.1.2 A closer look at alpha particles

An alpha particle consists of two protons and two neutrons, identical to a helium nucleus. In the realm of radiation detection, an alpha particle is considered to be a massive particle, especially compared to other common types of radiation. In addition, it has two protons but no electrons, so the particle is positively charged. Because of its large mass and its charged state, it interacts promptly with any material, causing rapid ionization within a small range.

A thin film (0.127 mm to 0.254 mm) of americium (^{241}Am) with an activity of 100 nCi is the source of the alpha particles used in this work. Americium is commonly used in smoke detectors, where an alarm goes off if smoke blocks the alpha particles from ^{241}Am from reaching a detector. It has a half-life of 430 years. ^{241}Am undergoes radioactive decay via the creation of alpha particles with energy of 5.486 MeV (~85%), shown schematically in Figure 46.

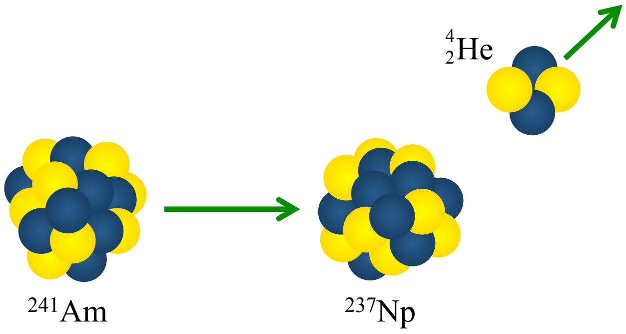

Figure 46: Alpha particle decay schematic.

The daughter nuclide is neptunium (^{237}Np). The decay process is accompanied by γ-radiation with an energy of 59.55 keV (~78%) [87]. A more complete decay scheme, in which ^{241}Am appears, is displayed in Figure 47. A thin film alpha source is preferred because it will produce monoenergetic alpha particles. A thick source produces alpha particles from various positions within the source layer. The particles that are situated toward the surface have the full amount of energy;, however, the particles that originate from deeper within the layer will lose energy to the americium layer as they escape.

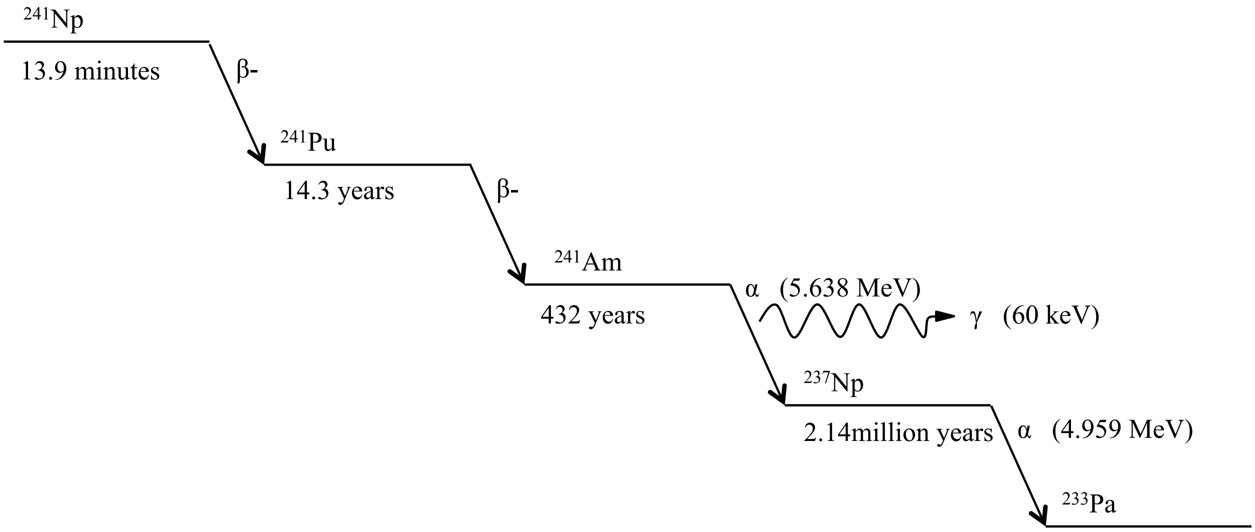

Figure 47: The decay scheme in which ^{241}Am appears.

The alpha flux incident onto the detector sample is estimated in the following manner. Assuming that the source emits in all directions, and assuming that the source area can be estimated to be small in comparison to the distance between the source and sample, the fractional solid angle can be simplified to:

$$FSA = \frac{A_{sample}}{A_{sphere}},$$

where the sphere is centered on the source and the radius of the sphere is the separation distance between the source and the detector, as shown in the schematic in Figure 48. For a detector with an active size of 5 mm x 5 mm the A_{sample} will be 25 mm^2. For a source-detector distance of 20 mm, the A_{spere} = 5026.5 mm^2.

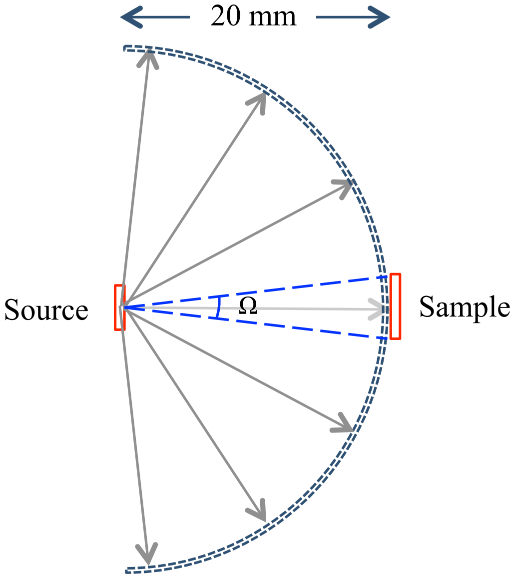

Figure 48: A schematic of the fractional solid angle between the source and the detector.

$$\Omega = \frac{A_{sample}}{A_{sphere}} \cong 0.005$$

This equation estimates the fraction of the sphere that the detector encompasses. The activity of the sample must also be taken into account. As mentioned above, the sample in this work has an activity of 100 nCi, which is equal to 3700 decays/second. When this is multiplied by the fractional solid angle, it is possible to find the number of alpha particles hitting the detector per second. This value is calculated to be 18.4 alphas/second. This will likely be a lower limit because the source does have a finite extent.

As an alpha particle enters the semiconductor material it collides with its surroundings; it changes direction slightly and loses energy, causing the formation of electron-hole pairs. The alpha particle is involved in two types of collisions: inelastic and elastic. During an elastic scattering event, an alpha particle collides with the atom nuclei causing a change in direction, but the energy of the alpha particles is preserved [88]. During an inelastic collision, the alpha particle interacts with the outer electrons of the detector atoms causing ionization and a loss in kinetic energy from the α-particle as the electrons are scattered.

As the alpha particle travels through the detector material, it continuously experiences many of these types of collisions. Every collision decreases the alpha particle energy by a fraction, causing it to slow down. As the α-particle slows to a stop, the rate at which its energy is removed increases and it starts to become less charged as it captures orbital electrons. Close to the end of its range it rapidly loses all of its energy. As shown in Figure 49, this leads to the formation of a Bragg peak in a measurement of energy versus penetration depth. A significant amount of the α-particle energy is lost at the end of the range, making it important to stop the particle within a detector volume [89].

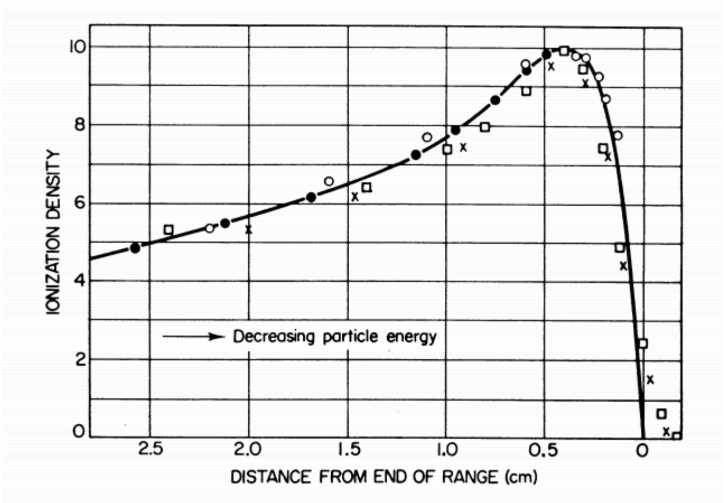

Figure 49: Alpha particle ionization in air. Most of the alpha particle energy is released at the end of its path in a Bragg peak [89].

Because of the importance of stopping the alpha particle within the detector volume, it is crucial to have a better understanding of the stopping power of α-PbO. To model the path range of an alpha particle in α-PbO, we use a program called SRIM© version 2008. This program uses statistical methods to calculate the stopping and the range of ions as they enter a target material. A subprogram, called TRIM, allows the user to define complex target materials. A calculation of the stopping range of alpha particles in α-PbO is displayed in Figure 50. The majority of the alpha particles travel a distance of 16 μm in α-PbO before stopping [90].

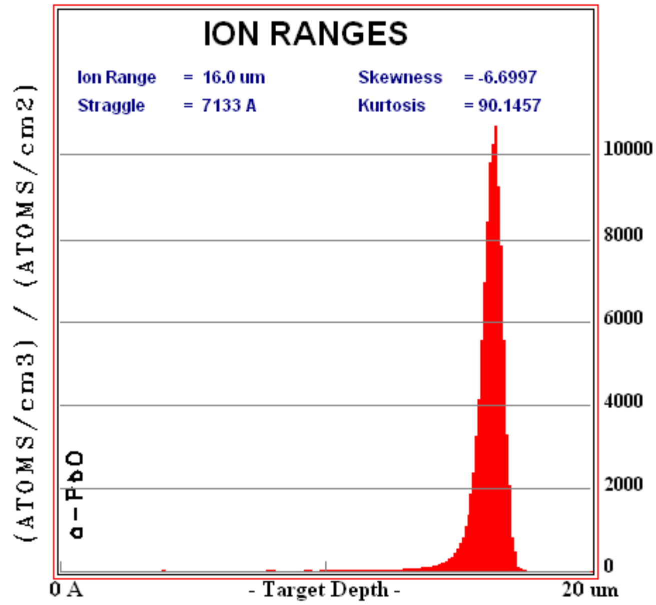

Figure 50: SRIM/TRIM calculation showing the stopping range of the alpha particles in a α-PbO target.

6.1.3 Factors affecting the detection of the alpha particles

Active region: The geometry of an alpha particle detector is determined by the function of the detector. In this case, we do not have a low-intensity source or need to count incident particles, so a large area detector is not necessary. Indeed, a larger detector area can lead to a large capacitance, which has negative effects as discussed below. Additionally, the detector resolution is dependent upon the size of the detector, in which case a smaller detector area is desirable. Furthermore, the detector should be thick enough to stop the alpha particles, as discussed in Section 6.1.2. Increasing the detector depth can decrease the capacitance in the system; however, doing so can also increase the noise.

Capacitance of the detector: As the capacitance of a detector increases, so does the effective electronic noise of the preamplifier. To quantify this, the preamplifier's "slope" is determined by the increase in the electronic noise per unit of increase in the capacitance. In addition, the rise time of the preamplifier will also be affected. To achieve a low noise environment for this application, it is preferable to minimize the detector capacitance geometrically. Additionally, cables and connectors can add to this problem and, thus, they must be managed.

Leakage current: As discussed in Chapter 2, it is desirable for the detector to have as low a leakage current as possible. This leakage current is temperature-dependent and its increase will cause an increase in the electronic noise during a measurement. If the noise is large enough, it may completely overwhelm the signal from the detector.

Detector noise: Noise is introduced into the system by the detector leakage current and the preamplifier. This causes a broadening of the pulse height spectrum obtained by the multi-channel analyzer. Using wide-band gap semiconductors and high quality material lessens the detector noise. The preamplifier noise can be managed by selecting an appropriate time constant. The noise can be quantified using the FWHM of a mono-energetic peak. The total noise in the system is determined by the square root of the sum of the squares of the individual noise sources.

Energy resolution: As discussed in Chapter 2, detector noise and statistical fluctuations will set a lower limit on the achievable energy resolution. Energy resolution will also be affected by imperfect charge collection. Consequently, large bias voltages are used to increase the efficiency of the charge collection. The quality of the source is another important aspect to consider. As discussed briefly in Section 6.1.2, a thick-film source causes the alpha particles to lose energy as they travel through the layer of ^{241}Am. This would lead to incident alphas with a range of energies. Even with perfect charge collection, this would lead to broadening of the alpha energy peak and degradation of the energy resolution [21].

6.2 Experimental Setup

6.2.1 The sample

Preparing the sample for testing the alpha particle response in α-PbO involves growing samples of sufficient thickness to stop an alpha particle. An e-beam deposition system is used to deposit contacts that consist of 15 nm aluminum as a wetting layer and 200 nm of gold. The two side-by-side contacts are separated using a wire shadow mask. Wires are connected to the electrodes using conductive epoxy. Initial test samples that were grown for one hour had a thickness of 2 μm. A five-hour growth duration produced samples that have an estimated thickness of 8 μm. Prior to testing detection of alpha particles on α-PbO, the system will be calibrated by testing detection on a silicon diode. This diode is discussed further in Section 6.3.3.

6.2.2 The vacuum chamber

As seen in Figure 49, the range of alpha particles in air is not very long. This value will change with the energy of the alpha particle, and it follows the relationship [89]:

$$R_{air}[cm] = (0.005 * E_{\alpha}[MeV] + 0.285) * E_{\alpha}^{3/2}[MeV].$$

Application of this equation for decay from ^{241}Am yields an expected alpha particle range of 4.0 cm in air. For this work, it is preferable to have a monoenergetic alpha particle source. Therefore, the alpha detection study will need to be conducted in a vacuum environment in order to avoid loss of alpha particle energy.

The detector is mounted in a vacuum chamber fabricated at Lawrence Berkeley National Laboratory. One of the detector electrode wires is soldered onto the bias voltage input circuit. The other detector electrode is soldered to the vacuum chamber output to the charge sensitive preamplifier. The ^{241}Am source is mounted to a metal tag and suspended over the detector at a set height. A shutter inside the vacuum chamber swings freely on an axis so that the alpha signal can be stopped and started by tilting the chamber without bringing the vacuum to atmospheric pressure. Before starting the measurement, the chamber is roughed out and then pumped down using a turbo pump to a pressure of ~ $3x10^{-5}$ Torr.

6.2.3 The test pulse generator

A test pulse generator is used to check the detection system in order to insure that it is properly setup and functioning. This generator allows the user to send a pulse through the system that looks like the charge pulse deposited by the alpha particle in order to determine whether or not the system is functioning. The test pulse generator used in this work is a Berkeley Nucleonics Corporation Model BH-1 Tail Pulse Generator, a pulse generator specifically designed to simulate radiation signals. The frequency of the tail pulse generator can be controlled to approximate the frequency of the alpha particle incidence. The rise time and the decay time of the pulse are also variable.

The generator has a variable output amplitude that can range from 0 volts to 9.99 volts, along with a 10x attenuator and a 100x attenuator. The pulse amplitude mimics the energy of the alpha particle, with a sharp rise to a peak and a slower decay, and it enables precise determination of the energy spectrum from the multi-channel analyzer. As seen in Figure 7, the pulse enters through a specific input port on the charge sensitive preamplifier [91]. It can also be applied across the detector through the voltage bias filtering circuit, as shown in Figure 51.

6.2.4 The high voltage bias and filter

The voltage bias is applied to the detector through a filtering circuit, as noted in Figure 51. The high voltage input is indicated by HV. The various resistors and capacitors are marked, where their values are known.

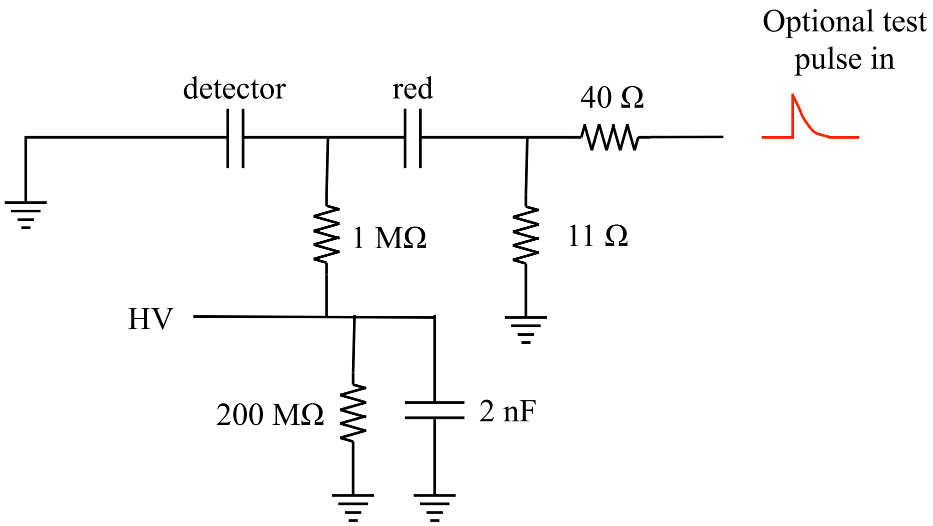

Figure 51: A schematic of the filtered high voltage input.

6.2.5 The charge sensitive preamplifier

After absorption of an alpha particle in a detector, the signal travels to the charge sensitive preamplifier (CSP). This is the preferred type of preamplifier for energy spectroscopy. The CSP is used to read the signal from the detector after an incident alpha is absorbed. The circuit inside the CSP is tailored to the function of the detection system. The CSP integrates the charge in the pulse from the detector output. The expected signal from the detector is very small; therefore, it is important that the CSP contribute as little noise as possible. The CSP will be sensitive to input capacitance from cabling between the detector output and the CSP input, so this should be as short as possible. The effects from this include: microphonic noise, ground loops, and radio frequency pickup. If those effects are present, they will show up as noise for the CSP. The signal enters as a current pulse and it is then integrated into a feedback capacitor. The CSP outputs a voltage with an amplitude, V_0, which can be calculated as follows:

$$V_0 = \frac{Q_D}{C_f},$$

where Q_D is the charge released by the detector and C_f is the capacitance from the feedback capacitor. The calculation of Q_D introduced above is as follows:

$$Q_D = \frac{E_\alpha * e * 10^6}{\varepsilon},$$

where E_α is the energy of the incident alpha particle, 5.486 MeV, e is the charge of an electron, the 10^6 factor converts the alpha energy from MeV into eV, and the ε is the electron-hole pair creation energy. For a silicon detector with $\varepsilon = 4$ eV, $Q_D = 0.2194$ pC. For a detector of α-PbO with $\varepsilon = 6$ to 8 eV, $Q_D = 0.1097$ to 0.1463 pC.

Similar calculations can be performed to determine the sensitivity, or gain, of the preamplifier that is needed for detection, using both the silicon and the α-PbO detectors. Entering the equation for Q_D into the equation for output voltage from the CSP, V_0, and rearranging gives:

$$\frac{V_0}{E_\alpha} = \frac{e * 10^6}{C_f * \varepsilon}.$$

Assuming that the feedback capacitance is approximately 1 pF, the required sensitivity for a silicon diode is 40 mV/MeV. For the α-PbO detector, the sensitivity ranges from 20 mV/Me to 26.7 mV/MeV.

The CSP will produce some noise in the system that will contribute to broadening the alpha energy peak. The noise comes from the input FET, the total capacitance of the input (C_f and the detector capacitance, etc.), the resistance connected to the input, and the leakage current from the detector and the FET. The noise can be evaluated by setting the test pulse to a charge, Q, equal to the energy of the alpha particle. This is injected into the preamplifier, which results in an energy peak in the multichannel analyzer. Measuring the FWHM of this peak gives the noise of the system, since the test pulse in a theoretically perfect system would be a delta function [92].

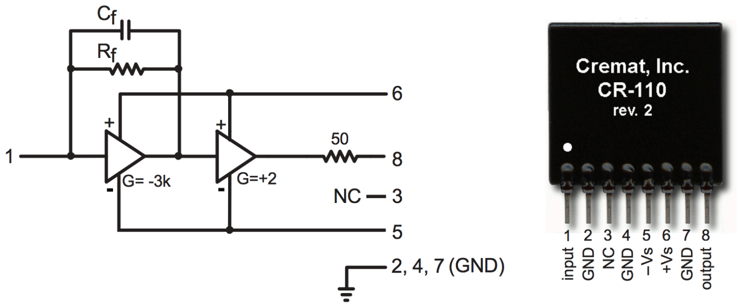

Figure 52: On the left, a simplified equivalent circuit schematic of the CSPs manufactured by Cremat, Inc. C_f and R_f denote the feedback capacitance and resistance, respectively. These values are listed in Table 4. On the right is the packaged CSP with labeled pins. Pin 1 is the input from the detector [93].

A set of four CSP preamplifiers made by Cremat, Inc. were used in this work (Figure 52). These CSPs have the following model numbers: CR-110, CR-111, CR-112, and CR-113. Each of these preamplifier chips has a different gain and energy range. The CR-110 model has the highest gain, at 1400 mV/pC; however, it also has the lowest energy range leading to saturation of the preamplifier circuitry by a large energy pulse. As the energy range increases for each CSP chip, the sensitivity will decrease and the noise will increase, as noted in Table 4.

Table 4: Cremat CSP properties [94].

Model	Gain (mV/pC)	Max detectable pulse (electrons)	Noise (ENC) in electrons RMS	C_f	R_f
CR-110	1400	10^7	200	1.4 pF	100 MΩ
CR-111	130	10^8	630	15 pF	10 MΩ
CR-112	13	10^9	6,800	75 pF	680 kΩ
CR-113	1.3	10^9	16,000	750 pF	68 kΩ

Therefore, it is necessary to carefully select the appropriate chip with the correct energy range and the maximum sensitivity. In order to determine the correct CSP, it is important to calculate the pulse magnitude. Using the equation:

$$Q_{pulse} = E_\alpha * \epsilon * G,$$

where E_α is the energy of the incident alpha particle, ϵ is the ionization efficiency, and G is the gain of the detector, we calculated this value for a silicon diode as well as an α-PbO detector. For the Si diode, $Q_{pulse} = 1.52 \times 10^6$ electrons, and for α-PbO, $Q_{pulse} = 9.14 \times 10^5$ electrons. This result would imply the CSP CR-110 should be used, although other aspects might change this determination. For example, high input capacitance may make CR-110 unstable, in which case CR-111 would be the preferred chip to use. The capacitance at the CSP input can also determine the rise time performance and that might imply that one of the faster CSPs should be used. Each of the CSP chips also has a maximum count rate that must be taken into consideration [94].

The CSP chips fit into a circuit board whose circuitry is presented in Figure 53. The bias supply in the setup used for this work is externally applied so that part of the circuit diagram is not used. The detector input is labeled ‘det’. The test pulse input is labeled ‘test input’. It is applied across a capacitor with a value of 1 pF. This is the capacitance that determines the amount of charge seen by the CSP due to the voltage setting of the test pulse generator.

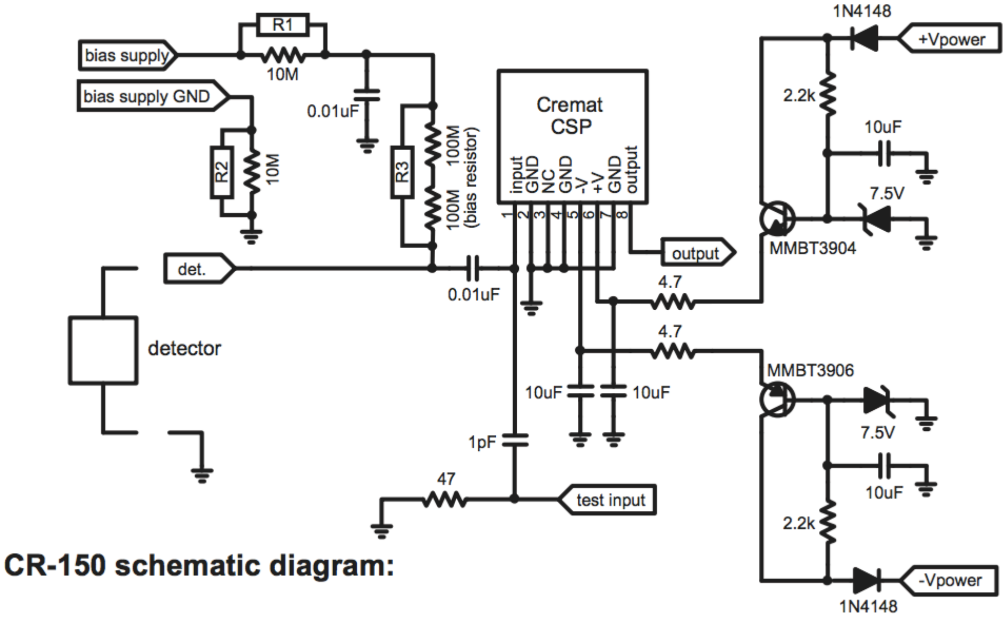

Figure 53: A schematic of the circuit board into which the CSP chips fit [93].

6.2.6 The Gaussian shaping amplifier

From the preamplifier, the signal is passed to a Gaussian shaping amplifier (GSA). The GSA in this research is a Canberra 2026 Spectroscopy Amplifier. This amplifier is one of the most important parts of the pulse processing procedure for energy spectroscopy. The GSA has a number of important functions. It magnifies the signal from the CSP from millivolts to 0.1-10 volts. This makes it much easier to accurately determine the pulse height for characterization in the multichannel analyzer. The GSA also converts the pulse shape received from the CSP into a Gaussian curve. This is important in order to enable accurate energy resolution and reduce the likelihood of overlapping pulses. Finally, it also provides a quickly restored baseline in order to be able to handle higher count rates. This requires registering the amplitude of the step from the pulse output of the CSP, but it removes the longer decay tail in order to be ready for the next incoming pulse.

The signal from the CSP can be simplified to a step function, although, the signal actually does decay over a long period of time. The actual shaping of the signal by the amplifier is achieved using a series of filters. The simplified concept behind this involves sending the signal through a CR high-pass filter and then through an RC low-pass filter. The initial CR high-pass filter is often called a CR differentiator. It attenuates low frequencies, thereby reducing noise and improving the signal-to-noise ratio. It also cuts short the pulse. The second RC low-pass filter, called the RC integrator, attenuates the high frequencies, which lengthens the rise time of the pulse. The result is a better signal-to-noise ratio because the noise has been eliminated from the high frequency regime.

Combining these two filters produces a pulse that rises more slowly to the maximum peak value and then decays back to the baseline more quickly than the original pulse. A schematic of this simplified circuit is displayed in Figure 54. It is common to have the time constants of both the differentiator and the integrator set to the same value:

$$\tau_D = C_D R_D, \quad \tau_I = R_I C_I, and\ \tau_D = \tau_I = \tau.$$

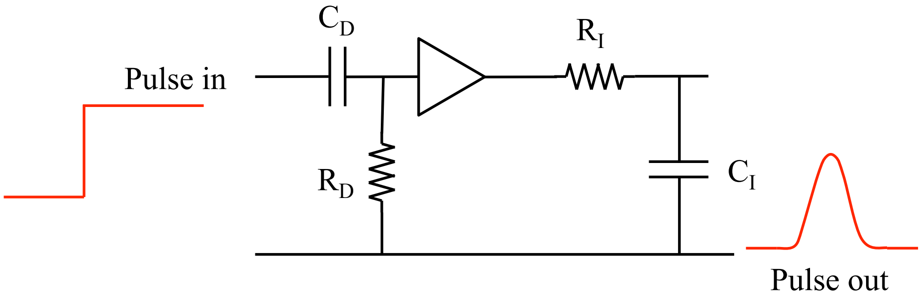

Figure 54: The CR-RC filter that explains the function of the Gaussian shaping amplifier. The CR differentiator is on the left side and is denoted by C_D and R_D. The RC integrator is on the right side and is denoted by R_I and C_I [95].

As the Gaussian curve tapers off, an overshoot generally occurs that causes the signal to dip below the baseline and then slowly rise back up to it. This is an artifact from the long decay of the pulse from the CSP. This becomes an issue if subsequent pulses arrive when the signal is lower than the baseline. This causes the ensuing signals to appear to have lower energies and it will broaden the energy peak, reducing the detector resolution. To mitigate this issue, the amplifier has a pole-zero cancellation circuit. It consists of a variable resistor in parallel with the capacitor in the differentiator, since that is the filter that handles the decay after the peak. This allows the operator to visually inspect the signal output for overshoot and to correct it if it appears. The CSP will have a set decay time constant. If the GSA shaping time constant is longer than the shaping time constant of the CSP, an undershooting of the decay to the baseline will occur. It is important to adjust this resistance in order to achieve the best spectrum resolution.

The time constant is a variable of the GSA that is adjusted during the setup. Choosing the proper time constant can help minimize noise and, therefore, improve the overall resolution of the system. The Canberra 2026 time constant can be set to 0.5 μs, 1 μs, 2 μs, 4 μs, 6 μs, or 12 μs. While the shorter time constants are in use, the field effect transistor in the first part of the CSP dominates the noise in the system. As the time constant reaches higher values, the noise is dominated by the detector leakage current, the FET gate leakage current, and the thermal noise in the feedback resistor, R_f, in the CSP. The value of the time constant that enables the least amount of noise depends upon the detector, the CSP, and the properties of the amplifier [95].

6.2.7 The multichannel analyzer

Once the detector signal pulses pass through the preamplifier and the amplifier, they are ready to be counted and displayed in an energy spectrum. This is the function of the multichannel analyzer (MCA). The MCA creates a histogram of the peak height values obtained from the GSA. It receives the peak heights in terms of a voltage that lies somewhere between 0 volts and 10 volts. It breaks this voltage range into a number of channels. As the pulse arrives, the MCA measures the amplitude of the pulse and places it into the channel with the correct voltage range. It does this with each pulse that arrives and it adds a count to the correct channel. Over time, the energy spectrum for the emitting source is revealed.

When a pulse arrives, the MCA analyzes it to determine the maximum peak height. Once it determines this, it stops acquiring new pulses while it adds one count to the channel in which the last pulse belongs. During this time, which is known as dead time, the system is not acquiring new pulses. Once the filing process is complete, the acquisition is restarted. The MCA employs a lower level discriminator set at a level just above the highest value of the noise so that it does not use up processing time on noise. This significantly reduces the amount of dead time during the data acquisition.

The number of channels that span the total voltage range determines the resolution of the MCA. Depending upon the MCA, the resolution can generally be set from 500 channels to up to 32,000 channels. The coarser resolution range will show peaks more quickly; however, to see finer resolution for higher quality detectors, a higher resolution, and therefore a longer integrating time, is necessary.

The MCA interfaces with a computer through a USB port and displays the spectrum in real time as the acquisition progresses. The channels can be calibrated to the corresponding energy units to enable further analysis of the energy spectrum. The MCA enables selection of peaks in the energy spectrum, which are known as regions of interest (ROI). These can be analyzed for total counts and FWHM [96].

6.2.8 The entire picture

The alpha detection system fits together as a complete system, as shown schematically in Figure 55. The initial input comes either from the test pulse generator or from an alpha particle absorbed by the detector. In both cases, the pulse appears as a sharp rise and a longer decay tail, with a charge whose magnitude corresponds to either the energy of the alpha particle or the voltage setting on the test pulse generator. The charge pulse travels to the charge sensitive preamplifier, where is it converted into a voltage step with a very slow decay time in such a way that it appears to be a step function. This pulse is then passed to the Gaussian shaping amplifier, where the high and low frequencies are removed so that the pulse ends up as a Gaussian curve. Up until this point, the pulse height is maintained throughout the process. The GSA can amplify the pulse height by a variable amount during the shaping process. This pulse height is measured by the multichannel analyzer and placed in the proper energy channel in the energy spectrum. In this way, spectroscopic analysis is performed for an incident alpha particle or a test pulse. The entire system is set up with a universal ground and is powered through an isolation transformer. The isolation transformer supplies AC power while suppressing the electronic noise caused by ground loops in the building power system [97].

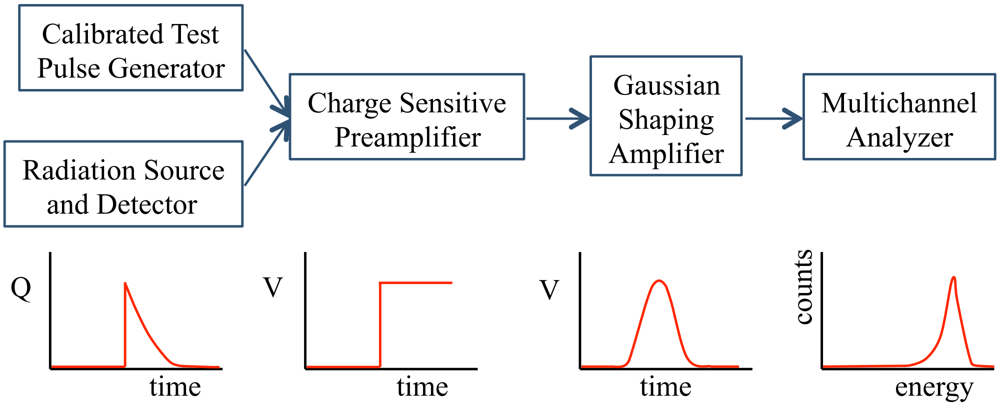

Figure 55: The detection system from the incident test pulse or the alpha particle to the MCA. Below each step are schematics of what the signal looks like during that phase of the processing.

6.3 Data and Analysis

6.3.1 Calibration of the energy spectrum

The setup described in Section 6.2 enables calibration of the energy spectrum via the following method. The test pulse is set up so that it appears in the spectrum at the location of the desired test energy. The oscilloscope probe measures the voltage of the test pulse. Because the preamplifier is sensitive to charge, the next step is to calculate the charge the test pulse voltage introduces into the preamplifier. The injection occurs at a capacitor with a value of 1 pF. Therefore, for a test pulse voltage of 0.2 V:

$$Q = CV = 1\,pF * 0.2\,V = 2\times10^{-13}\,Coulombs.$$

Each electron-hole pair has 1.6x10^{-19} C/e-h pair. Therefore, calculation of the number of electron-hole pairs created by the test pulse yields:

$$\frac{2\times10^{-13}C}{1.6\times10^{-19}\ C/eh\,pair} = 1{,}250{,}000\ electron\ hole\ pairs.$$

The conversion to peak height requires knowledge of the pair creation energy or the ionization energy for the specific detector. For a silicon diode, this value is ~ 4 eV/eh pair. This gives the energy for the peak displayed by the multi-channel analyzer, as follows:

$$1{,}250{,}000\ eh\,pairs * 4\,\frac{eV}{eh\,pair} = 5\,MeV$$

This means that the location of the test pulse on the spectrum displayed by the multi-channel analyzer has energy equal to 5 MeV. The energy spectrum displayed by the MCA during detection with α-PbO will shift due to the difference in electron-hole pair creation energy between the Si diodes and the lead oxide detectors. Following a similar calculation, the same test pulse voltage would result in a reference energy peak of 8.75 MeV.

6.3.2 Preamplifier range testing

The process described in Section 6.3.1 is useful for confirming the energy range of the CSP chips. Installing the desired CSP chip and measuring the incremental values of the test pulse enables the calibration of the energy range of the CSP with respect to the voltage supplied by the test pulse generator, as presented in Figure 56.

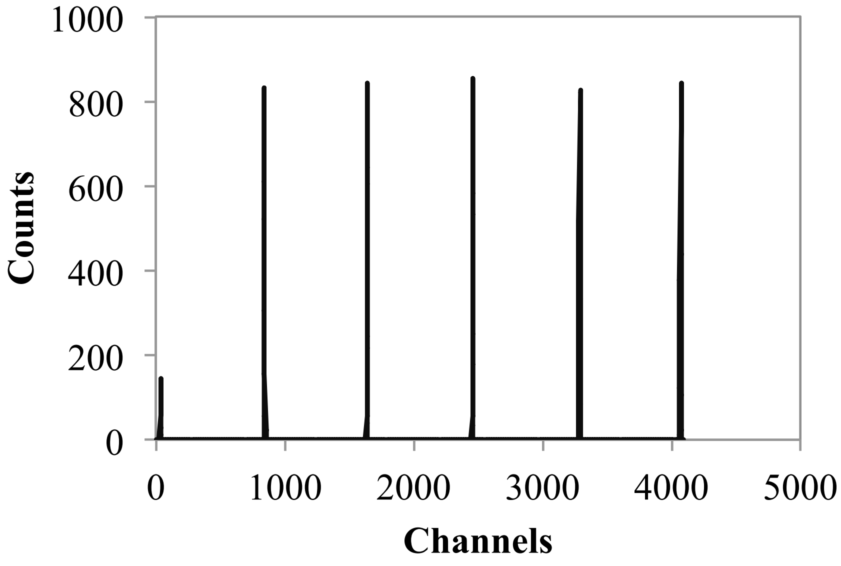

Figure 56: An energy spectrum showing incremental stepping of the test pulse generator in order to characterize the detection system output. Each peak corresponds to a larger energy, or channel number, than the previous by a value of 0.5 volts at the test pulse generator.

The spectrum in Figure 56 shows a pulse at channel zero that corresponds to the noise peak, as well as a voltage of zero for the test pulse. This noise peak is kept at a low level to ensure that the signal processing that it causes does not introduce excessive dead time into the system. The system setup includes a silicon diode fabricated at Lawrence Berkeley National Lab and the CR-111 CSP chip. Test pulse voltage is applied at 0.5 V intervals, with the 10x attenuator. The five peaks have voltage values at the test pulse generator of 0.05 v, 0.1 volts, 0.15 volts, 0.2 volts, and 0.25 volts. Following the calibration scheme outlined in Section 6.3.1 yields peak energies of 1.25 MeV, 2.5 MeV, 3.75 MeV, 5.0 MeV, and 6.25 MeV, respectively.

6.3.3 Si-diode testing

Before testing the α-PbO detectors on an untested system, a silicon diode was used to ensure that the system was functioning as expected. The silicon diode was manufactured at Lawrence Berkeley National Lab. The diode is fabricated using high-resistivity n-type silicon. The p-type contact is made via a boron implant. The p-type contact side of the detector has a patterned pixel and a guard ring. The other surface, through which the alpha particles will enter, has a thin n-type contact made of phosphorus-doped polysilicon. The total diode thickness is ~ 300 μm. The diode has a leakage current of 23 pA at 100 V reverse bias and it is fully depleted at 30 V, as seen in the plots in Figure 57.

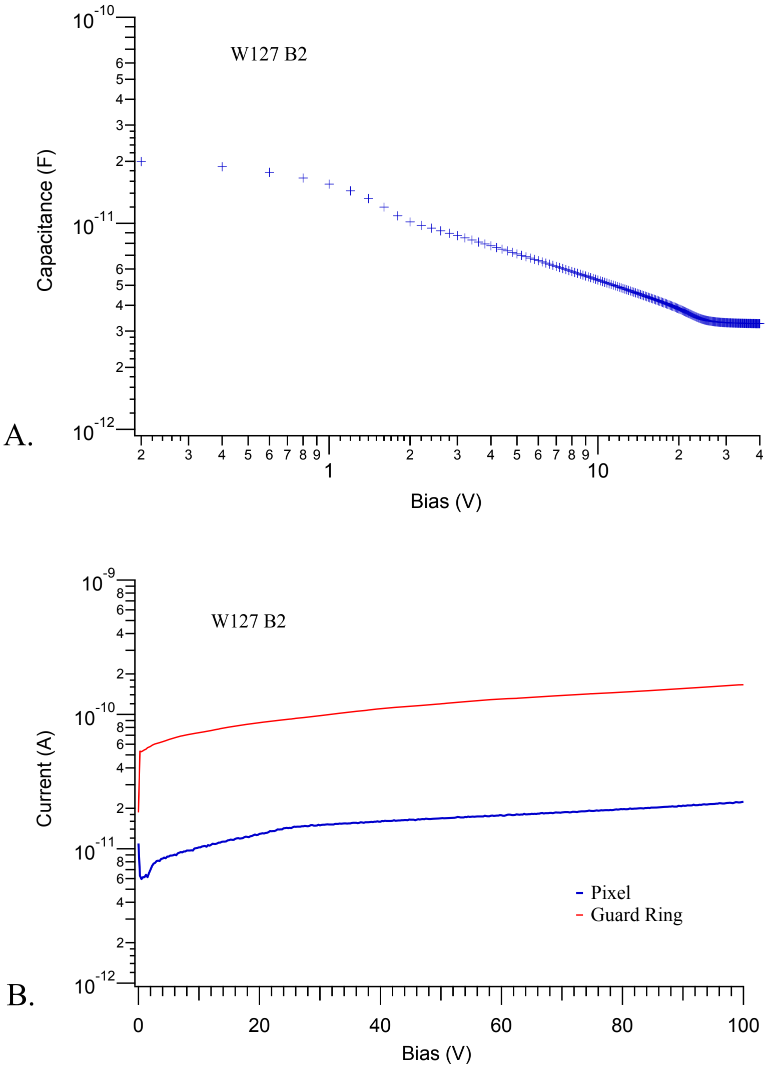

Figure 57: A.) CV curve for the silicon test diode. Capacitance bottoms out between 25 V and 30 V; therefore, the diode must be fully depleted at those voltages. B.) IV curves for the silicon test diode. Leakage current for the pixel is in the 23 pA range at 100 V. Diode and data courtesy of Craig S. Tindall at Lawrence Berkeley National Laboratory.

The first test of the silicon diode involved varying the bias voltage to observe the detector response at various levels. The alpha source for this test is ^{241}Am. The time constant used throughout this experiment was 6 μs. The test pulse was calibrated to 7.5 MeV and the live capture time is 900 s. As noted in Figure 58, the use of 9 V or 18 V is not sufficient enough to bias the diode. The diode must have at least 27 volts to measure the proper energy of the alpha particles. This finding aligns very well with the prior CV measurements, indicating full depletion in that range of bias voltage.

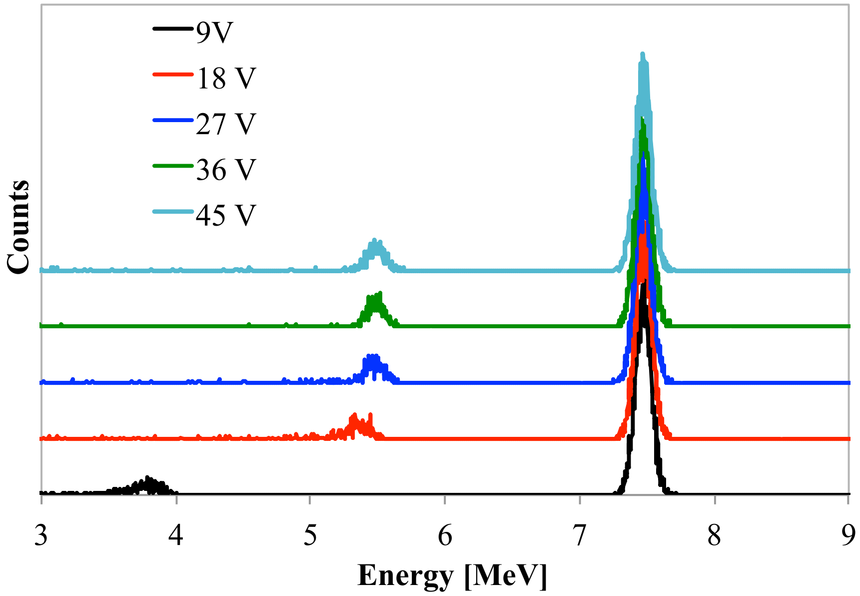

Figure 58: Energy spectrum of alpha particles detected by a silicon diode at varying bias voltages. The pulse on the right side is the test pulse, the pulses to the left are the alpha energy peaks.

A similar test was performed to observe the effect of various time constants on the spectrum. The silicon diode was biased with 45 volts. The source, test pulse energy calibration, and live capture time are the same as those used in the previous test. As noted in Figure 59, varying the time constant moves the energy range to new channels in the multichannel analyzer. For this reason, any measurements taken at different time constants will need to be re-calibrated. The effect of the time constant on the noise of the measurement can be seen in the test pulse at each value. The test pulse for a time constant of 1 μs has a FWHM of ~ 22 channels, the FWHM of the 2 μs peak is ~ 30 channels, the FWHM of the 4 μs peak is ~ 44 channels, and the FWHM of the 6 μs peak is ~ 49 channels. Thus, it is quite obvious that, for the silicon diode detector, the smallest time constants provide the least amount of noise to the measurement.

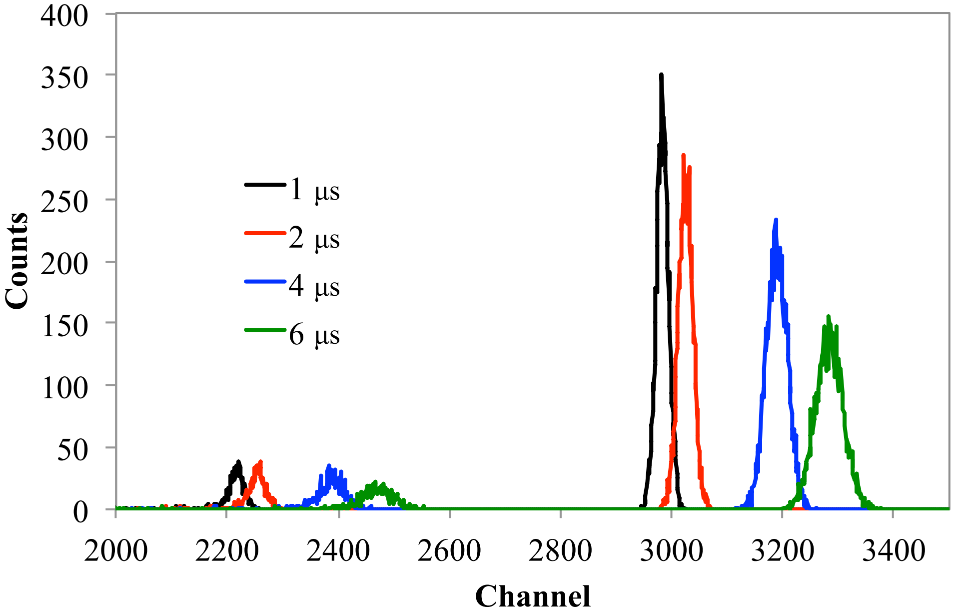

Figure 59: Energy spectrum of alpha particles detected by a silicon diode at various time constants. Both the test pulses and the alpha energy peaks change position with the time constant.

6.3.4 Alpha particles on α-PbO

Initial testing on α-PbO was performed on films that were not thick enough to stop a significant number of alpha particles. For films of ~ 2 μm, no signal was seen. This means that the charge carrier generation from the tail of the alpha particle, before it left the sample, was insufficient to overcome the system noise with its signal.

Thicker films (~ 8 μm) were grown via PLD. Testing in the alpha detection system with these films yielded evidence of charge carrier creation due to the alpha particles. Figure 60 displays data showing evidence of alpha particle interaction with the α-PbO detector. The blue line is the background signal when the shutter is closed and no alpha particles are reaching the detector. The red line is data taken when the shutter is open and the alpha particles are incident onto the detector. The peak on the right side is the test pulse peak. The tallest peak on the left side is the noise in the system. At the foot of the noise peak, the signal from the alpha particles can be seen when the shutter is open. This signal disappears when the shutter is closed, and it is repeatable. However, the test pulse peak is centered at ~ 1 MeV. This alpha shoulder is at a very low energy for alpha particles that are incident at 5.4 MeV. An explanation for this is evident after examining the stopping range information in Figure 50. It is likely that the alpha particles are not fully stopped within the detector layer and they leave only a small fraction of their energy in the film as electron-hole pairs. In order to move the alpha energy peak out of the noise, the detector layer will have to be thicker if it is to stop the full energy of the alpha particle within the detector layer.

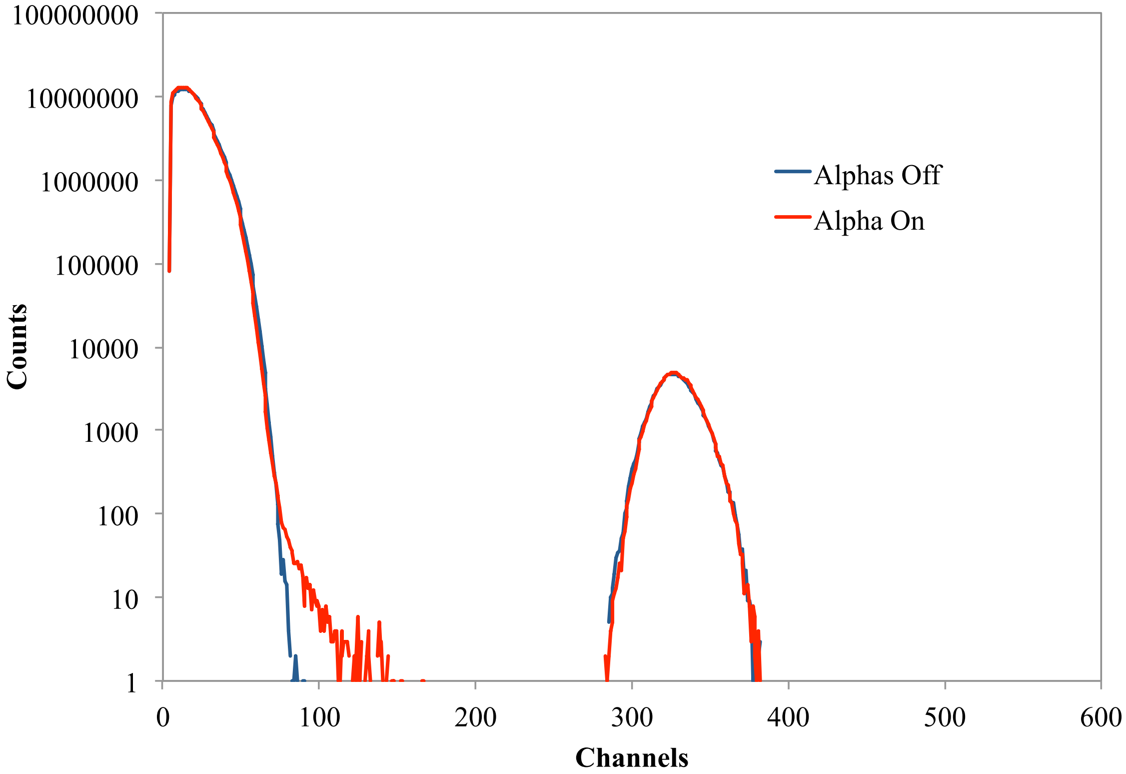

Figure 60: Evidence of alpha particle interaction with an α-PbO detector. Due to insufficient thickness, the tail energy of the alpha particle is all that is collected, yielding a low shoulder just above the noise level.

6.4 Summary

Due to their large energy and relatively small penetration depth, alpha particles were chosen in an initial attempt at radiation detection in α-PbO thin-film detectors. The radiating source is ^{241}Am with an activity of 100 nCi. Theoretical calculation of the Bragg peak of the alpha particles in α-PbO estimates a very sharp peak, with the vast majority of alpha particles stopping at a depth of ~ 16 μm. The experimental setup consists of a sample in a vacuum chamber. A high voltage bias filter introduces the bias to the detector. The detector output enters a charge sensitive preamplifier, along with a test pulse. The CSP collects the charge from the alpha absorption and converts it into a voltage, which is passed to a Gaussian shaping amplifier. The GSA takes the voltage step and converts it into a Gaussian peak with a defined and amplified peak height. This peak is passed to its multichannel analyzer, which files it into the correct channel corresponding to the peak height. The test pulse is used to calibrate the energy of the channels and determine the energy spectrum of the resulting peaks. Initial control testing of the alpha particle system was performed using a Si-diode. Energy range calibration was confirmed and the effect of voltage bias and time constant were analyzed. Evidence of alpha particles was seen above the noise level of the system; however, thicker samples are necessary to achieve a true alpha particle spectrum with α-PbO.

Chapter 7: Conclusion

7.1 Summary:

The global nature of the shipping industry and high throughput of cargo containers through ports increases the opportunity of nuclear terrorism delivered by means of containers. This drives the search for new and better high-resolution, room-temperature, semiconductor radiation detector materials. In this work we focused on growth and characterization of α-PbO. Absorption spectroscopy and ellipsometry measurements enabled characterization of the optical properties and constants of α-PbO. These measurements yielded band gap energies of $E_g = 3.2$ eV (direct) and $E_g = 1.9$ eV (indirect), as well as the complex spectral index of refraction. Spectral photocurrent and photocurrent-voltage measurements were used to characterize the electronic and transport properties of α-PbO. Spectral photoconductivity confirmed the band gaps measured by optical absorption and yielded a photocurrent with a magnitude 10^4 times that of the dark current. Fitting of Many's equation to the photocurrent-voltage data produced a value of $\mu\tau = 6.8 \times 10^{-4}$ cm^2/V for the majority carrier. Finally, α-PbO displayed detection of radiation particles through measurement of its response to alpha particles.

7.2 Limitations and Implications

The film format of the material is the most important limitation of this work. Thin films do not have the requisite stopping power to fully absorb high-energy γ-rays. Additionally, there are measurement effects from the thin film nature of this material that may not be evident in a bulk single crystal. Finally, four-point probe resistivity measurements are necessary to determine the material resistivity without effects of contact resistance on the measurements. These measurements are currently underway.

Notwithstanding these limitations, this work has demonstrated that α-PbO is highly interesting as a potential room temperature detector material. α-PbO has a high atomic number and a high density. It has a band gap in the range required for room temperature detection. It has a significant photoconductive response to illumination by light with energy above the band gap. The μτ-product derived from the photocurrent-voltage characteristic was a few orders of magnitude lower than most of the leading room temperature detector materials. However, most detector materials require improvement in that area before they can become operational, high-resolution detectors. Indeed, research on detector materials based on CdTe has been underway since the 1970s. However CdTe did not gain interest as a promising detector material until the late 1980s. Therefore, we do not expect α-PbO detectors to rival the quality of CZT detectors in the near future. The implication of this study's conclusions is that α-PbO is a highly interesting material for room temperature radiation detection. Further research on α-PbO should be pursued with single crystals.

7.3 Contributions of this Work

This work has contributed a number of achievements to the study of α-PbO as a room temperature semiconductor radiation detector. The first of these achievements includes the development and optimization of a growth process for epitaxial films of α-PbO using pulsed laser deposition. Extensive structural characterization and optimization of the growth parameters yielded growth of epitaxial thin films of high quality, single-phase, highly oriented α-PbO. Routine optical absorption measurement confirmed that the indirect band gap and the direct band gap of this material are in the expected ranges. For the first time, spectral ellipsometry measurements were performed in order to calculate the spectral complex index of refraction on α-PbO. The spectral photoconductivity measurements yielded photocurrents that were four orders of magnitude greater than the dark current, thereby proving significant photoconductivity in α-PbO. We also performed the first fitting of Many's equation to photocurrent-voltage characteristics, calculating a μτ-product for α-PbO. Finally, α-PbO has been proven to detect radiation decay products in the form of alpha particles.

References

1. Allison, G., *Nuclear Terrorism: The Ultimate Preventable Catastrophe*. 2004, New York: Times Books, Henry Holt and Company, LLC.
2. Kouzes, R.T., et al. *Naturally occurring radioactive materials and medical isotopes at border crossings*. in *Nuclear Science Symposium Conference Record, 2003 IEEE*. Portland, OR.
3. Righi, S. and L. Bruzzi, *Natural radioactivity and radon exhalation in building materials used in Italian dwellings.* Journal of Environmental Radioactivity. **88**(2): p. 158-170.
4. Xinwei, L., *Radioactivity level in Chinese building ceramic tile.* Radiation Protection Dosimetry, 2004. **112**(2): p. 323-327.
5. Alberto Malanca, R.S., Harim Revorêdo de Macêdo, *Radium, potassium, and caesium in foodstuffs from a Brazilian state.* Journal of Environmental Science and Health, Part A. **34**(2).
6. Zagatto, V.A.B., et al., *Natural Radioactivity in Bananas.* AIP Conference Proceedings, 2008. **1034**(1): p. 264-268.
7. Peplow, D.E., *Fiestaware™ radiography.* The Physics Teacher, 1999. **37**(5): p. 316-318.
8. Luke, P.N. and M. Amman, *Room-temperature replacement for ge detectors - Are we there yet?* IEEE Transactions on Nuclear Science, 2007. **54**(4): p. 834-842.
9. Sandeep K. Chaudhuri, R.M.K., Kelvin J. Zavalla, Liviu Matei, Vladimir Buliga, Michael Groza, Arnold Burger, and Krishna C. Mandal, *Cd0.9Zn0.1Te Crystal growth and fabrication of large volume single-polarity charge sensing gamma detectors.* IEEE Transactions on Nuclear Science, 2013. **60**(4): p. 2853-2858.
10. Owens, A. and A. Peacock, *Compound semiconductor radiation detectors.* Nuclear Instruments & Methods in Physics Research Section a-Accelerators Spectrometers Detectors and Associated Equipment, 2004. **531**(1-2): p. 18-37.
11. Schottmiller, J.C., *Photoconductivity in Tetragonal and Orthorhombic Lead Monoxide Layers.* Journal of Applied Physics, 1966. **37**(9): p. 3505-3510.
12. Knoll, G.F., *Radiation detection and measurement*. 4th ed. 2010, New York, USA: John Wiley & Sons, Inc.
13. Aberlizov, *Components of the detector response for the energy of incidnet photons*, D.R.C. Spectrum.jpg, Editor. 2008, nucleonica.com.
14. AllenMcC., Am-Be-SourceSpectrum.jpg, Editor. 29 October 2007. p. http://en.wikipedia.org/wiki/File:Am-Be-SourceSpectrum.jpg.
15. Hykes, J., in *matplotlib*, Al-gamma-xs.svg, Editor. 2011. p. http://en.wikipedia.org/wiki/File:Al-gamma-xs.svg.
16. Hykes, J., in *matplotlib*, Pb-gamma-xs.svg, Editor. 2011. p. http://en.wikipedia.org/wiki/File:Pb-gamma-xs.svg.
17. Lindsey, C.S. *Photon Absorption*. March 2014]; Available from: http://www.particle.kth.se/~fmi/kurs/PhysicsSimulation/Lectures/04B/photonAbsorp.html.
18. Lappe, F., *The energy of electron-hole pair formation by x-rays in PbO.* Journal of Physics and Chemistry of Solids, 1961. **20**(3/4): p. 173-176.
19. Kasap, S. and P. Capper, eds. *Springer Handbook of Electroic and Photonic Materials*. Springer Handbooks. 2007, Springer: Leipzig.

20. Klein, C.A., *Bandgap Dependence and Related Features of Radiation Ionization Energies in Semiconductors.* Journal of Applied Physics, 1967. **39**(4): p. 2029-2038.
21. Ortec, *Why High-Purity Germanium (HPGe) radiation detection technology is superiour to other detector technologies for isotope identification*.
22. Pehl, R.H. and F.S. Goulding, *Recent observations on the Fano factor in germanium.* Nuclear instruments and methods, 1970. **81**: p. 329-330.
23. Haller, E.E., *Detector materials: germanium and silicon.* IEEE Transactions on Nuclear Science, 1982. **NS-29**(3): p. 1109-1118.
24. Niemela, A. and H. Sipila, *Evaluation of CdZnTe detectors for soft X-Ray applications.* IEEE Transactions on Nuclear Science, Aug 1994. **41**(4): p. 1054-1057.
25. Sordo, S.D., et al., *Progress in the Development of CdTe and CdZnTe semiconductor radiation detectors for astrophysical and medical applications.* Sensors, 2009. **9**: p. 3491-3526.
26. Owens, A., *Semiconductor materials and radiation detection.* Journal of Synchrotron Radiation, 2006. **13**(2): p. 143-150.
27. Amman, M., et al., *Evaluation of THM-Grown CdZnTe Material for Large-Volume Gamma-Ray Detector Applications.* IEEE Transactions on Nuclear Science, June 2009. **56**(3): p. 795-799.
28. Dalven, R., *A review of the semiconductor properties of PbTe, PbSe, PbS and PbO.* Infrared Physics, 1969. **9**: p. 141-184.
29. Hitomi, K., et al., *TlBr Capacitive Frisch Grid Detectors.* IEEE Transactions on Nuclear Science, 2013. **60**(2): p. 1156-1161.
30. Wriedt, H.A., *The O−Pb (Oxygen-Lead) system.* Journal of Phase Equilibria, 1988. **9**(2): p. 106-127.
31. Cancarevic, M., M.V. Zinkevich, and F. Aldinger, *Pb-O Phase Diagram*, P.V. ASM Alloy Phase Diagrams Center, editor-in-chief; H. Okamoto and K. Cenzual, section editors, Editor., http://ww1.asminternational.org/AsmEnterprise/APD , ASM Iternational: Materials Park, OH, 2005.
32. Heijne, L., P. Schagen, and H. Bruining, *Television Pick-up Tube for both Light and X-ray pictures.* Nature, 1954. **173**: p. 220.
33. Doorn, A.G.v., *The "Plumbicon" compared with other television camera tubes.* Philips Technical Review, 1966. **27**(1): p. 1-14.
34. Kwestroo, W., J.H.v.d. Biggelaar, and C. Langereis, *The Formation of PbO-SnO solid solutions.* Philips Research Laboratories, 1970. **5**(5): p. 307-314.
35. Biberman, L.M. and S. Nudelman, eds. *Photoelectronic Imaging Devices*. Optical Physics and Engineering, ed. W.L. Wolge. Vol. 2. 1971, Springer Science + Business Media: New York.
36. Neuhauser, R.G., *Photoconductors Utilized in TV Camera Tubes.* Journal of the Electrochemical Society, 1987. **134**(1): p. 5C-13C.
37. Bali, S.P., *Consumer Electronics*. 2008, India: Dorling Kindersley.
38. Chao, S., et al., *Multiple phase change of lead oxide film for optical storage.* Journal of Physics D: Applied Physics, 1990. **23**: p. 955-958.
39. Zabinski, J.S., et al., *Synthesis and characterization of PbO films grown by pulsed laser deposition.* Materials Research Society Proceedings, 1992. **235**: p. 849-854.
40. Baleva, M. and V. Tuncheva, *Laser-assisted deposition of PbO films.* Journal of Materials Science Letters, 1994. **13**: p. 3-5.

41. Veluchamy, P. and H. Minoura, *Simple electrochemical method for the preparation of a highly oriented and highly photoactive α-PbO film.* Applied Physics Letters, 1994. **65**(19): p. 2431-2433.
42. Cattley, C.A., et al., *Colloidal synthesis of lead oxide nanocrystals for photovoltaics.* Chemical Communications, 2010. **46**: p. 2802-2804.
43. Droessler, L.M., H.E. Assender, and A.A.R. Watt, *Thermally deposited lead oxides for thin film photovoltaics.* Materials Letters, 2012. **71**: p. 51-53.
44. Wiechert, D.U., S.P. Grabowski, and M. Simon, *Raman spectroscopic investigation of evaporated PbO layers.* Thin Solid Films, 2005. **484**: p. 73-82.
45. Hwang, O., et al., *Effect of thermal annealing of lead oxide film.* Nuclear Instruments & Methods in Physics Research A, 2010. **633, Supplement 1**: p. S69-S71.
46. Berashevich, J. and A. Reznik, *Non-magnetic impurities to induce magnetism in α-PbO crystal structure.* Europhysics Letters, 2013. **104**(3): p. 37008.
47. Keezer, R.C., D.L. Bowman, and J.H. Becker, *Electrical and Optical Properties of Lead Oxide Single Crystals.* Journal of Applied Physics, 1967. **39**(4): p. 2062-2066.
48. Rooymans, C.J.M. and W.F.T. Langenhoff, *Hydrothermal growth of single crystals and phase width of tetragonal lead monoxide.* Journal of Crystal Growth, 1968. **3**(4): p. 411-416.
49. Rastrenenko, N.A., et al., *Ellipsometry of tetragonal lead oxide single crystals.* Solid State Communications. **38**(5): p. 393-395.
50. Oka, K., H. Unoki, and T. Sakudo, *Growth of single crystals of lead monoxide.* Journal of Crystal Growth, 1979. **47**: p. 568-572.
51. Heijne, L., *Contact influence on the photoconductivity of lead oxide.* Journal of Physics and Chemistry of Solids, 1961. **22**: p. 207-212.
52. Clarke, J.R. and J.E. Greene, *Reactively evaporated photoconductive PbO: Phase transformations induced by water vapor.* Thin Solid Films, 1980. **66**: p. 339-349.
53. Light, T.B., et al., *Structure of thin lead oxide layers as determined by x−ray diffraction.* Journal of Applied Physics, 1975. **46**(4): p. 1489-1492.
54. Harris, E.P., P.S. Hauge, and C.J. Kircher, *Optical properties of ultrathin PbO layers grown on Pb films.* Applied Physics Letters, 1979. **34**(10): p. 680-682.
55. Thangaraju, B. and P. Kaliannan, *Optical and structural studies on spray deposited α-PbO thin films.* Semiconductor Science and Technology, 2000. **15**: p. 542-545.
56. Eason, R., ed. *Pulsed Laser Deposition of Thin Films: Applications-led growth of functional materials*. 2007, John Wiley and Sons, Inc.: Hoboken, New Jersey.
57. Chrisey, D. and G. Hubler, *Pulsed Laser Deposition of Thin Films*. 1994, New York: Wiley.
58. Baleva, M. and V. Tuncheva, *Structural and optical investigation of PbO films grown by pulsed laser deposition.* Journal of Materials Science Letters, 1994. **13**: p. 65-67.
59. Boudias, C.M., Daniel, *CaRIne Crystallography*. 2005.
60. Guinebretière, R., *X-ray Diffraction by Polycrystalline Materials*. 2007, Newport Beach, Ca: iSTE Ltd. 347.
61. Smilgies, D.M., *Scherrer grain-size analysis adapted to grazing-incidence scattering with area detectors (vol 42, pg 1030, 2009).* Journal of Applied Crystallography, 2013. **46**(1): p. 286-286.

62. Cullity, B.D., *Elements of X-ray Diffraction*. 2nd ed. Addison-Wesley Series in Metallurgy and Materials, ed. M. Cohen. 1978, USA, Canada: Addison-Wesley Publishing Company, Inc.
63. Freund, L.B. and S. Suresh, *Thin Film Materials*. 2003, New York: Cambridge University Press.
64. Heavens, O.S., *Optical Properties of Thin Solid Films*. 1991, London, England: Butterworths Scientific Publications.
65. Pankove, J.I., *Optical Processes in Semiconductors*. 1971, Englewood Cliffs, New Jersey: Prentice-Hall, Inc.
66. Izvozchikov, V.A., *Crystallochemical Peculiarities and Shape of the Absorption Edge of Lead Oxides.* Physica Status Solidi (a), 1972. **14**: p. 161-170.
67. PerkinElmer, *Why Limit Yourself, High Performance UV/VIS/NIR Instruments*, I. PerkinElmer, Editor. 2012: Waltham, Ma.
68. PerkinElmer, *Design Considerations for a Variable Angle Absolute Reflectance Accessory*, P.L.a.A. Sciences, Editor. 2004: Shelton, CT.
69. Schroder, D.K., *Semiconductor Material and Device Characterization*. 3rd ed. 2006, Hoboken, New Jersey: John Wiley & Sons, Inc. .
70. Yu, P.Y. and M. Cardona, *Fundamentals of Semiconductors - Physics and Materials Properties*. 3rd ed. 2003, Verlag Berlin Heidelberg New York: Springer.
71. Aspnes, D.E., *Spectroscopic Ellipsometry of Solids*, in *Optical Properties of Solids - New Developments*, B.O. Seraphin, Editor. 1976, American Elsevier Publishing Company, Inc.: New York.
72. Yacobi, B.G., *Semiconductor Materials: An Introduction to Basic Principles*. 2004, New York: Kluwer Academic Publishers.
73. Dresselhaus, M.S. *Solid State Physics*. 2001 [cited 2014 March 2014]; Available from: http://web.mit.edu/course/6/6.732/www/texts.html.
74. Hector, L.G. and H.L. Schultz, *The Dielectric Constant of Air at Radiofrequencies.* Journal of Applied Physics, 1936. **7**(4): p. 133-136.
75. Eldridge, J.M. and D.W. Dong, *The growth of thin PbO layers on lead films.* Surface Science, 1973. **40**: p. 512-530.
76. Chou, N.J., et al., *Auger and ellipsometric studies of ultra-thin PbO growth on Lead.* Journal of Electronic Materials, 1973. **2**(1): p. 115-126.
77. Mulder, B.J. and J.d. Jonge, *Quantum efficiency of photoconduction in Lead Oxide.* Solid State Communications, 1966. **4**(6): p. 293-294.
78. Broek, J.v.d., *Physical interpretation of a PbO-photoconductor.* Solid State Communications, 1966. **4**(6): p. 295-296.
79. Cui, Y., et al., *DC Photoconductivity Study of Semi-insulating CdZnTe Crystals.* Electronic Materials, 2001. **30**(6): p. 774-778.
80. Zanichelli, M., et al., *Charge collection in semi-insulator radiation detectors in the presence of a linear decreasing electric field.* Journal of Physics D: Applied Physics, 2013. **46**: p. 9pp.
81. Sellin, P.J., et al., *Drift Mobility and Mobility-Lifetime Products in CdTe:Cl Grown by the Travelling Heater Method.* IEEE Transactions on Nuclear Science, 2005. **52**(6): p. 3074-3078.

82. Zanichelli, M., et al., *Characterization of bulk and surface transport mechanisms by means of the photocurrent technique.* IEEE Transactions on Nuclear Science, 2009. **56**(6): p. 3591-3596.
83. Many, A., *High-field effects in photoconducting cadmium sulphide.* Journal of Physics and Chemistry of Solids, 1864. **26**: p. 575-585.
84. *Operation and service manual - Model 4140B pA meter/DC voltage source*. 1980, Tokyo, Japan: Yokogawa-Hewlett-Packard, LTD.
85. Alden, E., *Muon Cooling*. 2002, Columbia University: Nevis Labs.
86. Magill, J. and J. Galy, *Radioactivity Radionuclides Radiation*. 2005, Berlin Heidelberg: Springer.
87. Bé, M.-M., et al., *Table of Radionuclides*. Monographie BIPM. Vol. 2-A. 2004, France: Bureau International Des Poids et Mesures.
88. Braibant, S., G. Giacomelli, and M. Spurio, *Particles and Fundamental Interactions*. Undergraduate Lecture Notes in Physics. 2009, Italy: Springer.
89. Loveland, W., D.J. Morrissey, and G.T. Seaborg, *Modern Nuclear Chemistry*. 2006, Hoboken, New Jersey: John Wiley & Sons, Inc.
90. Ziegler, J.F., J.P. Biersack, and M.D. Ziegler, *SRIM - The Stopping and Range of Ions in Matter [computer program]*. . http://www.srim.org.
91. *General Purpose Tail Pulse Generator*, in http://www.berkeleynucleonics.com/resources/BH-1_Datasheet.pdf, B.N. Corp., Editor.: San Rafael.
92. Ortec, *Preamplifier Introduction*, Ametek, Editor. 2009: Oak Ridge, TN.
93. Cremat, I. *Charge Sensitive Preamplifiers*. 2014; Available from: http://www.cremat.com/CSP_intro.htm.
94. Cremat, I. *CSP selection guide*. 2014; Available from: http://www.cremat.com/preamplifier_choice.htm.
95. Cremat, I., *Introduction to Amplifiers*, Amtek, Editor. 2009: Oak Ridge, TN.
96. Ortec, I., *The Multichannel Pulse-Height Analyzer*, Amtek, Editor. 2010: Oak Ridge, TN.
97. *Electrical isolation*. 2012 April 5, 2014]; Available from: http://www.allaboutcircuits.com/vol_2/chpt_9/3.html.